ABSTRACT

HONG, YAOYE. Mechanics-guided Morphological Intelligence in Kirigami Structures. (Under the direction of Dr. Jie Yin).

Living organisms possess an inherent ability to adapt their shapes in order to excel in various tasks within unstructured environments. Recent advancements in the field have employed shape-morphing materials, such as stimuli-responsive materials or pneumatic/hydraulic actuators, to achieve diverse functionalities in water and energy harvesting, soft electronics, biomedical devices, biology conservation, and soft robotics. However, developing a systematic approach to program morphologies for functional evolutions remains a formidable challenge. Addressing this gap, this thesis introduces a novel framework based on mechanics-guided morphologies of kirigami structures. By leveraging this approach, the morphological properties are effectively translated into practical applications for evolutionary advancements in soft robotics.

First, this thesis exploits programming the boundary curvatures of cuts rather than the complex cut patterns in kirigami sheets for target 3D curved morphologies in both forward and inverse designs, motivated by the Gauss-Bonnet theorem in differential geometry. This strategy largely simplifies the inverse design using the geodesic feature of the discrete ribbons. Leveraging this, I demonstrate its potential applications as dynamically conformable heaters for human knees. This strategy opens a new avenue to encode boundary curvatures for shape-programing materials with potential applications in soft machines and wearable devices.

Next, by systematically adjusting the geometric parameters of coupled ribbons, this thesis demonstrates the generation of nastic wavy shapes in artificial kirigami structures. The developed analytical framework enables accurate prediction and precise control over the resulting morphologies exhibited by these interconnected ribbons. Through the utilization of mechanical shape evolutions, this method offers mechanical means to induce curved and undulating shapes,

circumventing the need for material or chemical interventions. As a result, the proposed approach holds considerable potential for a wide array of applications in the fields of biology and soft robotics.

Then, the thesis shows the morphology-induced application as a noninvasive kirigami-based gripper for gelatinous organisms. Further, this thesis reports the evolution of kirigami-based manipulations into an ultragentle, ultrastrong, and precise gripper enabled by tendril-like grasping trajectories. Such multi-capability stems from programmable trajectories rationalized through experiments, simulations, and analytics. Driving the trajectory towards nastic tendril curves yields preternatural capabilities for extremely soft liquids and ultrathin/tiny objects. Further, the yielded bending-to-stretching energy evolution enables a Janus-faced feature, ultrastrong to lift 16,000 times its own weight, while retaining the ultra-gentleness. The scalable and material-independent design allows for a biodegradable noninvasive gripper from natural leaf. Explicitly controlled trajectories facilitate the integration with robotic arms and prostheses for challenging tasks, including grapes harvesting, zipper manipulation, and book-page turning.

In conclusion, this thesis highlights a mechanics- and mathematics-guided methodology that leverages morphological intelligence, resulting in advancements in soft manipulation specifically tailored for extreme scenarios. These demonstrated outcomes hold significant promise for diverse applications in agriculture, food processing, biomedicine, soft robotics, and the minimally invasive conservation of marine life.

Mechanics-guided Morphological Intelligence in Kirigami Structures

by
Yaoye Hong

A dissertation submitted to the Graduate Faculty of
North Carolina State University
in partial fulfillment of the
requirements for the degree of
Doctor of Philosophy

Mechanical Engineering

Raleigh, North Carolina
2023

APPROVED BY:

_____	_____
Dr. Jie Yin Committee Chair	Dr. Matthew Bryant
_____	_____
Dr. He (Helen) Huang	Dr. Irina Kogan

_____
Dr. Yong Zhu

DEDICATION

To my parents, Jiatong Hong and Shuhong Sun.

BIOGRAPHY

Yaoye Hong received his B.S. degree in Mechanical Engineering from Nanjing University of Aeronautics and Astronautics, Nanjing, China, in 2015. He received his M.S. degree in Mechanical Engineering from Boston University, Boston, U.S.A., in 2018. He joined the Dr. Jie Yin's group (Yin Lab) and had since pursuing his Ph.D. degree in Mechanical engineering. His research interests include mechanics of slender structures, mathematics-guided design of mechanical metamaterials, and their applications in soft robotics.

ACKNOWLEDGMENTS

First and foremost, I would like to express my deepest gratitude to my esteemed advisor, Dr. Jie Yin, for his unwavering guidance and support throughout not only my Ph.D. journey, but also in shaping my outlook on life. His continuous guidance and unwavering support have been instrumental in my academic and professional growth. The passion and enthusiasm he demonstrated during our research endeavors were truly contagious and have inspired me to push beyond my limits. Jie, I am incredibly grateful for everything you have done for me. Thank you from the bottom of my heart.

I would like to thank the advisory committee members, Dr. Matthew Bryant, Dr. He (Helen) Huang, Dr. Irina Kogan, and Dr. Yong Zhu, for their invaluable guidance and unwavering commitment in serving on my dissertation advisory committee. Their insightful advice and constructive feedback have played a pivotal role in elevating the quality and impact of my research.

I would like to express my sincere appreciation to Drs. Shu Yang, Po-Chun Hsu, Yong Zhu, Irina Kogan, Hao Su, and He (Helen) Huang for their invaluable guidance. I am thankful to Dr. Yi Yang, Dr. Jing Bian, Dr. Shuang Wu, Mr. Hong Chen, Mr. Joseph Berman, Mr. Ting-Hsuan Chen, Ms. Frances McBride, and Mr. Thomas Batchelder for their kind suggestions.

I would like to extend my gratitude to my lab mates, Dr. Gaojian Lin, Dr. Yichao Tang, Dr. Qiuting Zhang, Dr. Yao Zhao, Dr. Yinding Chi, Dr. Yanbin Li, Mr. Fangjie Qi, Mr. Haitao Qing, and Mr. Haoze Sun, for their support and friendship throughout my journey. I am also grateful to my fellow graduate students, Dr. Qian Dong, Dr. Zhuolei Zhang, and Dr. Xiaolei Song, for their companionship and shared experiences.

In addition, I acknowledge the support from National Science Foundation (NSF) through awarded award numbers CMMI-2005374 and 2013993.

TABLE OF CONTENTS

LIST OF TABLES

LIST OF FIGURES

CHAPTER 1

Introduction

1.1 Shape-morphing materials

Shape-programming materials from 2D thin sheets to 3D shapes have attracted broad and increasing interest in the past decades due to their novel materials properties imparted by geometrical shapes[1]. Programmable shape shifting in different materials and structures was realized at all scales utilizing folding, bending, and buckling[2]. These shape-programmable materials are attractive for broad applications in programmable machines and robots[3,4], functional biomedical devices[5], and four-dimensional (4D) printing[6,7].

1.2 Kirigami structures for shape-morphing

Kirigami, the traditional art of paper cutting, has recently emerged as a new promising approach for creating shape morphing structures and materials[8-19]. Cuts divide the original continuous thin sheets into discretized cut units without sacrificing the global structural integrity. Compared to continuous thin sheets, the kirigami sheet enables more freedom and flexibility in shape shifting through local or global deformation between cut units[17]. Starting from a thin sheet with patterned cuts, it can morph into varieties of 2D and pop-up 3D structures via rigid rotation mechanism[20] and/or out-of-plane buckling[21]. The cuts impart new properties such as auxeticity[9,11], stretchability[8,10,15,22-24], conformability[8], multistability[25], and optical chirality[26], which have found broad applications in mechanical metamaterials[11,15,27,28], stretchable devices[8,10,23,29,30], 3D mechanical self-assembly[31], tunable adhesion[32], and soft machines[17,18,33].

Despite the advance, most studies focus on the local buckling of cut units in a thin sheet patterned with arrays of parallel slits or networked triangular or square cuts etc[8-13,15,17,18],

generating quasi-3D pop-up structures without global curvatures. There are few studies on the shape shifting from a kirigami sheet to 3D shapes with intrinsic curvature[34-36]. Recent work shows that starting from a kirigami sheet or shell, 3D shapes with non-zero Gaussian curvature can be generated by utilizing either forward designs of non-periodic patterns of square cuts/cutouts[34,36] or inverse designs of tessellation of non-uniform square cuts patterning with irregular polygon cut units[35]. The local heterogeneous deformation among non-periodic tessellated cut units induces global out-of-plane buckling of the 2D kirigami sheets, thus, resulting in the formation of different 3D curved shapes[34,35]. However, it often requires programming intricate cut patterns and arrangements of non-periodic cut units, making the inverse design and optimization for target 3D shapes complicated and challenging[35,36]. In addition, how to utilize the 3D curved shapes in kirigami sheets for functionalities remains largely unexplored[34-36].

1.3 Morphological intelligence for soft robotics

The shape-shifting materials yield versatile morphologies. These morphologies lead to functional evolutions in soft robots, including locomotion, jumping, swimming, manipulating. We use the yielded evolution in soft and delicate manipulations by the morphologies to demonstrate how the morphological intelligence evolves preternatural capabilities. Soft robotic grippers have emerged as a promising approach for grasping miscellaneous objects through fluid-driven soft actuators[37-42], underactuated compliant elastomers[43], origami[44] and kirigami structures[45,46], and stimuli-responsive materials[17,47-52]. These grippers utilize their softness to adapt to the targets[41,53], facilitating pinching[45,52], enveloping[43], suction[41,44], and entangling[42] grasps. Their adaptivity enables grasping objects in a safe manner. A delicate dielectric elastomer actuator (DEA)-based gripper can grasp fragile objects[54], including a raw egg and a deformable water-filled balloon via

pinching. A hydraulic ribbon-based soft robotic gripper[39], utilizing enveloping, allows ultragentlely manipulating gelatinous organisms.

Softness enhances delicacy but forfeits strength and precision[55-58]. The delicate hydraulic[39] and DEA-based[54] grippers show low payload-to-weight ratios, reaching 1 and 80, respectively. It hinders their ability for heavy objects. To bridge the gap between softness and strength, researchers proposed several designs for achieving low-to-high grasping strength, including suction[41], fluid-driven rigidity percolation[37,53,59], and varied stiffness of stimuli-responsive materials[51,52]. For example, a five-finger-shaped gripper based on shape-memory-polymers enables manipulating heavy objects with a record-high payload-to-weight ratio up to 6400[52]. However, the gain in strength often sacrifices delicacy for nondestructive manipulation. Suction and jamming-based soft grippers cannot grasp gelatinous organisms noninvasively[37,53,59]. When objects are tiny\thin, precision grasp remains challenging[60]. To pick up small objects, extended appendages are needed, as demonstrated in the kirigami shell-based gripper capable of pinching a grain of sand[45]. For thin sheet objects, electroadhesion is often used but with limitations that require smooth and dry flat surfaces[58].

The expanding frontier of robotic-grasping applications in biomedicine, deep-sea biological conservation, prosthetics, and minimally invasive surgeries[55-58,61] requires grippers to specialize across high-requirement tasks, a substantial challenge that current grippers have not effectively addressed. For example, biofluidic manipulation requires ultradelicate grippers capable of handling extremely fragile objects such as droplets[62]. Minimally invasive surgeries require soft grippers to be high-delicate, strong, and high-precision[63]. The need for ideal robotic prosthetics requires soft robotic grippers equipped with analogous capabilities to human hands regarding dexterousness, precision, and load-carrying capacity[64]. Meanwhile, it requires soft grippers to be

lightweight and easily integrated with robotic prosthetics for simple and controllable actuation. However, the bulky systems in pneumatic or hydraulic grippers[37,39,41,42], such as pumps and tethered tubes, make it challenging.

However, given the tradeoff between delicacy, strength, and precision, it remains challenging to simultaneously achieve high delicacy, high strength, and high precision in a single soft gripper[58,65] (see Methods for summary of representative soft grippers). One potential solution is the shape-morphing kirigami approach[45,46]. Inspired by the kirigami approach[45], our recent work in design of an encapsulating gripper takes a step toward a potential solution[46]. We demonstrated its proof-of-concept applications in manually picking a raw egg yolk nondestructively, a human hair, and heavy objects with a payload-to-weight ratio up to 1000[46]. It underscores the significance of morphologies in potentially mitigating the tradeoff challenges. However, its performance still falls short of achieving the goal of an extraordinary soft gripper that specializes across the versatile high-requirement tasks mentioned above. Several challenges necessitate further exploration. These include effectively handling objects even more delicate than the reported water-filled balloon[54] and raw egg yolk[46], such as water droplets. Addressing the manipulation of micro-size and thin objects thinner than a human hair that requires ultraprecision, and accommodating ultra-heavy objects that may surpass the reported record-high payload-to-weight ratio of 6400[52], as well as the potential integration of the gripper with prosthetic hands for multifunctions, pose significant hurdles.

Another potential solution is to mimic natural organisms, which balance this tradeoff by morphing with nastic trajectories to perform grasping and climbing, e.g., cucumber tendrils and cephalopod tentacles[66]. Soft grippers aim to imitate their shapes, but few explore the potential of the nastic trajectory for exceptional grasping capabilities[67]. Previous studies in soft grippers

emphasize the adaptive morphologies for improved capabilities[58,65]. Their grasping trajectories receive less attention and remain largely unexplored[68]. However, the significance of the trajectory should not be overlooked, as it profoundly influences the gripper's performance, especially when dealing with noninvasive manipulation of fragile objects and precision grasping of small/thin objects[58]. Explicitly programming trajectories pose challenges due to the inherent complexities arising from the nonlinear deformations in compliant structures[69].

1.4 Outline of the thesis

The thesis is organized as follows:

Chapter 2 reports programming the curvature of cut boundaries in kirigami sheets for target 3D curved morphologies through both forward and inverse designs. This strategy largely simplifies the inverse design. Leveraging this strategy, we demonstrate its potential applications as dynamically conformable heaters for human knees. This study opens a new avenue to encode boundary curvatures for shape-programing materials with potential applications in soft robotics and wearable devices.

Chapter 3 illustrates how adjusting the geometric constructions of coupled ribbons in kirigami structures enables the creation of nastic wavy shapes. It presents an analytical framework that facilitates the prediction and program of the morphology of interconnected ribbons. This approach leverages mechanical shape evolutions rather than relying on material or chemical interventions to naturally induce curved and undulating shapes. The findings from this research hold significant potential for a wide range of applications in biological systems and the development of soft machines.

Chapter 4 first demonstrates a noninvasive kirigami-based gripper for gelatinous organisms realized by programmable morphologies. Then, it reports how the morphological intelligence enables kirigami-based grippers to evolve into a deployable kirigami-based soft gripper that can simultaneously achieve ultragentle, ultradelicate, and ultrastrong manipulation capabilities. Such multi-capability stems from its trajectory and mechanical responses that are rationalized through experiments, finite element simulations, and analytical modeling. Programming the morphology and trajectory of the gripper enables ultragentle and ultradelicate grasping of extremely soft (e.g., a liquid drop and a gelatinous jellyfish), ultrathin/tiny (e.g., a 4 μm-thick polymer sheet and a 2-μm-diameter fiber), ultrasharp (e.g., granular sharp medical waste), and other objects. Further, the bending-to-stretching energy evolution yielded by the morphologies enables a Janus-faced feature, i.e., ultragentle to perform a 0.0468 kPa contact pressure in noninvasive tasks and ultrastrong to lift and hold a deadweight of 6.4kg, 16,000 times the weight of the gripper. Leveraging the scalability and materials independence of the kirigami design, we further demonstrate a biodegradable and noninvasive gripper made of a bare leaf and thin wood plates. Lastly, we demonstrate its easy integration with both commercial robotic arms and prosthesis hands for accomplishing challenging tasks such as picking grapes from a vine, turning a book page, and folding cloth. It has broad potential applications in biomedicine, agriculture, food processing, deep-sea exploration, prosthesis, and minimally invasive surgeries.

Chapter 5 reports the conclusions of this work and anticipates some potential works about the thesis.

CHAPTER 2

Boundary curvature guided programmable morphologies in kirigami sheets

Note: This Chapter was partially adapted and modified from the publication below: Hong, Y. et al. Boundary curvature guided programmable shape-morphing kirigami sheets. *Nature Communications* **13**, 530 (2022).

2.1 Introduction

From the perspective of analytics, the curvature of a boundary can be harnessed to tune 3D curved shapes based on the classical Gauss-Bonnet theorem in differential geometry[70], which correlates the Gaussian curvature and the geodesic curvature along the boundary (i.e., the projection of boundary curvature). Motivated by this theorem, here, we propose a simple strategy of utilizing the boundary curvature of cut edges rather than complex cut patterns to program 3D curved shapes through both forward and inverse designs. In contrast to previous networked polygon cut units with square cut patterning[8,11,34-36], our kirigami sheet is composed of parallel discrete ribbons enclosed by continuous boundaries (Fig. 2.1) through simple patterning of parallel cuts. We demonstrated that simply stretching the kirigami sheet with prescribed curved cut boundaries could generate varieties of well-predicted 3D curved shapes with positive, negative, and zero Gaussian curvatures and their combinations. We proposed a straightforward inverse design strategy for target 3D curved shapes, avoiding the necessity of shape optimization by building on top of theoretical insights from applying the Gauss-Bonnet theorem to the geodesic ribbons. Leveraging this, we demonstrated their potential applications in designing a biomimetic conformable heating pad with intrinsic adaptivity for human knees in this chapter.

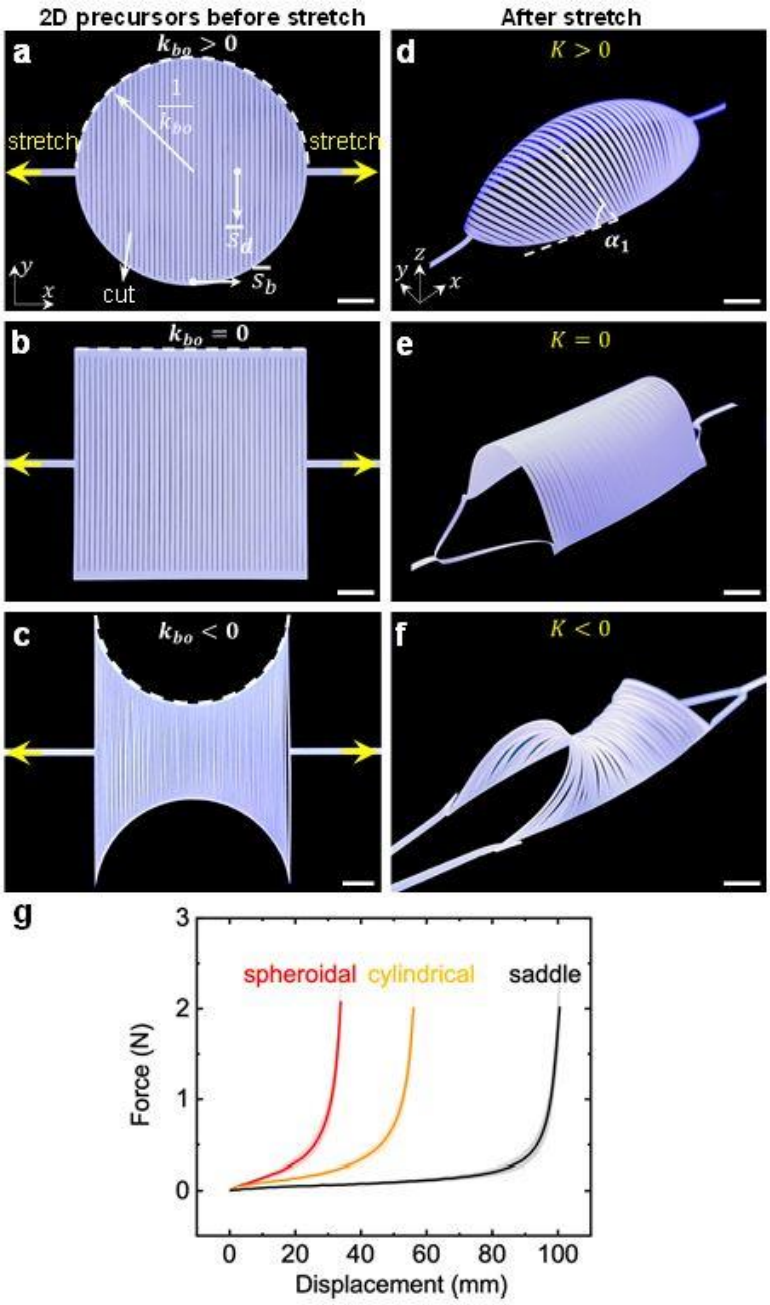

Fig. 2.1 Shape shifting of 3D curved morphologies from 2D kirigami sheets with different cut boundary curvatures subject to uniaxial tension. a-c 2D precursors of three kirigami sheets patterned with parallel cuts but different boundary curvatures k_b highlighted in dashed white curves. circular (a), square (b), biconcave (c) samples with positive, zero, and negative boundary curvature, respectively. d-f The corresponding formed 3D curved shapes with different Gaussian curvature K. d Spheroidal shape with $K > 0$ at an applied strain of 0.30. e Cylindrical shape with $K = 0$ at an applied strain of 0.65. f Saddle shape with $K < 0$ at an applied strain of 1.47. Scale bars = 10 mm. g Force-displacement curves for the three 2D precursors. The shaded areas are the standard deviation between four different tests.

2.2 Manipulating 2D boundary curvatures for 3D curved morphologies

The classical Gauss-Bonnet theorem[70] correlates the boundary curvature with the global Gaussian curvature *K*. Motivated by the theorem, as shown in Fig. 2.1, we start by designing the 2D precursors of kirigami sheets with different boundary curvatures k_{bo} to exploit its effects on the Gaussian curvature of their 3D deployed shapes, where k_{bo} is set to be positive (circular boundary), zero (rectangular boundary), and negative (biconcave circular boundary), respectively. We use the polyethylene terephthalate (PET) sheet with Young's modulus of 3.5 GPa, Poisson's ratio of 0.38, and thickness of 127 μm to fabricate the kirigami sheets using laser cutting. The thin sheets are cut into a number of discrete parallel thin ribbons enclosed by continuous boundary ribbon.

Fig. 2.1 show that stretching the 2D precursors leads to distinct spheroidal, cylindrical, and saddle shapes with positive, zero, and negative Gaussian curvature *K*, respectively. Upon stretching, the boundary ribbon starts bending and compresses the enclosed discrete ribbons to induce their out-of-plane buckling. Thus, it renders a 3D pop-up morphology. Once the 3D shape is formed, the global shape will not change but with its magnitude of curvature increasing with the applied strain. The three samples exhibit similar J-shaped force-displacement curves as shown in Fig. 2.1, where the force increases approximately linearly with the initial displacement due to the bending-dominated deformation in the discrete ribbons, followed by the steep rise arising from the stretching-dominated deformation in the boundary ribbon. Such stiffness strengthening mechanical responses are similar to that observed in the kirigami sheet patterned with orthogonal square cuts[24]. Among the three samples, the circular one morphing into a spheroidal shape shows the highest stiffness and the least stretchability, while the biconcave one deforming into a saddle shape is the most compliant and stretchable (Fig. 2.1).

We note that distinct from the kirigami sheets composed of networked polygon cut units in previous studies [8,11,34-36] or discrete structures composed of disconnected non-geodesic ribbons [71], the simple design of parallel cuts in this work endows the unique characteristic, i.e., parallel cuts make each discrete ribbon a geodesic curve of the morphed morphologies. It will facilitate the inverse design and dynamically programming morphologies, as discussed later.

By extending the classical Gauss-Bonnet theorem in differential geometry to the two neighboring enclosed ribbons and the multiple-connected enclosed kirigami surface morphology, we can qualitatively explain the observed 3D curved shapes and their dynamic shape morphing. Mathematically, for the morphed 3D pop-up morphologies, the theorem can be simplified as

$$\int_{\Omega} KdA + \oint_{\partial\Omega} k_{gb}\, ds = C \tag{2-1}$$

where the constant $C = 2\pi\chi(\Omega) - \sum_{i=1}^{p} \theta_i$ with $\chi(\Omega)$ and θ_i denoting the Euler characteristic of the Riemannian manifold Ω with boundary $\partial\Omega$ and the exterior angles at the vertices of the manifold, respectively. C remains unchanged during shape shifting. k_{gb} is the geodesic curvature along the boundary ribbon according to the Meusnier theorem[70], i.e., the projection of the deformed boundary curvature k_b with φ being the projection angle.

For the 2D kirigami precursor with positive boundary curvature, i.e., $k_{bo} > 0$, we have $C = \oint_{\partial\Omega_o} k_{gb}\, ds$ by setting $K = 0$ with Ω_o denoting the manifold before deformation. After deformation, for the deformed manifold Ω', we have $\int_{\Omega'} KdA = C - \oint_{\partial\Omega'} k_{gb}\, ds = \oint_{\partial\Omega_o} k_{gb}\, ds - \oint_{\partial\Omega'} k_{gb}\, ds$ in terms of Eq. (2-1). As the applied strain increases, both k_b and sin φ decrease, which results in a decreased geodesic curvature k_{gb}, and consequently $\int_{\Omega'} KdA > 0$. Given the C^2 continuous boundary curves in the three characteristic precursors (C^2 continuity means that both the first and second derivatives of the curves are continuous, i.e., continuous in curvature), both $\int_{\Omega'} KdA$ and K will be simultaneously positive or negative. Thus, we have a globally positive K in the deformed

manifold Ω', i.e., $K > 0$ in Ω', which is consistent with the observed spheroidal shape in Fig. 2.1. Similarly, for the 2D precursor with $k_{bo} < 0$, as the strain increases, the absolute value of the boundary curvature $|k_b|$ becomes smaller and sin φ decreases, which results in an increased geodesic curvature. Thus, we have the generated saddle shape with globally $K < 0$ in Fig. 2.1. For the 2D precursor with $k_{bo} = 0$, during the deformation, $k_{bo} = 0$ does not change, which leads to a zero geodesic curvature. Thus, we have a cylindrical shape with $K = 0$ in Fig. 2.1.

2.3 Analytical modeling and simulation on 3D shape shifting

To quantify the shape shifting of the kirigami structures with the applied strain, we combine both analytical modeling and finite element method (FEM) simulation to predict their morphology changes. The deformation of the kirigami structures is dominated by bending of the discrete ribbons, where the elastic strain energy in the boundary ribbon is negligible due to its small width. Thus, all the discrete ribbons share similar deformed elastica shapes[72-75]. The deformed 3D shape at an applied strain ε can be described by $\tilde{r}_s(\bar{s}_b, \bar{s}_d) = (\bar{x}(\bar{s}_b, \bar{s}_d), \bar{y}(\bar{s}_b, \bar{s}_d), \bar{z}(\bar{s}_b, \bar{s}_d))$, where $\bar{s}_b$ and $\bar{s}_d$ denote the normalized arc length coordinate of the boundary and the discrete ribbon as illustrated in Fig. 2.1, respectively. $(\bar{x}, \bar{y}, \bar{z})$ denote the Cartesian coordinates of any point $P(\bar{s}_b, \bar{s}_d)$ on the surface with its origin set at the center of the 2D precursor. Considering the deformed surface shape foliated by continuously varying discrete ribbons along the boundary, its generalized shape functions can be expressed as

$$\bar{x}(\bar{s}_b, \bar{s}_d) = \frac{2m}{\lambda} CN(\lambda \bar{s}_d, m) \cos \alpha_1 + f(\bar{s}_b, \varepsilon) \tag{2-2}$$

$$\bar{y}(\bar{s}_b, \bar{s}_d) = \frac{2}{\lambda} E(AM(\lambda \bar{s}_d, m), m) - \bar{s}_d \tag{2-3}$$

$$\bar{z}(\bar{s}_b, \bar{s}_d) = \frac{2m}{\lambda} CN(\lambda \bar{s}_d, m) \sin \alpha_1 \tag{2-4}$$

by sweeping the varying discrete ribbons modeled as an elastica shape along the boundary. $m = m(\bar{s}_b, \varepsilon)$ is the elliptical modulus that characterizes the bending deformation of a discrete ribbon. $\lambda = \frac{2F(\frac{\pi}{2},m)}{\bar{l}_d}$ is related to the normalized length $\bar{l}_d$of the discrete ribbon. *AM* and *CN* denote the Jacobian amplitude and the elliptic cosine, respectively. *E* and *F* denote the incomplete elliptic integral of the second kind and the first kind, respectively. $\alpha_1 = \alpha_1(\bar{s}_b, \varepsilon)$ is the tilting angle of the discrete ribbon with respect to the horizontal plane (i.e., *xy* plane) as shown in Fig. 2.1, which varies from 0 to 180^o depending on its boundary location and the applied strain. $f(\bar{s}_b, \varepsilon)$ describes the *x* coordinate at $\bar{s}_b$ of the deformed boundary ribbon.

Without losing generality, we can use three profiles from the front view, top view, and side view to characterize the 3D shape shifting with the applied strain (Fig. 2.2 for spheroidal and saddle shapes). The front view shows the backbone profile on the *xz* plane, which can be predicted by $\bar{x}_{bb} = \frac{2m}{\lambda} cos\, \alpha_1 + f(\bar{s}_b, \varepsilon)$ and $\bar{z}_{bb} = \frac{2m}{\lambda} sin\, \alpha_1$ after setting $\bar{s}_d$= 0 and $\bar{y}$= 0 in Eqs. (2-2)-(2-4). The top-view profile shows the deformed shape of the boundary ribbon (Fig. 2.2) that remains in the *xy* plane during deformation by setting $\bar{z}$= 0 in Eqs. (2-2)-(2-4), which can be parametrized by

$$\tilde{r}_b(\bar{s}_b, \varepsilon) = (\bar{x}, \bar{y}, 0) = (f(\bar{s}_b, \varepsilon), g(\bar{s}_b, \varepsilon), 0) \tag{2-5}$$

where

$$g(\bar{s}_b, \varepsilon) = \left[\frac{2E\left(\frac{\pi}{2},m\right)}{F\left(\frac{\pi}{2},m\right)} - 1\right] g(\bar{s}_b, 0) \tag{2-6}$$

describes the *y* coordinate at $\bar{s}_b$ of the deformed boundary ribbon at the strain of ε. Eq. (2-6) describes the relationship between *m* and ε. Thus, combining Eqs. (2-2)-(2-4) and Eq. (2-6) will determine the unknown parameters of $\bar{x}$, $\bar{y}$, $\bar{z}$, and *m* to predict the deformed 3D shapes with the applied strain. The side view shows the projection of similar elastica shapes of discrete ribbons

onto the *yz* plane (Fig. 2.2), which depends on *m* and the tilting angle of the longest discrete ribbon. Its deformed elastica shape can be expressed by $\bar{y}_d = \frac{2}{\lambda}E(AM(\lambda\bar{s}_d, m), m) - \bar{s}_d$ and $\bar{z}_d = \frac{2m}{\lambda}CN(\lambda\bar{s}_d, m)$, where the length of the discrete ribbons is assumed to be unchanged during deformation.

Next, we apply both the generalized analytical model and FEM simulation to analyze the 3D shape shifting in the specific examples shown in Fig. 2.1. Fig. 2.2 theoretically predict the variation of the three profiled shapes with the applied strain ε during the formation of a spheroidal shape. As ε increases from 0 to 0.4, top-view profiles show that the circular boundary gradually deforms into an elliptical shape (Fig. 2.2), where we have $f(\bar{s}_b, \varepsilon) = (1 - \bar{w})\sin s_b + \bar{v}\cos s_b$ and $g(\bar{s}_b, \varepsilon) = (1 - \bar{w})\cos s_b - \bar{v}\sin s_b$ ($\bar{s}_b \in [-\frac{\pi}{2}, \frac{\pi}{2}]$) in the model. $\bar{w}(\bar{s}_b, \varepsilon)$ and $\bar{v}(\bar{s}_b, \varepsilon)$ denote the radial and tangential displacement of the boundary ribbon[76], respectively. Correspondingly, the compressed discrete ribbons deform into an elastica shape (Fig. 2.2). The backbone expands and shows an elliptical profile (front view in Fig. 2.2). As shown in Fig. 2.2, the superposition of the three theoretically predicted front-view, top-view, and side-view profiles (highlighted in purple color) with images retrieved from the experimental observation at ε = 0.3 shows an excellent agreement. The corresponding FEM simulated deformed 3D shape shows an excellent overlapping with the experiment (Fig. 2.2). Differently, during the formation of the cylindrical shape, both the boundary ribbon and backbone profile remain straight during deformation and all the discrete ribbons take the same elastic shape, the modeling of which is consistent with both experiments and FEM simulation.

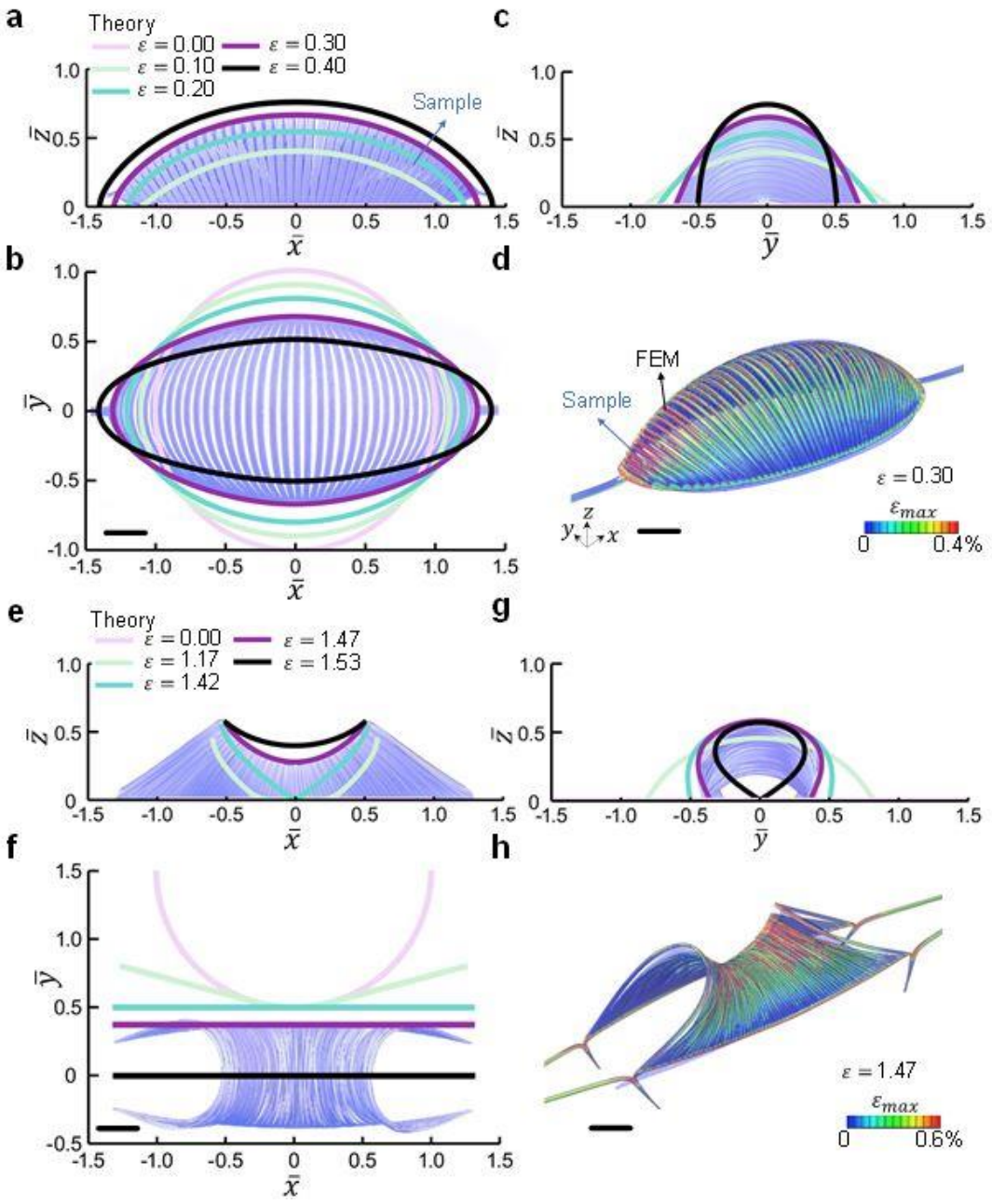

Fig. 2.2 Quantifying the 3D shape shifting through analytical modeling and simulation. a-h Predicted shape changes with the applied strain ε in the samples of spheroidal (a-d) and saddle shapes (e-h). a and e are the front-view profile. b and f are the top-view profile. c and g are the side-view profile. d and h are the overlapping of FEM simulation results (contours of the maximum principal strain ε_{max}) with the experimental image at ε = 0.30 (d) and 1.47 (h). Scale bars = 10 mm.

Fig. 2.2 shows the predicted shape change during the formation of a saddle shape. In contrast to simultaneous buckling in generating the spheroidal and cylindrical shapes, we observe a sequential buckling during the formation of the saddle shape in experiments. The discrete ribbons near two stretching ends pop up first, followed by the ribbons in the center when beyond a critical strain ε_c. The physical origin of the sequential buckling is due to the coupling effects of the concave boundary geometry and different critical buckling forces of the discrete ribbons, where the curvature varies sequentially during deformation along the boundary ribbon from its two ends to the center (Fig. 2.2). Such sequential buckling behavior disappears for the large radius of curvature since the 2D precursor is close to a rectangle shape. As the applied strain further increases, the discrete ribbons contact with each other, leading to structural frustration. Reducing the number of ribbons facilitates a frustration-free structure without self-contact. Such a sequential shape shifting is well captured by both the analytical model and FEM simulation. As predicted by the model, Fig. 2.2 shows that at the critical strain $\varepsilon_c \approx 1.42$, the initial concave boundary ribbon deforms into a straight line and remains straight upon further deformation, where we have $f(\bar{s}_b, \varepsilon) = \bar{s}_b$ and $g(\bar{s}_b, \varepsilon) = \sqrt{1.46 - (\varepsilon - 0.32)^2}$ with $\bar{s}_b \in [-1.32, 1.32]$ in the model. Correspondingly, the backbone profile (Fig. 2.2) transits from an initial sharp V shape to a smooth concave shape, which exhibits a sudden jump of the displacement along the z-axis when the applied strain is slightly beyond ε_c. Further stretching results in the formation of the saddle shape with a concave backbone, which is consistent with both experiments (Fig. 2.2) and FEM simulation results.

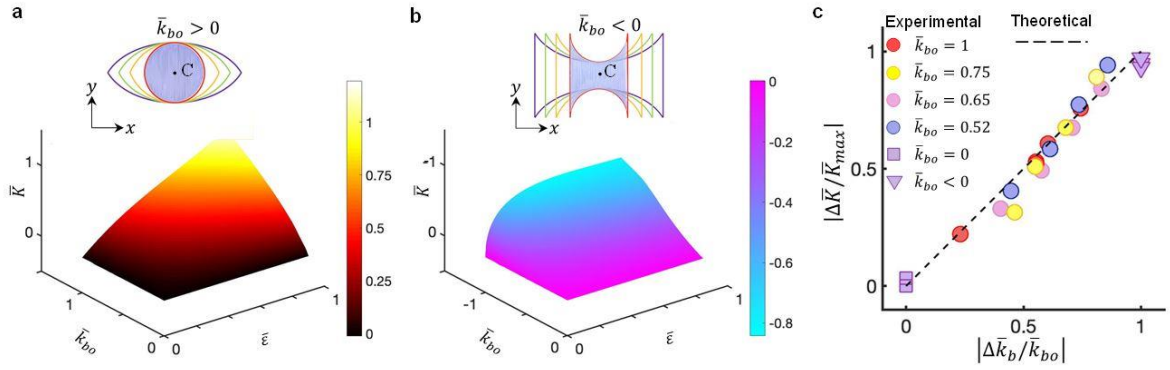

Fig. 2.3 Quantifying the correlation between the boundary curvature and the Gaussian curvature. a-b Theoretically predicted 3D maps of the normalized Gaussian curvature $\bar{K}$ at the center point C as a function of the normalized boundary curvature $\bar{k}_{bo}$ in 2D kirigami precursors (insets) and the applied strain ε for the cases of spherical (a) and saddle (b) shapes. The color bars represent the normalized Gaussian curvature. c Theoretical and experimental results of the approximately linear relationship between the normalized variation of the Gaussian curvature $|\frac{\Delta\bar{K}}{\bar{K}_{max}}$ and the normalized variation of the boundary curvature $|\frac{\Delta\bar{k}_b}{\bar{k}_{bo}}|$.

2.4 Quantitative correlation between the boundary curvature and the Gaussian curvature

Based on the validated theoretical model, we further establish the general quantitative correlation between the boundary curvature k_{bo} of 2D kirigami precursors and the Gaussian curvature K of their popped 3D morphologies at a given applied strain. Fig. 2.3 show the theoretically predicted 3D maps of the normalized Gaussian curvature $\bar{K}$ at the center point $C(\bar{s}_b = 0, \bar{s}_d = 0)$ as a function of both normalized boundary curvature $\bar{k}_{bo}$ (see illustration of tuning different k_{bo} in the insets of Fig. 2.3) and applied strain $\bar{\varepsilon}$. It shows that for 2D kirigami precursors with either positive (Fig. 2.3) or negative boundary curvature, generally, the absolute value of $\bar{K}$ increases with an increasing strain $\bar{\varepsilon}$ and $|\bar{k}_{bo}|$. Note that for the formed saddle shapes, we have $\bar{K}$ = 0 before reaching the critical strain ε_c. At the onset of ε_c, $\bar{K}$ suddenly decreases due to a dramatic increase in the boundary curvature. Beyond ε_c, $\bar{K}$ barely changes because the boundary ribbon remains straight (Fig. 2.3). Interestingly, Fig. 2.3 shows that theoretically, the

normalized variation of Gaussian curvature $\left|\frac{\Delta\bar{K}}{\bar{K}_{max}}\right|$ increases approximately linearly with the normalized variation of boundary curvature $\left|\frac{\Delta\bar{k}_b}{\bar{k}_{bo}}\right|$ (slope ≈ 1), i.e.,

$$\frac{\left|\frac{\Delta\bar{K}}{\bar{K}_{max}}\right|}{\left|\frac{\Delta\bar{k}_b}{\bar{k}_{bo}}\right|} = \frac{4m^2\bar{k}_{bo}}{\left[\bar{k}_{bo}\bar{x}^2\left(\frac{\gamma}{\bar{k}_{bo}},0\right)-\bar{y}(0,1)\right]\bar{K}_{max}} \approx 1 \tag{2-7}$$

which is consistent with experimental measurements. $\bar{K}_{max}$ is the maximum Gaussian curvature at the center point, and γ denotes half of the central angle of the boundary curve. Note that there are few data points for the square and biconcave shapes because the cylinder and the saddle shape have zero and sudden-jumping Gaussian curvature, respectively. Specifically, this near-linear relationship holds regardless of the initial boundary curvature of a 2D kirigami precursor, which can be harnessed to program the morphology and the dynamic deployment trajectories.

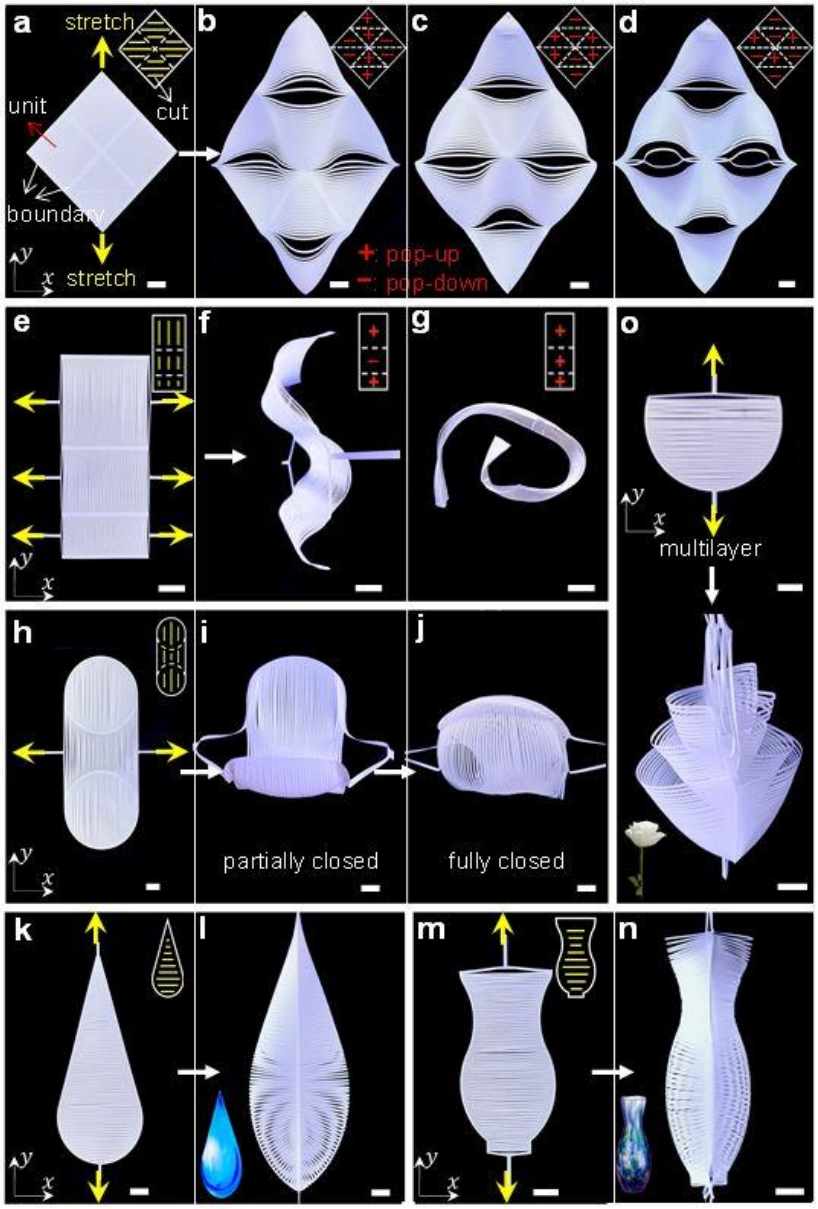

Fig. 2.4 Combinatorial designs of 2D kirigami precursors for complex 3D shapes under uniaxial tension. a-j Reconfigurable 3D shapes through bistability of discrete ribbons. a 2D precursor composed of 2 × 2 square units with zero boundary curvature. b-d uni-axial stretching induced reconfigurable human face-like morphologies with switchable smiley (b) and sad (c) expressions, as well as eyeglasses (d) by tuning the popping directions of ribbons (insets). e 2D precursor composed of 3 × 1 rectangle units with zero boundary curvature. f-g Formation of switchable sinusoidal wavy and coiled shapes. h 2D precursor composed of an array of two circular units bridged with a biconcave unit. i-j Formation of a 3D encapsulated Venus flytrap-like shape through uniaxial stretching. k-n Formation of a 3D droplet-like shape (l) and vase-like shape (n) by uni-axially stretching 2D precursors with different combined boundary curvatures (k, m). Insets show the image of a droplet and a vase. o Formation of a flower-like shape by uni-axially stretching multiple layers of semi-circular 2D precursors. Scale bars =10 mm.

2.5 Combinatorial designs for more complex 3D shapes

Next, equipped with the knowledge of the correlation between the boundary curvature and the deformed 3D shapes, we extend it to achieve more varieties of 3D shape-morphing morphologies through tuning the smoothness of the boundary curves of individual units in combinatorial and tessellated designs (Fig. 2.4).

We first explore the 3D shape shifting in 2D kirigami precursors through tessellating the three basic units in Fig. 2.1. Fig. 2.4 shows a 2D diamond-shaped kirigami precursor composed of tessellated 2 × 2 square units with zero boundary curvature. Each unit has the same parallel cut pattern. Upon vertically stretching the 2D diamond precursor along the *y*-axis, both top and bottom square units pop up spontaneously (represented by the symbol of "+" in the inset of Fig. 2.4) via out-of-plane buckling while the square units on two sides pop down (denoted by the symbol of "–"), generating a smiley 3D human face-like morphology (Fig. 2.4). Note that both the inner and outer boundaries of an individual unit in the combinatorial design still belong to the cut boundaries following our model, both of which contribute to the geodesic curvature k_{gb} in Eq. (2-1) and satisfy the Gauss-Bonnet theorem locally and globally. Specifically, the eyes and mouth in the form of a hole are formed due to its discontinuous slope (changed smoothness) at the intersections of boundaries, which results in a localized non-zero Gaussian curvature. This is also consistent with the Gauss-Bonnet theorem, where the localized non-zero Gaussian curvature arises from the localized curvature change (variation of the exterior angle in Eq. (2-1)) of the C^0 smooth inner and outer boundary curves of the units. The holes divide the face into eight independent popping regions (e.g., forehead, eyes, nose, cheek, mouth, and chin). We note that the face will not change its pattern under different loading rates. Similarly, stretching an array of 3 × 1 rectangle units with identical parallel cuts and zero boundary curvature (Fig. 2.4) along the *x*-axis leads to a sinusoidal

wavy shape with zero Gaussian curvature. Furthermore, Fig. 2.4 shows that two circular units with positive boundary curvatures bridged with a biconcave unit with negative boundary curvatures form a vertically tessellated 2D precursor. Stretching the 2D precursor along the *x*-axis generates an increasingly enclosing 3D shape, where the two circular units pop up into a spheroidal shape with positive Gaussian curvature while the concave unit buckle into a saddle shape with negative Gaussian curvature (Fig. 2.4). As the stretching strain further increases, their two end circular boundaries contact with each other, forming an encapsulated Venus flytrap-like structure (Fig. 2.4) that could be used for delicate grippers, as discussed later.

We note that given the combinatorial design of units and the bistability in each unit, the formed 3D shapes in the kirigami sheets could be further reconfigured to other distinct 3D morphologies via the bistability switch [25] in the buckled discrete ribbons locally or globally, where each ribbon could pop up or pop down independently and locally. For example, manipulating the bistable switch in eight independent popping regions of the human face-like morphology in Fig. 2.4, i.e., the popping directions of discrete ribbons in each region, could generate more potential facial expressions. As a proof of concept, manually flipping all the popping directions in the eight regions of the smiley face under the stretched state generates a sad face (Fig. 2.4), which can be reversibly switched to the smiley face. Furthermore, localized flipping of two single ribbons in the eye area generates a face with eyeglasses (Fig. 2.4). The bistable states of the ribbons could be either manually switched[25] or potentially remotely tuned using the magnetic field. Similarly, Fig. 2.4 shows that flipping the popping direction in the central unit of the sinusoidal wavy shape makes it reconfigure into a coiled shape, which could be reversibly switched by flipping back the popping direction.

More complex 3D shapes can be generated by combining boundary curvatures with different smoothness in stacked 2D kirigami precursors (Fig. 2.4) under uni-axial mechanical stretching, e.g., a 3D droplet-like shape and a vase-like shape. We note that the smoothness of the backbone in the generated 3D shapes is controlled by the smoothness of the boundary in their corresponding 2D precursors, which makes the combinatorial design easy to handle. To generate the water droplet shape, we design a 2D precursor consisting of combined a straight line and a circular arc to mimic the 3D water droplet's backbone shape (Fig. 2.4). Similarly, the vase-like shape is generated by stretching two stacked 2D precursors composed of a concave and convex boundary. Furthermore, stretching multiple layers of similar semi-circular 2D precursors generates a flower-like shape with multilayer pedals.

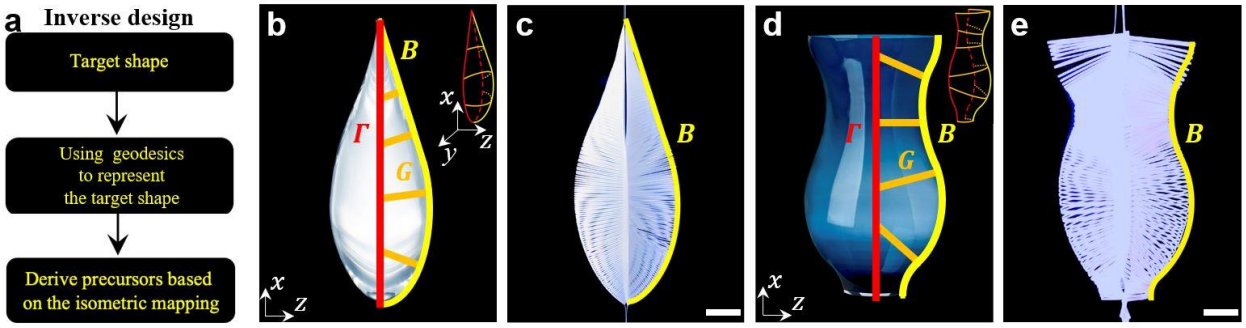

Fig. 2.5 Inverse design of 3D shapes. a Flow diagram of the inverse design. b Schematic of using curves to approximate and represent the target shape (side view of a waterdrop). The inset shows an isometric view. Red, orange, and yellow curves are the boundary curve Γ, geodesic curve G, and backbone curve B, respectively. c Experimental inverse-design result of the waterdrop shape formed by a 2D kirigami precursor subject to uniaxial tension. The yellow curve is the backbone in the target shape. d Schematic of using curves to approximate and represent the target shape (side view of a vase), with an isometric view showing in the inset. e Experimental inverse-design result of the vase shape formed by a 2D precursor subject to uniaxial tension. Scale bars = 10 mm.

2.6 Inverse design strategy

Existing methods of inverse design for target 3D curved shapes using the kirigami approach require complex algorithms to program heterogeneous local deformation among networked cut

units [35,36]. Based on the information that discrete ribbons are geodesic curves of the deformed 3D shapes, we propose a straightforward inverse design strategy. It utilizes the geodesic curves extracted from the target shapes and the isometric mapping to prescribe the 2D precursors (Fig. 2.5), which is, in principle, applicable to any target configuration.

To illustrate the strategy, we use the target shapes of a water droplet and a vase (Fig. 2.5) as two examples for the inverse design of the 2D kirigami precursors. As shown in Fig. 2.5, we first approximate and represent the target shapes by deriving the shape functions of the backbone curve *B* (highlighted in yellow color), the geodesic curves *G* (highlighted in orange color) approximated by elastica curves, and the boundary curve Γ (highlighted in red color). Next, based on the isometric mapping from *G* and Γ in the target shape to the 2D precursor, we derive the shape function of the prescribed 2D boundary curve Γ^P. The parametrization of Γ and Γ^P can be expressed in the form of $\tilde{r}_\Gamma = (x(s_b), y(s_b), 0)$ and $\tilde{r}_{\Gamma^P} = (x^P(s_b), y^P(s_b), 0)$, respectively, where the superscript *P* represents the 2D precursor. Accordingly, the shape function of the boundary curve Γ^P in the 2D precursor can be derived as

$$\begin{Bmatrix} x^P(s_b) \\ y^P(s_b) \end{Bmatrix} = \begin{bmatrix} \eta_x & 0 \\ 0 & \eta_y \end{bmatrix} \begin{Bmatrix} x(s_b) \\ y(s_b) \end{Bmatrix} \tag{2-8}$$

where the parameters η_x and η_y are related to the isometric mapping. Furthermore, the required strain ε_{re} to form the target shape is given by $\varepsilon_{re} = \frac{[x(max(s_b)) - x^P(max(s_b))]}{x^P(max(s_b))}$ with max(s_b) being the maximum arc length of the boundary ribbon.

Fig. 2.5 shows the result of the inverse design of a water droplet and a vase after deploying the derived 2D kirigami precursors at an applied strain of ε_{re} = 0.14 and 0.07, respectively. The inverse design result agrees well with the target shape denoted by the yellow curves. We note that for a target discrete 3D curved shape, previous studies using the assembly of disconnected non-

geodesic ribbons without an enclosed boundary need complicated control and optimization of geometry and distribution of each ribbon locally and globally in the inverse design[71]. Notably, precise control of all the geodesic ribbons and shape optimization are not necessary for our proposed inverse design approach since it harnesses the isometric mapping of geodesics and only needs the information of one representative geodesic curve and one boundary curve in the target surface. Thus, such a strategy could significantly simplify the calculation. Moreover, programming the dynamic shape-shifting morphology of the global geometric entity in our design is limited to only one variable, i.e., the boundary curvature in terms of Eq. (2-7). Only geodesic ribbons have zero geodesic curvatures, and their curvatures are the normal curvatures on the morphed surface, where the easy-to-handle global dynamic program arises naturally. It does not require the trivial control and optimization of the heterogeneous deformation of the polygons in networked kirigami structures[35,36] or the thickness distribution of each non-geodesic ribbon in a discretized manner[71].

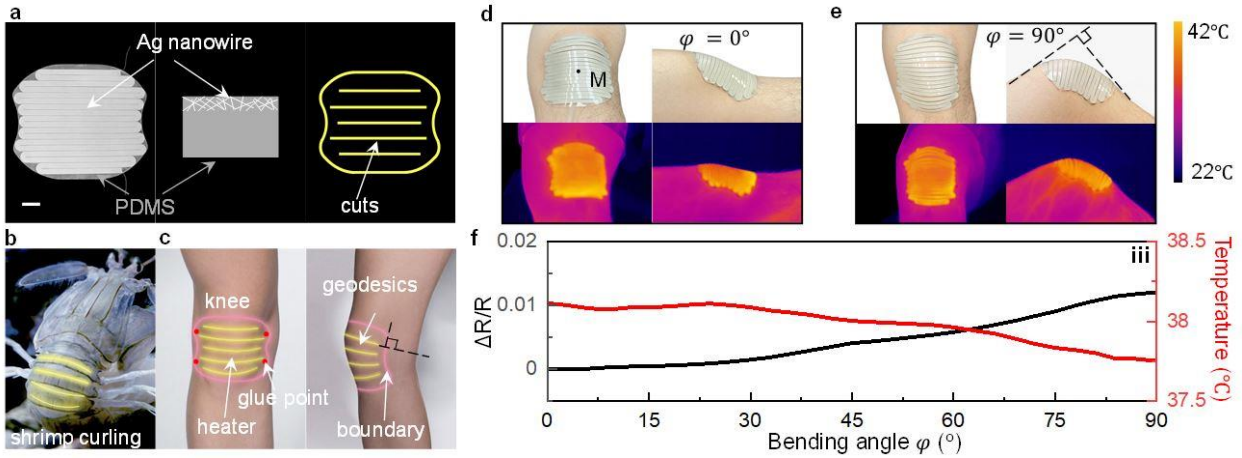

Fig. 2.6 Dynamically conformable biomimetic heater. a Photograph of the 2D precursor. Scale bar: 10 mm. The right shows the schematics of the cross-section of the AgNW/PDMS heater and the cut pattern. b-c Schematics of the heater mimicking the shell of the Mantis shrimp composed of geodesics attached to the human knee. b Curling shell of the Mantis shrimp. Yellow lines represent geodesics. c Schematic of the heater attached to the knee. Pink and yellow lines are the boundary and the geodesics, respectively. Red dots are the points with the adhesive. Black dashed lines representing the geodesics are perpendicular to the boundary with the knee bending. d-e The kirigami heater deforms with the knee as the knee bends from 0^o (d) to 90^o (e) and the corresponding thermal image upon heating. φ denotes the bending angle of the knee. M is the center of the knee. The color bar represents the temperature. f Electric resistance of the heater and the temperature of the point M as a function of the bending angle φ.

2.7 Application as a conformable heater composed of the geodesic ribbons

Conformable heating devices are desired for human joints to relieve pain[77]. The inhomogeneous deformation and complex curved shapes[78] of the joints, such as the human knee, result in the trade-off between the large contact area (between the device and the human skin) and the conformability and adaptivity, especially during motion. Here, different from existing heaters[32,79,80] , we harness the correlation between the boundary curvature and the 3D morphology and demonstrate an electrically driven resistive human-knee heater mimicking the conformability of the Mantis shrimp's shell. It shows intrinsic adaptivity with decent conformability and large-area uniform-heating capability.

As shown in Fig. 2.6, the heater is composed of silver nanowires (AgNWs)[81,82] and the PDMS (polydimethylsiloxane) kirigami sheet with parallel cuts. It generates Joule heating with a constant direct current applied. Mimicking the curling shell of the Mantis shrimp (Fig. 2.6), the heater includes discrete ribbons that are consistent with the geodesics of the knee, which are normal to the boundary. Four vertices of the kirigami AgNW-PDMS pad are bonded to the knee, as shown in Fig. 2.6. As the knee bends from 0 to 90^{o}, the discrete ribbons deform induced by the variation of the boundary curvature like the curling of the shell of the shrimp (Fig. 2.6). The geodesic feature, same as the shell, endows intrinsic adaptivity, and the heater shows decent conformability and uniform-heating capability, where the standard deviation of the temperature across the knee before and after bending is 0.73 °C and 0.97 °C, respectively (Fig. 2.6). With the increase of the bending angle φ, the temperature at the center of the heater (point M in Fig. 2.6) slightly decreases, resulting from the small increase in the resistance of AgNWs (~1%), which shows stable heating capability. We note that the cyclic heating and cooling do not degrade the performance of the device, where the resistance-temperature curves barely change after 100 cycles of heating and cooling from 25°C to 42°C. The discrete ribbon-based kirigami design offers the unique features of adaptivity, conformability, and flexibility combined with a large contact area, which can be potentially applied to wearable sensors, flexible electronics, and textile electronics.

2.8 Methods

2.8.1 Simplification of the Gauss-Bonnet theorem

The Gauss-Bonnet theorem can be simplified according to the constant Euler characteristic and summation of the exterior angles. The Euler characteristic of the surface is a topological

invariant and keeps a constant during deformation. For the surface formed by two neighboring discrete ribbons, the Euler characteristic is given by

$$\chi(\Omega) = V - E + F = 1 \tag{2-9}$$

where *V*, *E*, and *F* denote the numbers of vertices, edges, and faces of the manifold *Ω*, respectively. In this process, *V*, *E*, and *F* do not change with the increasing strain, resulting in a constant Euler characteristic.

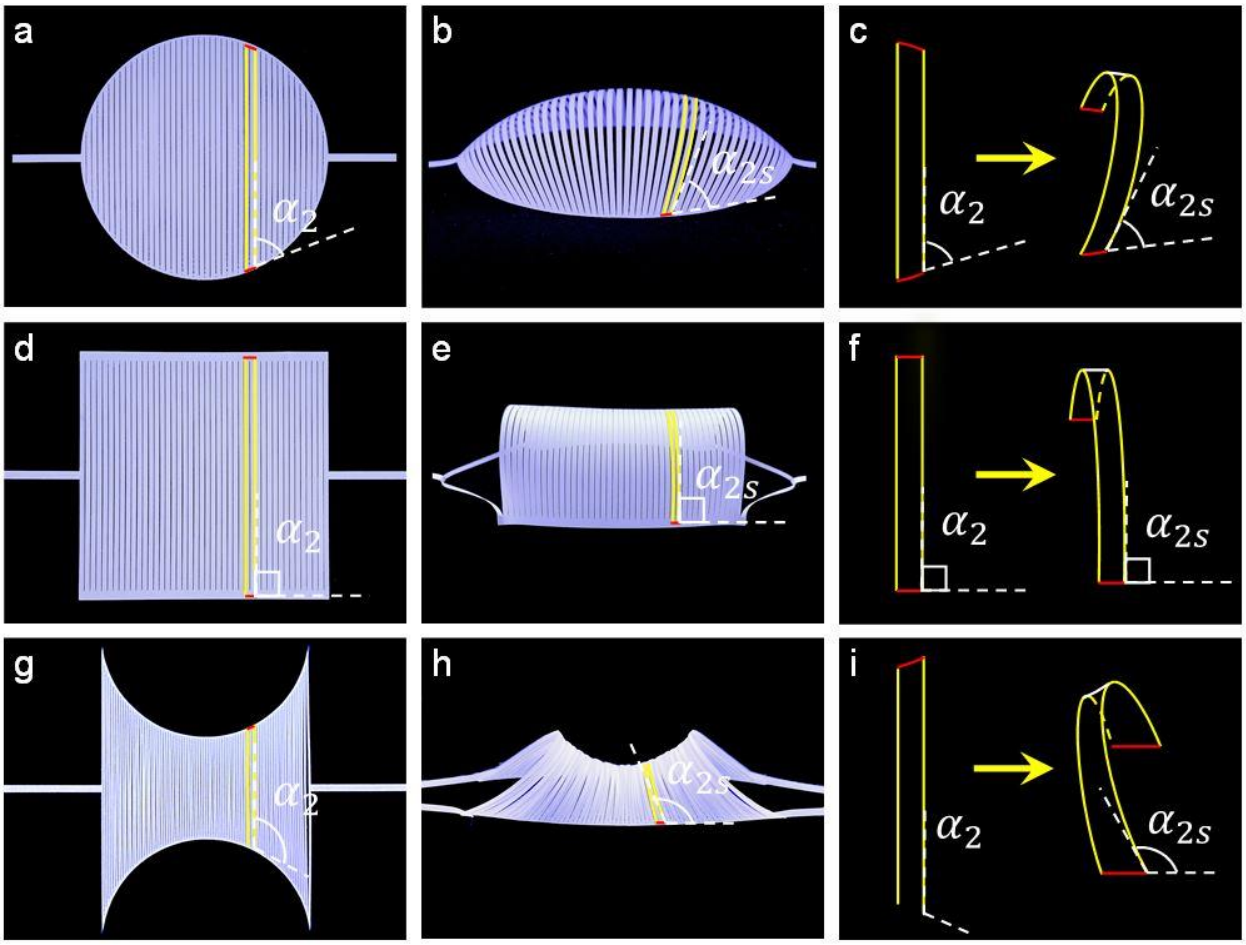

Fig. 2.7 Schematics of the surface formed by neighboring discrete ribbons. a-c Spheroidal shape. d-f Cylindrical shape. g-i Saddle shape. c, f, i show, schematically, the morphed shapes formed by neighboring discrete ribbons. Red and yellow lines are boundary and discrete ribbons, respectively. α_2 and α_{2s} are the angles between the tangent line of the boundary ribbon and the tangent line of the discrete ribbon before and after the deformation, respectively.

As shown in Fig. 2.7, the summation of the exterior angles does not change under tension and the variation in summation is expressed as

$$\Delta(\sum_{i=1}^{p}\theta_i) = 2\{\Delta[\alpha_{2s}(s_b + \frac{w_d}{\sin(\alpha_{2s})})] - \Delta[\alpha_{2s}(s_b)]\} = 0 \quad (2\text{-}10)$$

where $\Delta(\sum_{i=1}^{p}\theta_i)$ denotes the variation of the summation of the exterior angles; $\alpha_{2s}(s_b)$ denotes the angle between the tangent line of the boundary ribbon and the discrete ribbon at the point of intersection and is a function of the arc length of the boundary ribbon s_b; the coefficient 2 is from the symmetry of the structure; w_d is the width of the discrete ribbons. Note that we assume the distance Δs_b between two discrete ribbons along the boundary ribbon is expressed as $\Delta s_b = \frac{w_d}{\sin(\alpha_{2s})}$ because $w_d \ll R$, with R being the half-width of the 2D precursor.

For the cylindrical and spheroidal shape, it is obvious that $\Delta\alpha_{2s} = 0$ during the deformation due to the conformal mapping. For the saddle shape, while α_{2s} is changing due to the contact between the discrete ribbons, and the summation of the exterior angles keeps constant because the variation of the angles of two neighboring discrete ribbons has the same absolute value. It is noteworthy that the Gauss-Bonnet theorem is first applied to the surface formed by two neighboring discrete ribbons and then extended to the entire structure.

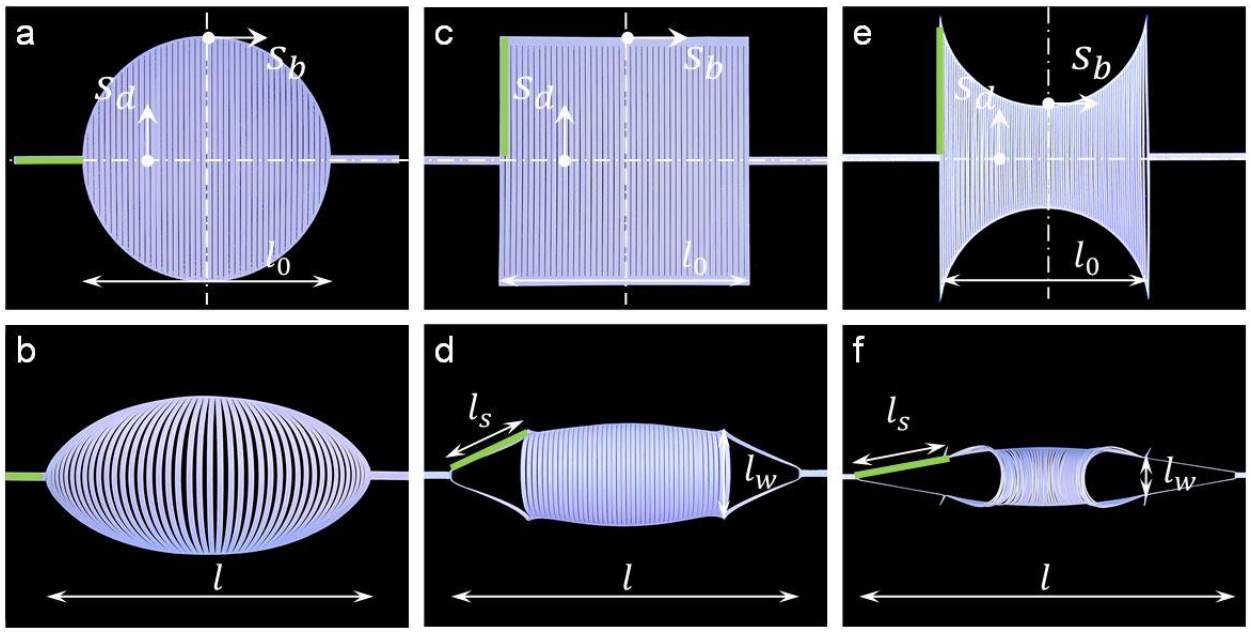

Fig. 2.8 Schematics of the coordinates (top-down view). a-b Spheroidal shape. c-d Cylindrical shape. e-f Saddle shape. a, c, e are 2D precursors and b, d, f are morphed shapes. s_b and s_d denote the arc length coordinate of the boundary and discrete ribbons, respectively. The boundary and discrete ribbons are parametrized by arc length and the origins are located at the midpoint of ribbons. l_0 and l are the length of the shapes before and during deformation, respectively; l_s and l_w are the lengths of the stretching ribbon and the width of the shape, respectively. Green lines represent the stretching ribbons.

The curve of the ribbon is parametrized by arc length; the origin is located at the midpoint of each ribbon (Fig. 2.8); s_b and s_d denote the arc length coordinate of the boundary and discrete ribbons, respectively. The integral of geodesic curvature along the smooth boundary of the manifold is composed of two parts, i.e., $\int k_g \, ds = \int k_{gd} ds_d + \int k_{gb} \, ds_b$, where k_{gd} and k_{gb} denote the geodesic curvature along the discrete and boundary ribbons, respectively. The geodesic curvature of the discrete ribbons is equal to zero ($k_{gd} = 0$), because the discrete ribbons are geodesics of the morphed surface (normal vectors of discrete ribbons are normal to the tangent plane). As such, the integral is simplified as

$$\int k_g \, ds = \int k_{gb} ds \tag{2-11}$$

where *ds* denotes the line element along the boundary of the manifold formed by two neighboring discrete ribbons. Further, the geodesic curvature of the boundary ribbons is equal to the projection of the curvature of the boundary ribbon on the tangent plane T_p of the surface. According to the Meusnier theorem[70], the relationship between the curvature of the boundary ribbon and the geodesic curvature is given by

$$k_{gb} =< \mathbf{r_b''}, \mathbf{S} >= k_b \sin\varphi \tag{2-12}$$

where k_b is the curvature along the boundary ribbon. k_{gb} is the geodesic curvature along the boundary ribbon. Vector $\mathbf{r_b}$ denotes the boundary curve parameterized by arc length and $|\mathbf{r_b''}|=k_b$, as shown by Fig. 2.9.

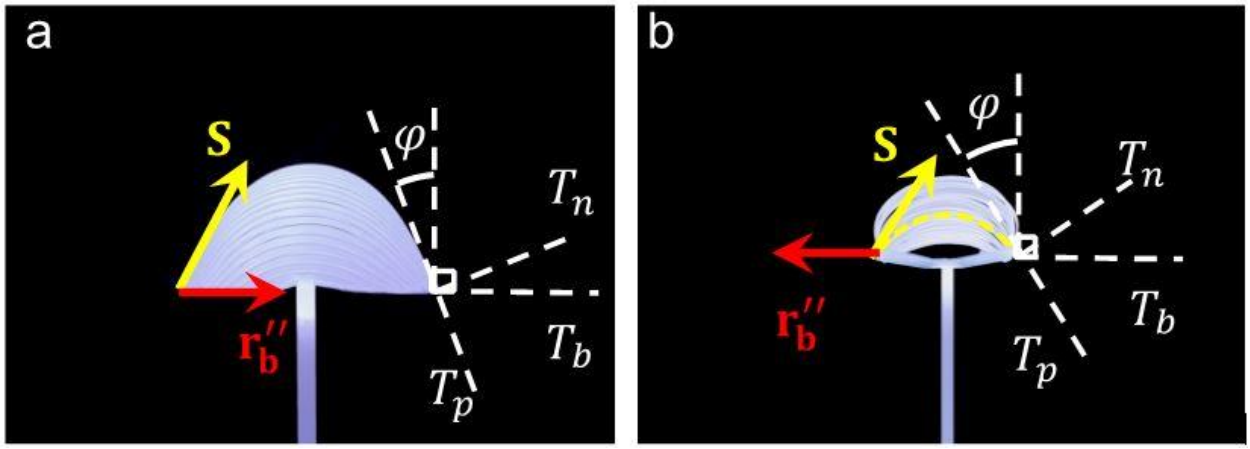

Fig. 2.9 Schematics of the projection of the boundary curvature. a Spheroidal shape. b Saddle shape. The yellow vectors S represent the preferred normal to the boundary ribbon α_b in the surface *S*. The red vectors $\mathrm{r_b''}$ are curvature vectors of the boundary ribbon. T_b is the plane containing the boundary curve; T_p is the tangent plane to the surface *S* at this point; T_n is the normal plane to the discrete ribbon at this point; φ denotes the angle between T_b and T_n.

2.8.2 Fabrication, mechanical testing and thermal treatment of the kirigami sheets

We used polyethylene terephthalate (PET) sheets (Dupont Teijin Film, McMaster–Carr) with Young's modulus of 3.5 GPa, Poisson's ratio of 0.38, and thickness of 0.127 mm for the kirigami sheets. The samples with different cut patterns were cut out using a laser cutter (EPILOG

LASER 40 Watts) with cut ribbon width of 1.5 mm and 0.75 mm. Uniaxial tensile tests were performed using Instron 5944 to characterize the force-displacement curves under a loading rate of 10 mm/min. Thermal treatment (120 °C for 120 min) of the deformed PET samples under a stretched state in an oven fixed the generated 3D shapes upon cooling to room temperature and force removal. To recover to the initial flat state, a second thermal treatment of the deployed 3D shapes was conducted under 120 °C for 120 min in the oven.

2.8.3 Finite element simulation

In the FEM simulation (Abaqus/Standard), the PET sheets corresponding to three different morphologies as a spheroid, cylinder, and saddle were modeled as linear elastic, isotropic material with the measured Young's modulus of 3.5 GPa and Poisson's ratio of 0.38. The geometries were meshed with solid quadratic tetrahedral elements (C3D10H) and the fine mesh was applied to the connection area for the ribbons. The left end was fixed and a prescribed displacement was applied to the right end to stretch the 2D kirigami precursors.

2.8.4 Fabrication of the AgNW/PDMS heater

For the nanowire synthesis, a modified polyol process was used. Firstly, 60 mL of a 0.147 M PVP (MW ~ 40000, Sigma-Aldrich) solution in EG (was added to a round-bottom flask to which a stir bar was added; the vial was then suspended in an oil bath (temperature 151.5 °C) and heated for 1 h under magnetic stirring (150 rpm). Then at 1h, 200 µL of a 24 M CuCl2 (CuCl2·2H2O, 99.999+%, Sigma-Aldrich) solution in EG was injected into the PVP solution. The solution was then heated for an additional 15 min, followed by injecting 60 mL of a 0.094 M AgNO3 (99+%, Sigma-Aldrich) solution in EG. AgNWs in ethanol solution with an average

diameter of 90 nm and length of 20–30 μm were shaken for 5 minutes before use to disperse the nanowires in the solution. The AgNW solution was drop-casted on plasma-treated polyimide (PI) tape on a glass slide; at the same time, the solution was heated by a hot plate at 50 °C to evaporate the solvent. After the evaporation of ethanol, the AgNWs were thermally annealed at 150 °C for 20 min. Then the sample was laser cut to the desired pattern with extra nanowires and PI removed. Then liquid PDMS (SYLGARD 184) with a weight ratio of 10 : 1 was spin-coated onto the AgNW film, degassed, and subsequently thermally cured at 100 °C for 1 hour. After curing, the AgNW/ PDMS composite was laser cut again to the designed geodesic pattern. Then the AgNW/PDMS composite was peeled off from glass/PI substrate in water. Finally, Cu wires were attached to the two ends of the heater by silver epoxy (MG Chemicals) for connection to the power source.

2.8.5 Deformation of the discrete ribbons

The torsional energy of the boundary ribbon is small compared with the bending energy of discrete ribbons due to the small width of the boundary ribbon. Therefore, the torsion of the boundary ribbon is dominated by discrete ribbons. As such, the shape of the slender discrete ribbons can be derived based on large deflections of buckled ribbons and is expressed as

$$\bar{y}_d = \frac{2}{\lambda} E(AM(\lambda \overline{s}_d, m), m) - \overline{s}_d \tag{2-13}$$

$$\bar{z}_d = \frac{2m}{\lambda} CN(\lambda \overline{s}_d, m) \tag{2-14}$$

where $\bar{y}_d$ and $\bar{z}_d$ are normalized coordinate functions; $\overline{s}_d$ denotes the normalized arc length coordinate of the discrete ribbons; the discrete ribbon is parametrized by its arc length and these variables are normalized with the half-width of the precursor, *R*; the origins are located at the midpoint of ribbons; *E*, *AM*, and *CN* are elliptic functions; $m(\overline{s}_b, \varepsilon)$ is the modulus characterizing the deformation of the discrete ribbons. The angle φ (Fig. 2.9) between the plane T_b containing the

boundary ribbon and the normal plane T_n of the discrete ribbon at this point is dependent on m and is expressed as

$$\varphi = \tan^{-1}\left(-\frac{2\sqrt{m^2-m^4}}{1-2m^2}\right) + \frac{\pi}{2} \quad (2\text{-}15)$$

2.8.6 Effect of the boundary curve smoothness in combinatorial designs

The smoothness of the backbone in the morphed shape depends on the smoothness of the boundary in the 2D precursor. C^0 continuity represents curves without continuous first derivative; C^1 continuity represents the curve and the first derivative are continuous (i.e., continuous in tangent vector); C^2 continuity represents the curve, the first derivative, and the second derivative are continuous (i.e., continuous in curvature). For instance, the eyes and mouth in the form of holes (Fig. 2.4) are formed and controlled by its C^0continuous boundaries, arising from the variation of the exterior angles at the joints based on the Gauss-Bonnet theorem. Note that for C^0 continuous boundaries, the decrease of the exterior angles results in a hole, while the increase of the exterior angles leads to the contact of discrete ribbons. The C^2 and C^1 continuous boundary segments generate the sections with C^2 and C^1 continuity in the backbone, respectively, as shown in the waterdrop and vase shape (Fig. 2.4).

2.8.7 Actuated ribbon bistability by remote magnetic field

We note that each ribbon in the buckled shapes of the three kirigami sheets with different boundary curvatures is bistable, i.e., it can pop up or pop down energetically equivalent (Fig. 2.10). By manually flipping the popping directions in the three buckled spheroidal, cylindrical, and saddle shapes under the stretched state, it can transform to more different shapes.

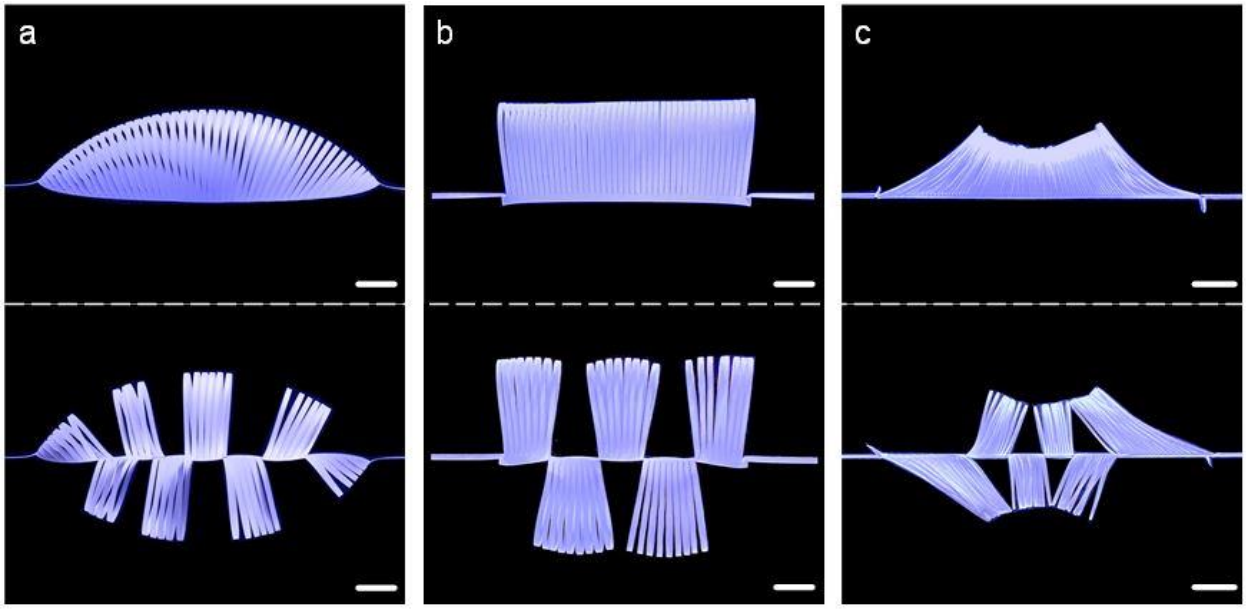

Fig. 2.10 Experiments of bistable states in three characteristic structures. a Spheroidal shape. b Cylindrical shape. c Saddle shape. (Top) All discrete ribbons pop up. (Bottom) Some discrete ribbons pop up, with the others popping down. The applied strain is 0.35, 0.9, and 1.52, respectively. Scale bars = 10 mm.

In addition to the contact-based mechanical actuation for shape morphing, we also demonstrate the capability of achieving bistability in kirigami sheets through remote magnetic actuation, as shown in Fig. 2.11. By attaching magnetic thin polymeric stripes to the discrete ribbons, we could use a remote translational magnetic field to fast switch the bistable states in the ribbons to reconfigure the kirigami structure. There exists a sequential snapping of the discrete ribbons in the spheroidal structure, where its sequence could be tuned via the distribution of the

magnetic polymers in the 2D kirigami precursor. We harness the distribution of the polymers changing the direction and the magnitude of the magnetic forces and torques acting on the discrete ribbons to tune the snapping sequence of the discrete ribbons. It is obvious that with the increasing strength of the magnetic field, ribbon one snaps first and then the ribbon two because the magnetic forces acting on them are larger. The ribbon three snaps last because the magnetic forces acting on it are smaller.

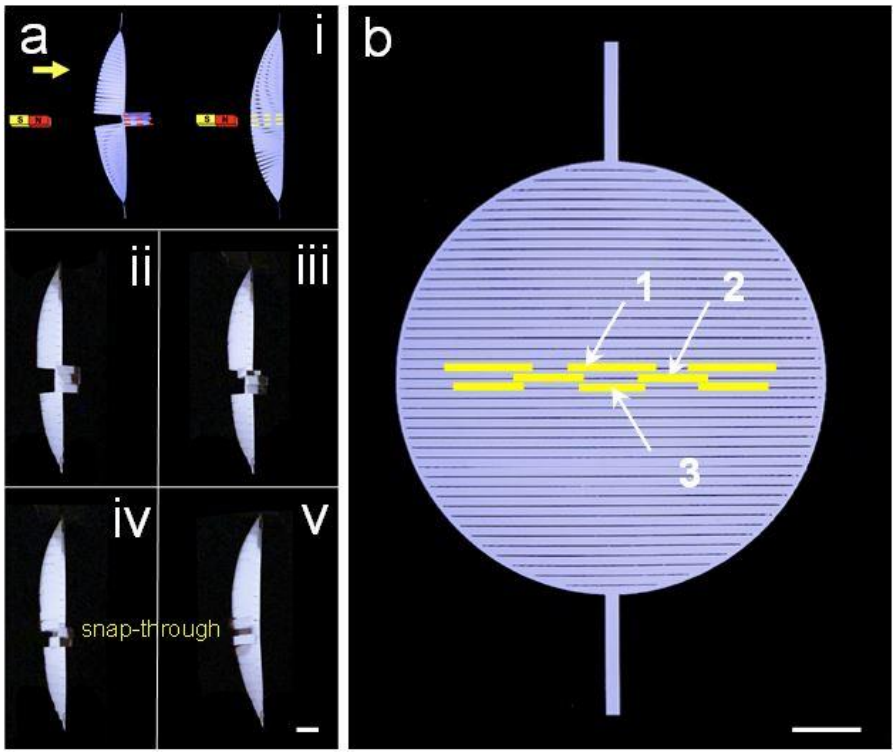

Fig. 2.11 a. ii-iv A moving magnetic field triggers the sequential snapping of the bistable central ribbons with magnetic polymers. b Schematic of the distribution of the magnetic polymers attached to three discrete ribbons 1, 2, and 3. Yellow lines represent the magnetic polymers. Scale bars = 10 mm. The magnetic polymer glued to the discrete ribbons is conformable magnets for irregular surfaces (McMaster–Carr) with thickness t = 0.794 mm.

2.8.8 Extending the strategy to other cut patterns

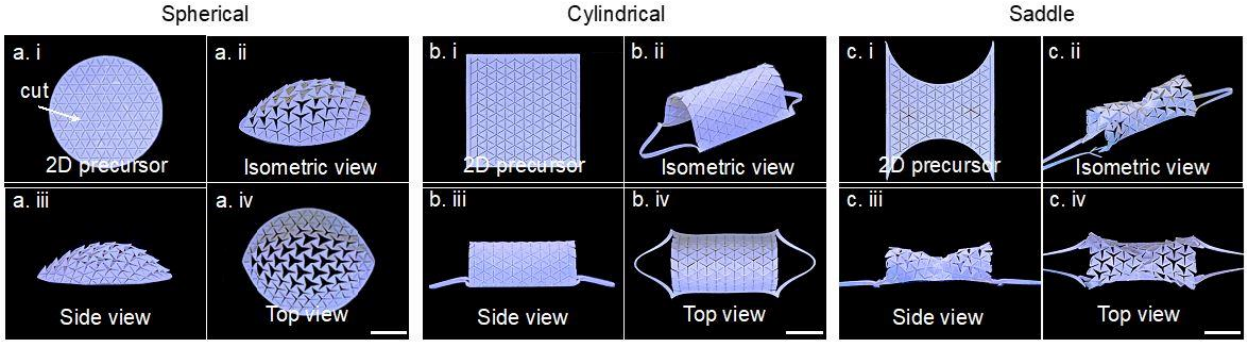

Fig. 2.12 Application of our method to kirigami sheets with hexagonal patterns. a, b, and c are the spheroidal, cylindrical, and saddle shape formed by 2D precursors with positive, zero, and negative boundary curvature, respectively. Scale bars = 10 mm.

As shown in the Fig. 2.12, the 2D precursors composed of periodic hexagonal cuts are enclosed by a circular, rectangular, and a biconcave boundary, respectively. Stretching the precursors leads to spheroidal, cylindrical, and saddle shapes, respectively. First, the decreasing boundary curvature as shown in the top view causes nonuniform expansions (rotations around the hinges relative to the neighboring units) of different unit cells leading to the formation of a spheroidal shape with positive Gaussian curvature. Second, the straight boundary compresses the surface to induce the global out-of-plane buckling resulting in a cylinder. Third, the flattened boundary curve leads to a saddle shape, where the local out-of-plane buckling of the unit cells at the center of the morphed shape is attributed to the geometric frustration. It is noteworthy that the local out-of-plane buckling disturbs the smoothness during the expansion of the hexagonal cuts. Also, the length of the hinge of the unit cells in the saddle shape needs to be small to reduce the bending rigidity and facilitate both the in-plane expansion and the out-of-plane buckling. These proof-of-concept results show that applying our approach to other patterns requires an additional program due to the coupling between geometric frustration and elasticity.

2.9 Conclusion and discussion

This chapter demonstrated a new way of utilizing the cut boundary curvature to guide the formation of controllable and reconfigurable complex 3D curved shapes in kirigami sheets patterned with simple parallel cuts. Such a strategy is validated through combined theoretical modeling, FEM simulations, and experiments. The unique feature of discrete cut ribbons as geodesic curves of the deformed 3D shapes largely simplifies the inverse design. Programming the dynamic 3D morphology, we showed a universal noninvasive flexible kirigami gripper for grasping and preserving delicate organisms and a biomimetic kirigami heater with decent conformability and intrinsic adaptivity to human knees.

The parallel cuts ensure easy fabrication. However, there are some limitations on our proposed method in terms of the achievable morphed shapes and the level of curvature programmability[83]. It is challenging for the straight discrete ribbons to approximate an axisymmetric shape perfectly due to the limitation of their elastica shape (e.g., a cone shape). The inverse design with a high-accuracy requirement will need local optimization of the boundary curve. For targeted more complex 3D surface shapes with arbitrary negative and positive curvatures, the inverse design will become more challenging since it needs to utilize the smoothness of two orthogonal geodesics to design both the tessellation of different shaped unit cells and the shapes of inner and outer boundary curves. Moreover, compared to the intrinsic deployment of retained 3D shapes through bistability[83] or pre-strain release[16] after force removal, our approach requires the application of external stretching forces to remain the deployed shapes, otherwise, the generated 3D shape will return to its original flat form after the external actuation is removed due to the fully reversible elastic deformation in the thermoplastic kirigami structure. To preserve the deformed 3D shapes, we could utilize the shape memory properties of the PET

polymer upon heating above its glass transition temperature[84]. We use thermal treatment under 120 ^{o}C to treat the 3D shapes held at an applied stretching strain for a period of 120 min and cooled down to the room temperature to fix the deformed configuration. Notably, the preserved 3D configuration can be further deformed and recover to its 2D flat precursor shape upon another thermal treatment.

Despite the demonstration of programmable shaft shifting in the thermoplastic kirigami sheets, we envision that the proposed strategy is material and scale independent. We note that despite the large applied stretching strain ε, the maximum principal strain ε_{max} in the buckled ribbons with thickness of 127 μm remains small (ε_{max} < 1% for ε > 50%), e.g., ε_{max} = 0.4% in the deformed spherical shape at ε = 30% (Fig. 2.2) and ε_{max} = 0.6% in the saddle shape at ε = 147%. Note that at the tip of the cuts, the stress concentration could be reduced via curved cuts, and moderate plastic deformation could be tolerated, as demonstrated by the over 1,400 repeated cycles of 400g deadweight lifting with the gripper without failure. Considering the small peak tensile strain in the buckled ribbons and its linear relationship with sheet thickness t, i.e., ε_{max} decreases linearly with t, we envision that the proposed kirigami strategy could also be applied to design shape-morphing and stretchable structures and devices made of other functional materials such as metals and even semiconductors at small scales, as well as other stimuli-responsive materials actuated by temperature, electrical, and magnetic field, etc.

Besides the parallel ribbon pattern, we also apply the boundary-curvature guided strategy to other homogeneous cut patterns, such as the triangular cut pattern. As a consequence of the different deformation mechanisms and the disturbed smoothness of the formed surface, our strategy is limited and the detailed deformation mechanism and shape morphing will be explored

in the future. This work could find potential applications in designing soft robots, non-invasive soft grippers, stretchable electronics, wearable devices, and portable and wearable heaters.

CHAPTER 3

Programmable wavy shapes in geometrically coupled ribbons under uni-axial stretching

Note: This Chapter was partially adapted and modified from the manuscript below: Hong, Y. et al. Programmable wavy shapes in geometrically coupled ribbons, in preparation (2023).

3.1 Introduction

Inspired by nastic morphologies in nature[58, 59], shape-morphing materials have attracted broad interests in past decades. The concept of shape morphing lies at the heart of numerous applications in the field of soft robotics[60], biomedical surgery[61], minimally invasive marine life conservation[47], and swift architectures[62]. The yielded morphological intelligence, facilitated through programmed deformations, instigates evolutions in crucial functions such as grasping[17], locomotion[21], sensing, and decision-making[63]. These functions are typically executed using pneumatic/hydraulic actuators or stimuli-responsive materials, such as magnetic polymers[60], dielectric elastomers, and liquid crystal elastomers[63], which rely on intricate material or chemical interventions. However, there is a scarcity of studies exploring the utilization of simple mechanical approaches to mimic the nastic morphologies observed in nature. Such approaches hold significant potential for applications in the domains of soft robotics and marine life conservation. For instance, the undulating waves commonly observed in leaves, flower petals, and Manta rays. In this study, we present a straightforward methodology for creating and programming wavy shapes formed by interconnected ribbons.

3.2 Wavy ring upon uniaxial stretching

We start by stretching a circular 2D precursor (Fig. 3.1) made of PET (polyethylene terephthalate) with the Young's modulus E = 3.5 GPa and the thickness t = 0.127 mm. The precursor is patterned with parallel cuts. These cuts divide the precursor into discrete strips enclosed by a thin curved boundary with a width w and radius R. Manipulating the boundary curvature $1/R$ can generate smooth 3D shapes with different Gaussian curvatures[1]. For example, for the precursor with a thin boundary (w = 0.5 mm in Fig. 3.1), upon stretching, the boundary gradually transits from circular to elliptical. As shown in Fig. 3.1, the bending boundary makes all discrete strips buckle and form a smooth spherical shape. The smooth shape results from the twisting of the boundary governed by the buckling of the discrete strips. Differently, with the width w increasing to 1.5 mm (Fig. 3.1), the stretched structure exhibits a wavy shape with an undulating boundary, as shown by Fig. 3.1. The wavy shape results from the bending and twisting of the boundary coupled with the buckling of discrete strips.

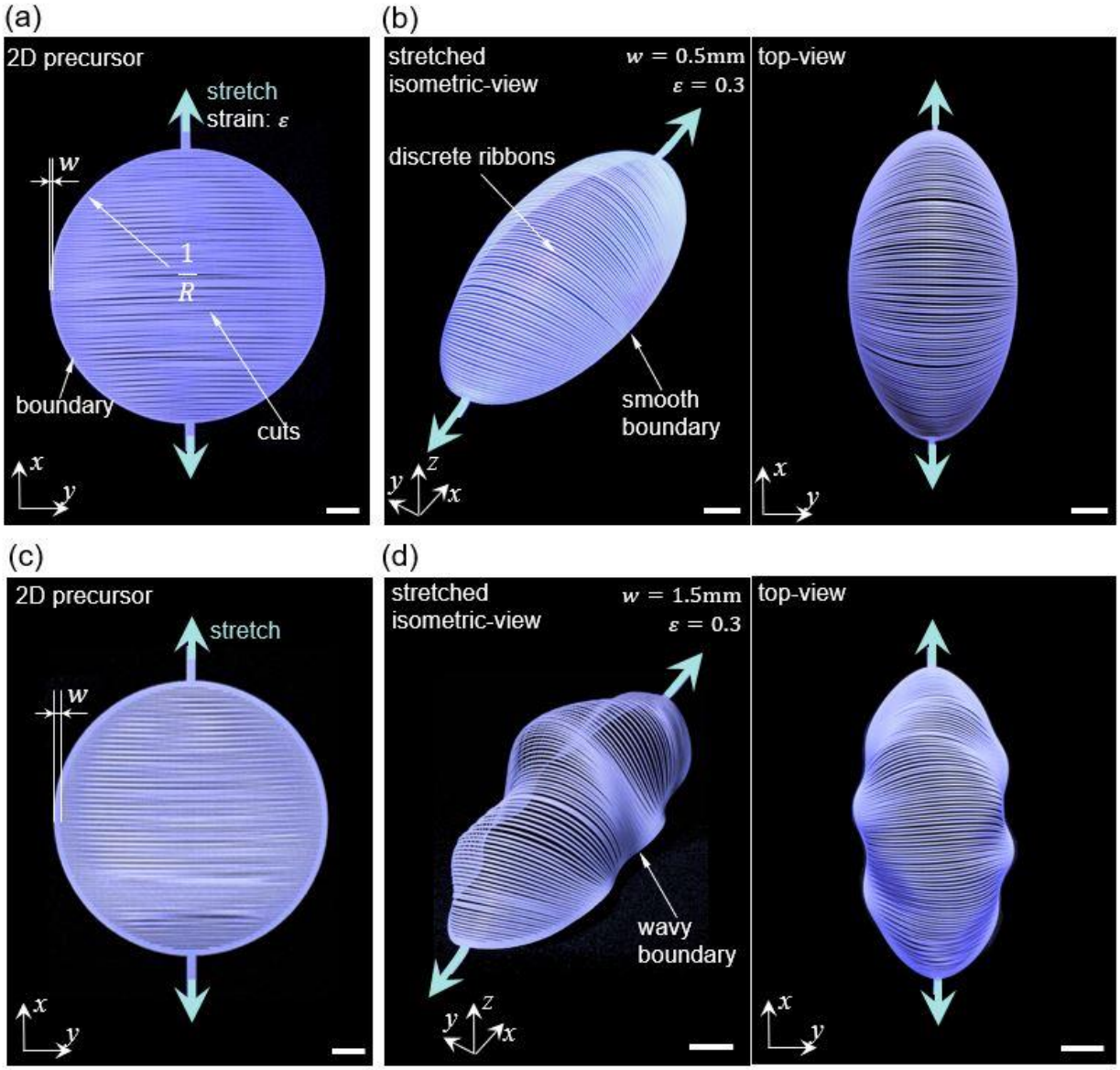

Fig. 3.1 Two distinct morphologies under uni-axial stretching via tuning width *w*. a, c 2D precursors patterned with parallel cuts enclosed by a circular boundary with width *w* = 0.5 and 1.5 mm. *R* denotes the radius of the circular boundary. c, d Isometric and top view of the smooth and wavy structures formed by the stretched 2D precursor. Green arrows represent the strecthing direction. Scale bars = 10 mm.

3.3 Buckling of discrete strips

3.3.1 Ribbon parameterization

To elucidate the origin of the wavy shape, we rationalize the deformation of the discrete and boundary ribbon during stretching. To study the deformation of the ribbon, we define each ribbon by its centerline (i.e., space curve) with *s* denoting the arclength coordinate. The space curve is obtained by integrating the unit tangent vector expressed as

$$\hat{\boldsymbol{t}} = \frac{\partial \tilde{\boldsymbol{r}}}{\partial s}, \tag{3-1}$$

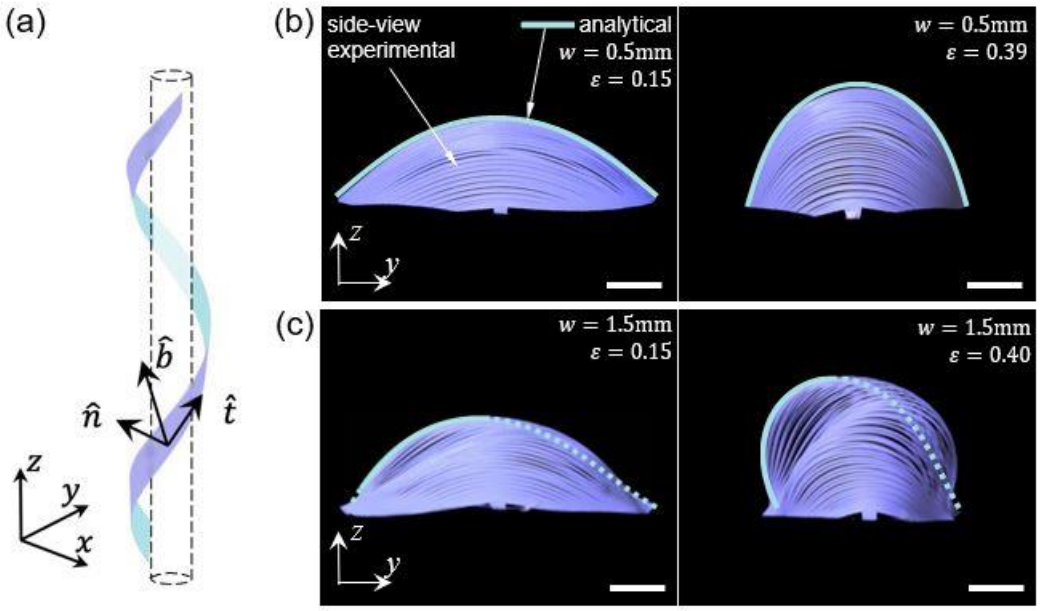

Fig. 3.2 Buckling of the discrete strip. a Schematics of the ribbon with a Frenet-Serret triad. $\hat{\boldsymbol{t}}$, $\hat{\boldsymbol{n}}$, and $\hat{\boldsymbol{b}}$ are unit tangent, normal, and binormal vectors, respectively. b, c Side view of the stretching structures with the profile showing the buckling discrete strip. Green curves are the analytical results. Scale bars = 10 mm.

We construct the Frenet-Serret triad along the arc length *s*, as shown in Fig. 3.2. The orthogonal triad evolves along the arc length based on the Frenet-Serret equations:

$$\frac{\partial \hat{\boldsymbol{t}}}{\partial s} = \kappa \hat{\boldsymbol{n}}, \tag{3-2}$$

$$\frac{\partial \hat{\boldsymbol{n}}}{\partial s} = \tau \hat{\boldsymbol{b}} - \kappa \hat{\boldsymbol{t}}, \tag{3-3}$$

$$\frac{\partial \hat{\boldsymbol{b}}}{\partial s} = -\tau \hat{\boldsymbol{n}}, \tag{3-4}$$

where κ and τ denote the curvature and torsion of the space curve, respectively. $\hat{\boldsymbol{t}}$, $\hat{\boldsymbol{n}}$, and $\hat{\boldsymbol{b}}$ are unit tangent, normal, and binormal vectors, respectively. Given the curvature and torsion of the curve along *s*, this frame can be obtained as a unique solution based on the Frenet-Serret equations through integrating the unit tangent vector $\hat{\boldsymbol{t}}$.

Assuming the ribbon to be inextensible and unshearable, the ribbon is parameterized by a position vector $\tilde{\boldsymbol{r}}(s)$ in the local orthonormal frame $(\hat{\boldsymbol{d}}_1, \hat{\boldsymbol{d}}_2, \hat{\boldsymbol{d}}_3)$, with $\hat{\boldsymbol{d}}_1$ and $\hat{\boldsymbol{d}}_2$ denoting the direction of a material cross section along the ribbon. Defining $\hat{\boldsymbol{d}}_3 = \hat{\boldsymbol{d}}_1 \times \hat{\boldsymbol{d}}_2$, we derive the kinematic equations expressed as

$$\hat{\boldsymbol{d}}_3 = \frac{\partial \tilde{\boldsymbol{r}}}{\partial s}, \tag{3-5}$$

$$\frac{\partial \hat{\boldsymbol{d}}_i}{\partial s} = \tilde{\boldsymbol{\omega}} \times \hat{\boldsymbol{d}}_i, \tag{3-6}$$

where $\tilde{\boldsymbol{\omega}} = \kappa_1 \hat{\boldsymbol{d}}_1 + \kappa_2 \hat{\boldsymbol{d}}_2 + \kappa_3 \hat{\boldsymbol{d}}_3$ is the Darboux vector. κ_1 and κ_2 are curvatures in the width and thickness direction, respectively, with $\kappa = \sqrt{{\kappa_1}^2 + {\kappa_2}^2}$. κ_3 denotes the twisting of the ribbon.

3.3.2 Shape function of deformed discrete strips

As the strain ε increases, the bending of the boundary leads to the buckling of the discrete strips (Fig. 3.1 and Fig. 3.2). Based on the Kirchhoff rod equations, we derive the balance of force and moment

$$\frac{\partial \tilde{\boldsymbol{N}}}{\partial s} + \boldsymbol{f} = 0, \tag{3-7}$$

$$\frac{\partial \tilde{\boldsymbol{M}}}{\partial s} + \frac{\partial \tilde{\boldsymbol{r}}}{\partial s} \times \tilde{\boldsymbol{N}} + \boldsymbol{l} = 0, \tag{3-8}$$

where $\widetilde{\boldsymbol{N}}$ and $\widetilde{\boldsymbol{M}}$ denote the resultant force and moment exerted on the cross section by the stress at $\tilde{\boldsymbol{r}}(s)$. $\boldsymbol{f}$ and $\boldsymbol{l}$ are the body force and moment per unit length, respectively.

When the width *w* of the boundary is small, the deploying structure is dominated by the buckling of discrete strips (Fig. 3.1 and Fig. 3.2). It makes the strips symmetric about the *z*-axis and resemble the shape of Euler elastica. This planar shape function based on Equations (3-7) and (3-8) can be simplified as

$$y_d = \frac{2}{\lambda} E(AM(\lambda s_d, m), m) - s_d, \tag{3-9}$$

$$z_d = \frac{2m}{\lambda} CN(\lambda s_d, m), \tag{3-10}$$

where y_d and z_d are the Cartesian coordinates. The discrete strips use the normalized arc length coordinate s_d, where the origin is set at the central point. *E*, *F*, *AM*, and *CN* are elliptic functions, with *m* being the elliptic modulus. λ is the parameter to normalize the length of the strip

$$\lambda = 2F(\frac{\pi}{2}, m)/s_d \tag{3-11}$$

When the width *w* of the boundary becomes larger, the deploying structure depends on the coupling effect of the buckling discrete strips and the bending boundary. As show in Fig. 3.2, the coupling effect results in the asymmetric buckling of discrete strips. The simplified governing equations of the planar shape function derived from Equations (3-7) and (3-8) read

$$\frac{dN_y}{ds} = 0, \tag{3-12}$$

$$\frac{dN_z}{ds} = 0, \tag{3-13}$$

$$\frac{dM}{ds} = N_y \sin\theta - N_z \cos\theta, \tag{3-14}$$

where N_y and N_z denote the planar resultant forces. *M* is the moment about the *x*-axis exerted on the cross section by the stress at *s*. θ denotes the tangent direction along the arc length *s*. Next, we apply the Bernoulli-Euler law and the geometric relationships expressed as

$$\kappa = \frac{d\theta}{ds} = \frac{M}{EI}, \tag{3-15}$$

$$\frac{dy_d}{ds} = \cos\theta, \tag{3-16}$$

$$\frac{dz_d}{ds} = \sin\theta, \tag{3-17}$$

where κ is the curvature. E and I are the Young's modulus and second moment of area. y_d and z_d are the Cartesian coordinates.

To validate the analytical results, we plot the analytical curves (green) in the side view of the deployed structures, which are consistent with the experimental results. As shown in Fig. 3.2, considering the rotation of the plane containing the discrete strip, we define a tilting angle between the *xy*-plane and the plane containing the discrete strip. Due to the conformal deformation at the connection of the discrete strip and the boundary, the tilting angle reads

$$\varsigma(s_b, m) = \cos^{-1}\{\tan(\varphi)\left[\frac{1}{2\tan(\theta)} - \frac{\tan(\theta)}{2} - \frac{1}{\sin(2\theta)} + \frac{\cos(\zeta_b)}{\sin(\varphi)\cos(\theta)}\right]\}, \tag{3-18}$$

where ζ_b is the angle between the tangent line of the boundary and the tangent line of the discrete strip. θ denotes the angle between the tangent line of the boundary ribbon and the x axis. φ is the angle between the discrete strip and *z*-axis given by

$$\varphi = \tan^{-1}(-\frac{2\sqrt{m^2-m^4}}{1-2m^2}) + \frac{\pi}{2} \tag{3-19}$$

3.4 Deformation of boundary ribbon

3.4.1 Two distinct buckling modes

To understand the deformation of the circular boundary ribbon, we start by uni-axially stretching the circular ring with a width *w*, a thickness *t*, and a radius *R* (Fig. 3.3). The circular ribbons with different widths exhibit two different buckling modes, as shown in Fig. 3.3. For the ribbon with a small width (w = 0.35 mm), the circular ribbon initially starts to bend (in the width

direction $\hat{\boldsymbol{d}}_1$) in plane upon the uniaxial stretching (with the applied strain ε = 0.05). Then, as ε increased, it buckle (in the thickness direction $\hat{\boldsymbol{d}}_2$) out-of-plane, as shown in Fig. 3.3. This results from the smaller bending rigidity of the thickness direction $\hat{\boldsymbol{d}}_2$ compared to that of the width direction $\hat{\boldsymbol{d}}_1$. When the strain ε increases to 0.2, the buckling becomes more prominent, and it exhibits a banana-like isometric view and a smooth C-shaped side view (Fig. 3.3).

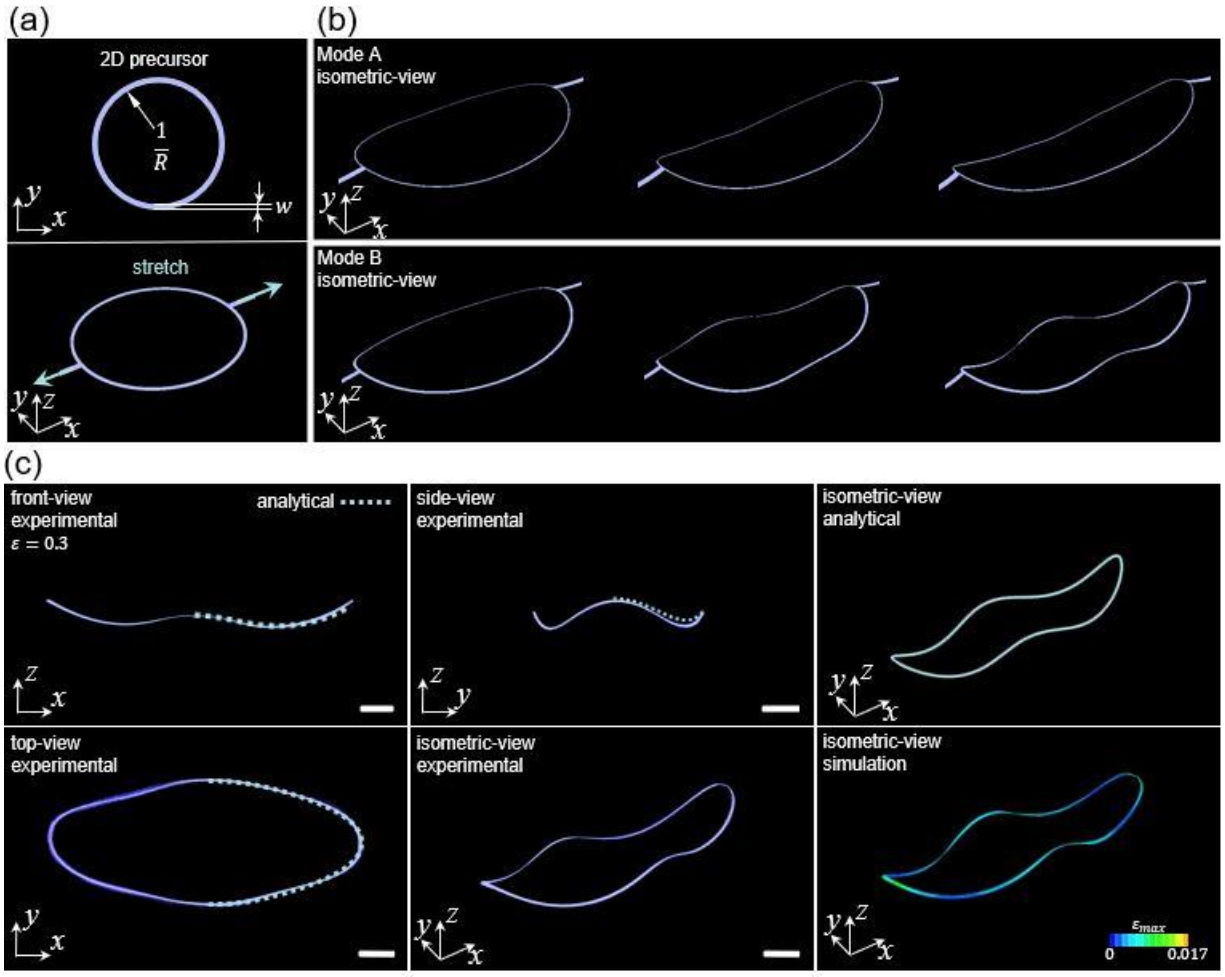

Fig. 3.3 Buckling of the boundary ribbon. a Schematics of the circular boundary ribbon. b Isometric view of the stretching ribbon in two distinct modes. c front-, side-, top-, and isometric-view of experimental results of the stretched ribbon in Mode 2. Green curves are the analytical results. The color bar is the maximum principal strain. Scale bars = 10 mm.

For the ribbon with a larger width (w = 0.6 mm), the circular ribbon exhibits a different buckling deformation upon uni-axial stretching (Fig. 3.3). Initially, the ring shows a similar stretching-induced deformation to that of the sample with a smaller width. It bends in plane (ε = 0.05) followed by an out-of-plane buckling (ε = 0.1). Interestingly, as the strain ε increases to 0.2, the deformed ribbon exhibits a wavy shape with a W-shaped side view (Fig. .3). It utilizes the inexpensive buckling in the thickness direction $\widehat{\boldsymbol{d}}_2$ and torsion to minimize the expensive bending in the width direction $\widehat{\boldsymbol{d}}_1$, as discussed later.

3.4.2 Analytical modelling

We derive the governing equations for the deformed boundary ribbons based on Equations (3-7) and (3-8). With the body force p and moment l per unit length being zero, the six equilibrium equations are expressed as

$$\frac{dN_1}{d\bar{s}} = N_2\bar{\tau} - T\bar{\kappa}_2, \tag{3-20}$$

$$\frac{dN_2}{d\bar{s}} = T\bar{\kappa}_1 - N_1\bar{\tau}, \tag{3-21}$$

$$\frac{dT}{d\bar{s}} = N_1\bar{\kappa}_2 - N_2\bar{\kappa}_1, \tag{3-22}$$

$$EI_1\left(\frac{d\bar{\kappa}_1}{d\bar{s}} - \frac{d\bar{\kappa}_{1o}}{d\bar{s}}\right) - EI_2(\bar{\kappa}_2 - \bar{\kappa}_{2o})\bar{\tau} + GJ(\bar{\tau} - \bar{\tau}_o)\bar{\kappa}_2 - N_2 = 0, \tag{3-23}$$

$$EI_2\left(\frac{d\bar{\kappa}_2}{d\bar{s}} - \frac{d\bar{\kappa}_{2o}}{d\bar{s}}\right) + EI_1(\bar{\kappa}_1 - \bar{\kappa}_{1o})\bar{\tau} - GJ(\bar{\tau} - \bar{\tau}_o)\bar{\kappa}_1 + N_1 = 0, \tag{3-24}$$

$$GJ\left(\frac{d\bar{\tau}}{d\bar{s}} - \frac{d\bar{\tau}_o}{d\bar{s}}\right) - EI_1(\bar{\kappa}_1 - \bar{\kappa}_{1o})\bar{\kappa}_2 + EI_2(\bar{\kappa}_2 - \bar{\kappa}_{2o})\bar{\kappa}_1 = 0, \tag{3-25}$$

where $\bar{\kappa}_1$, $\bar{\kappa}_2$, and $\bar{\tau}$ are the curvature and torsion of the deformed state in the direction of $\widehat{\boldsymbol{d}}_1$, $\widehat{\boldsymbol{d}}_2$, and $\widehat{\boldsymbol{d}}_3$, respectively. $\bar{\kappa}_{1o}$, $\bar{\kappa}_{2o}$, and $\bar{\tau}_o$ are the curvature and torsion of the reference state in the direction of $\widehat{\boldsymbol{d}}_1$, $\widehat{\boldsymbol{d}}_2$, and $\widehat{\boldsymbol{d}}_3$ respectively. N_1, N_2, and T are resultant forces along the direction of

$\widehat{\boldsymbol{d}}_1$, $\widehat{\boldsymbol{d}}_2$, and $\widehat{\boldsymbol{d}}_3$, respectively. EI_1, EI_2, and GJ denote the bending and torsional rigidity, respectively.

Considering the only non-zero curvature $\bar{\kappa}_{1o}$ in the reference state, Eq. (3-24) - (3-25) can be simplified. Substituting with

$$\alpha = \frac{EI_1}{GJ}, \tag{3-26}$$

$$\beta = \frac{EI_2}{GJ}, \tag{2-27}$$

we get

$$\alpha \frac{d\bar{\kappa}_1}{d\bar{s}} = \beta\bar{\kappa}_2\bar{\tau} - \bar{\kappa}_2\bar{\tau} + \bar{N}_2, \tag{3-28}$$

$$\beta \frac{d\bar{\kappa}_2}{d\bar{s}} = \alpha(\bar{\kappa}_1 - \bar{\kappa}_{1o})\bar{\tau} - \bar{\kappa}_1\bar{\tau} - \bar{N}_1, \tag{3-29}$$

$$\frac{d\bar{\tau}}{d\bar{s}} = \alpha(\bar{\kappa}_1 - \bar{\kappa}_{1o})\bar{\kappa}_2 - \beta\bar{\kappa}_1\bar{\kappa}_2, \tag{3-30}$$

where $\bar{N}_1$, $\bar{N}_2$, and T are resultant forces along the direction of $\widehat{\boldsymbol{d}}_1$, $\widehat{\boldsymbol{d}}_2$, and $\widehat{\boldsymbol{d}}_3$, respectively.

The Cartesian coordinates along the ribbon can be expressed as the quaternions in the form of

$$\frac{d\bar{x}}{d\bar{s}} = 2(q_1q_3 + q_0q_2), \tag{3-31}$$

$$\frac{d\bar{y}}{d\bar{s}} = 2(q_2q_3 - q_0q_1), \tag{3-32}$$

$$\frac{d\bar{z}}{d\bar{s}} = 2(q_0^2 + q_3^2 - 0.5), \tag{3-33}$$

where $\bar{x}$, $\bar{y}$, and $\bar{z}$ are normalized Cartesian coordinates along the ribbon arc length coordinate. $\boldsymbol{q} = [q_0, q_1, q_2, q_3]$ is the unit quaternion with $q_0^2 + q_1^2 + q_2^2 + q_3^2 = 1$. The direction of the cross-section along the ribbon can be expressed as

$$\frac{dq_0}{d\bar{s}} = 0.5(-q_1\bar{\kappa}_1 - q_2\bar{\kappa}_2 - q_3\bar{\tau} + \upsilon q_0), \tag{3-34}$$

$$\frac{dq_1}{d\bar{s}} = 0.5(q_0\bar{\kappa}_1 - q_3\bar{\kappa}_2 + q_0\bar{\tau} + \upsilon q_1), \tag{3-35}$$

$$\frac{dq_2}{d\bar{s}} = 0.5(q_3\bar{\kappa}_1 + q_0\bar{\kappa}_2 - q_1\bar{\tau} + \upsilon q_2), \tag{3-36}$$

$$\frac{dq_3}{d\bar{s}} = 0.5(-q_2\bar{\kappa}_1 + q_1\bar{\kappa}_2 + q_0\bar{\tau} + \upsilon q_3), \tag{3-37}$$

where υ is a parameter to ensure $q_0^2 + q_1^2 + q_2^2 + q_3^2 = 1$. The components of the unit quaternion can be expressed by Euler angles, which reads

$$q_0 = \cos\frac{\theta}{2}\cos\frac{\phi+\varphi}{2} \tag{3-38}$$

$$q_1 = \sin\frac{\theta}{2}\sin\frac{\phi-\varphi}{2} \tag{3-39}$$

$$q_2 = \sin\frac{\theta}{2}\cos\frac{\phi-\varphi}{2} \tag{3-40}$$

$$q_2 = \cos\frac{\theta}{2}\sin\frac{\phi+\varphi}{2} \tag{3-41}$$

Equations (3-20)-(3-22), (3-28)-(3-30), and (3-31)-(3-37) give a system of thirteen first-order differential equations with thirteen unknowns, yielding a boundary value problem. Solving this provides us with the deformation of the ribbon, shown by Fig. 4.3, which is consistent with the experimental results.

3.4.3 C-to-w criterion

Fig. 4.4 shows the variation in the curvature and torsion along the arclength of the boundary ribbon upon stretching. In Mode 1 (Fig. 3.2) with a smaller width *w*, the ribbon exhibits smooth curvature and torsion, as the applied strain increases from 0.1 to 0.2. As shown in Fig. 3.4, with the strain increasing, the C-shaped curvature becomes more prominent, where the torsion decreases near linearly with the arc length *s*. It leads to a C-shaped side-view (Fig. 3.2). Distinctly,

for Mode 2 (Fig. 3.2), when the strain $\varepsilon = 0.1$, both the curvature and torsion are smooth, similar to that of Mode A. With the strain ε increasing to 0.2, it starts to exhibit a w-shaped curvature and an undulating torsion (Fig. 3.4 b) to minimize the elastic energy. It results in the wavy shape of the ribbon. It utilizes inexpensive bending in the thickness direction $\hat{\boldsymbol{d}}_2$ and torsion, due to the larger bending rigidity in the width direction $\hat{\boldsymbol{d}}_1$. Fig. 3.4c shows the energy difference between the Mode 1 and Mode 2 as a function of the ratio of width *w* and thickness *t*. For a smaller ratio (w/t<4.7), the elastic energy stored in the Mode 1 is smaller than that in Mode 2. The ribbon exhibits a smooth C-shape. In contrast, with a larger ratio (w/t>4.7), the elastic energy stored in the Mode 1 is larger than that in Mode 2. The ribbon naturally exhibits a w-shape.

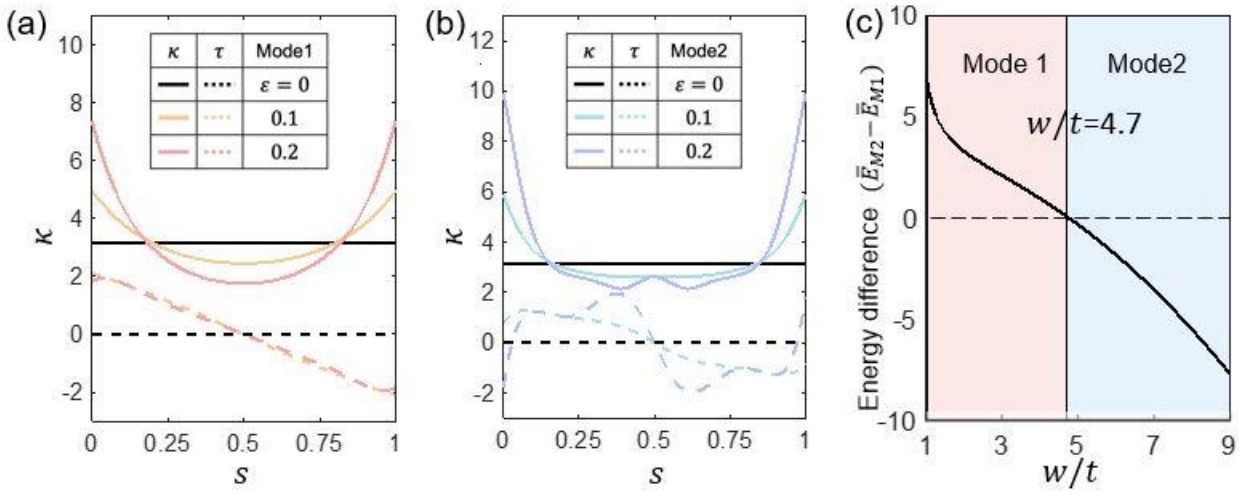

Fig. 3.4 Curvature and torsion of two distinct buckling modes. a-b Analytical results showing the curvature and torsion along the arclength coordinate *s* of the ribbon. κ and τ are the curvature and torsion, respectively. c The difference between the elastic energy stored in the boundary ribbon of two modes at the strain ε = 0.2.

3.4.4 Generic and scalable w-shaped boundary

As shown in Fig. 3.5, the w-shaped boundary is generic and not sensitive to the variation in the width or radius of the circular boundary ribbon. Fig. 3.5 a shows that with *w* the width of

the boundary increasing from 3mm to 7mm, the ribbons under uni-axial stretching exhibit a similar w-shaped side-view. Additionally, with the radius *R* of the boundary increasing from 16.5mm to 66mm, the ribbons under uni-axial stretching exhibit similar w-shaped, as shown by the isometric-view in Fig. 3.5b. These arise from that to avoid the expensive bending in the width direction $\hat{\boldsymbol{d}}_1$, the ribbon uses the inexpensive bending in the thickness direction $\hat{\boldsymbol{d}}_2$ and torsion, which results in a w-shape.

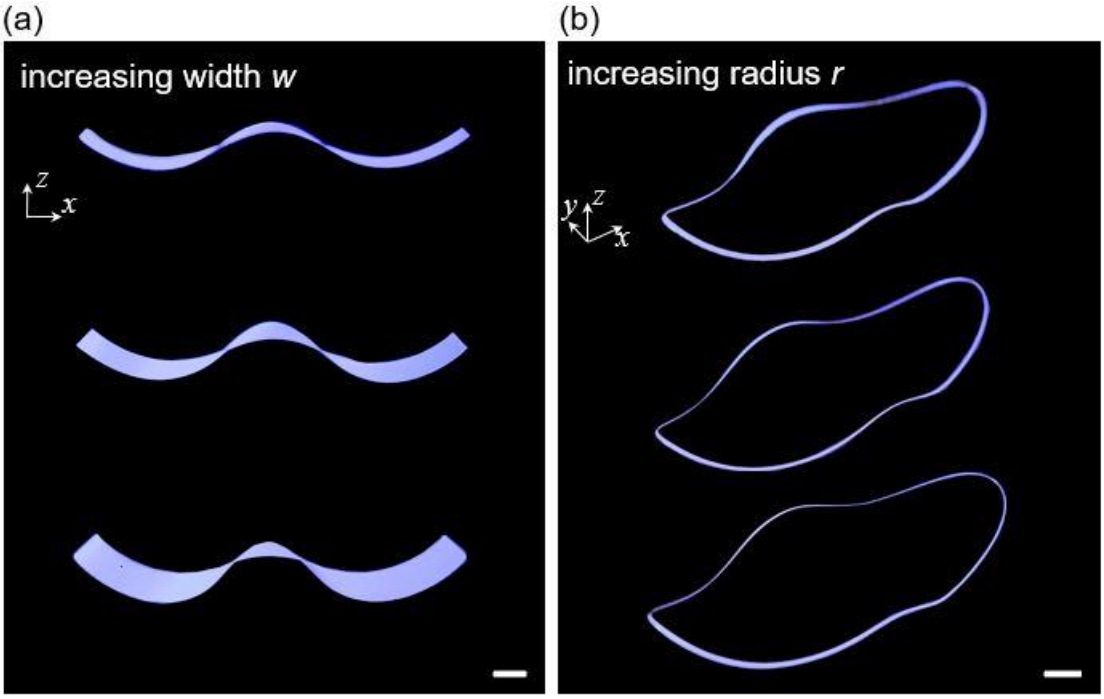

Fig. 3.5 Generic and scalable w shape. a Experimental side-view of the stretched boundary ribbons with the width *w* ranging from 3mm to 7mm. b Experimental isometric-view of the stretched boundary ribbons with the radius *R* ranging from 16.5mm to 66mm. Scale bars = 10 mm.

3.5 Coupled morphology of the boundary and discrete strips

We further program the wavy shape by the interplay of the boundary ribbon and discrete strips subject to uni-axial stretching. Fig. 3.6 shows the top-view and front-view of three samples with different widths (w = 0.5, 1.5, and 4.5 mm) at the same strain ε = 0.34. For the boundary with a smaller width (as shown by the example with w = 0.5 mm in Fig. 3.6 a), the morphology is

dominated by the buckling of the discrete strips. The structure exhibits a smooth spherical shape upon stretching. For the boundary with a larger width w = 1.5 mm, the interplay of the boundary ribbon and discrete strips leads to a most prominent wavy shape, as shown in Fig. 3.6 b. For the boundary with a larger width (as shown by the example with w = 4.5 mm in Fig. 3.6 c), the morphology is dominated by the boundary ribbon. The wavy boundary still shows a w-shape, similar to that in Fig. 3.2. The buckling of discrete ribbons only rotates the bending plane of the boundary from vertical to horizontal. The coupling effect barely changes the wavy shape of the boundary due to the increased rigidity from the increased width. The analytical results (green curves) are consistent with the experimental results, considering the effect from the discrete strips as body force and moment exerted on the boundary. Fig. 3.6 d shows the force-displacement curve of the structure under uni-axial stretching. The curves for samples with a larger width initially exhibit a sharp increase before the buckling of the boundary (d=1.25 mm). All subsequently increase linearly with the displacement d, where a larger width results in a larger force but a similar stiffness. After d>17.5 mm, all samples transit from the bending-dominated morphology to the stretching-dominated morphology, where a larger width leads to a sharp increase in stiffness.

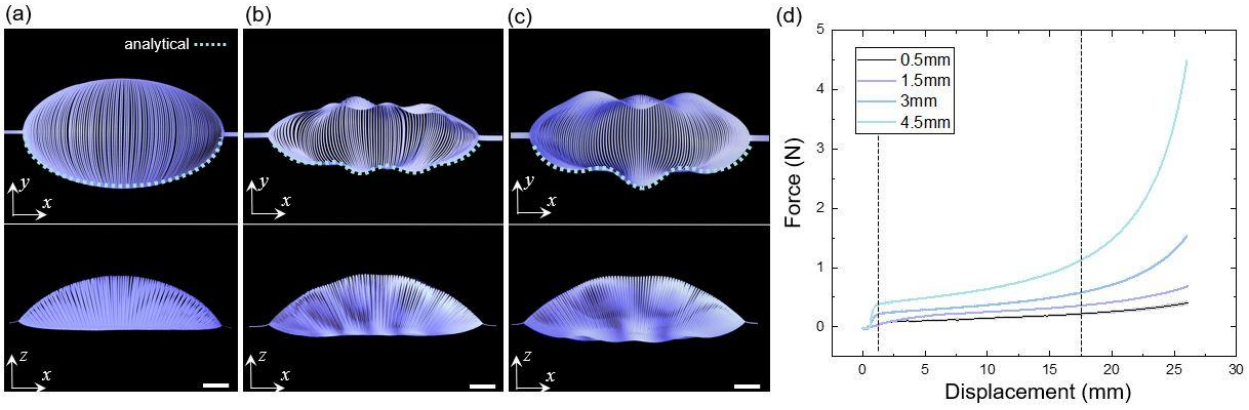

Fig. 3.6 Three different coupled morphologies. A-c Experimental top- and front-view of the stretched structures with the width w = 0.5, 1.5, and 4.5 mm. Green curves are the analytical results. d Force-displacement curves for structures with different widths. Scale bars = 10 mm.

Fig. 3.7 shows the wave number *N* in the boundary as a function of the ratio *w*/*t*. *N* defines the times of the curvature of the boundary ribbon changes its sign. With a smaller ratio *w*/*t*, *N* remains 0. The morphology is dominated by the buckling in discrete strips. With the ratio *w*/*t* increasing, *N* jumps to the maximum, due to the interplay of the boundary ribbon and discrete strips. With the ratio *w*/*t* further increasing, the effect from the discrete strips is weakened. It results in a wave number same as that of the w-shaped boundary in Fig. 3.3.

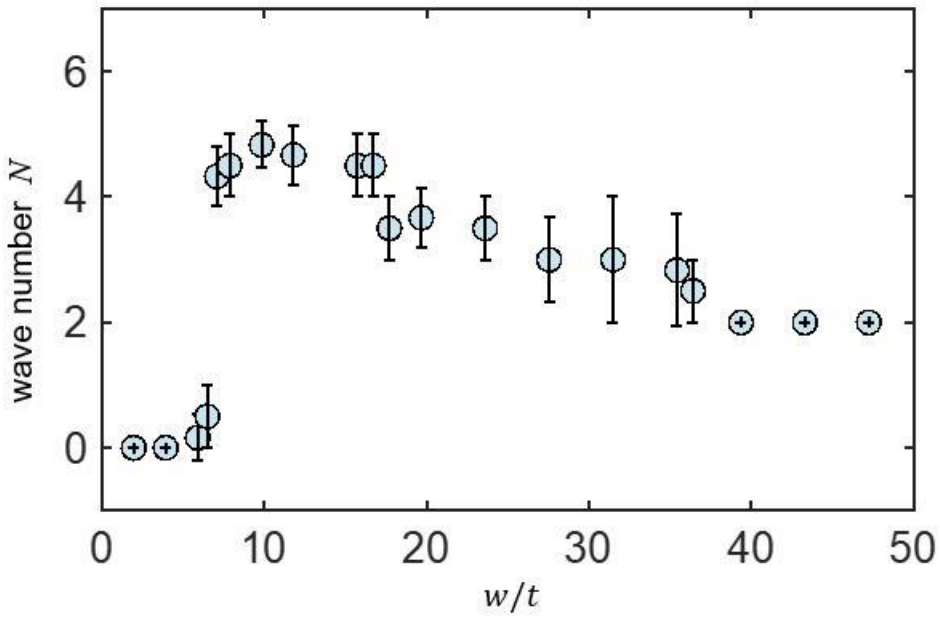

Fig. 3.7 The wave number *N* in the boundary as a function of the ratio *w*/*t*. *N* defines the times of the curvature of the boundary ribbon changes its sign.

3.6 Conclusions and discussions

This chapter demonstrates that tuning the geometric parameters in boundary ribbons in interconnected kirigami structures leads nastic wavy shapes. We provide an analytical methodology to predict and program the stretching-induced morphologies of interconnected ribbons. This approach harnesses mechanical shape evolutions as means to naturally induce undulating shapes, eliminating the need for material or chemical interventions. The outcomes

exhibit potential for diverse applications in biological systems and soft robotics. Moreover, the application of these structures to active materials leads to the generation of undulating shapes that exhibit wave propagations, a phenomenon commonly observed in various natural organisms. We leave it for future work.

CHAPTER 4

Curvature-guided noninvasive gripper evolves into an angle-programmed gripper with ultradelicacy, ultrastrength, and ultraprecision through tendril-like trajectories

Note: This Chapter was partially adapted and modified from the publications below: Hong, Y. et al. Boundary curvature guided programmable shape-morphing kirigami sheets. *Nature Communications* **13**, 530 (2022). Hong, Y. et al. Angle-programmed tendril-like trajectories enable a multifunctional gripper with ultradelicacy, ultrastrength, and ultraprecision. *Nature Communications*, in press (2023).

4.1 Introduction

It often perplexes researchers as to how they can translate the morphological properties into practical applications. In this chapter, we first demonstrate how harnessing the morphological intelligence of kirigami sheets generates a noninvasive gripper for gelatinous organisms. Additionally, we unlock the full potential of morphological intelligence in soft manipulation by employing a mechanics-guided design approach to create an angle-programmed gripper with exceptional delicacy, strength, and precision, achieved through tendril-like trajectories. These programmed nastic trajectories, inspired by nature, give rise to extraordinary grasping capabilities that are well-suited for diverse extreme scenarios. This innovation holds immense promise for a wide range of applications, including agriculture, food processing, prosthesis development, minimally invasive marine life conservation, and advancements in biomedicine.

4.2 Noninvasive gripper

A simple, rapid, and economical soft gripper is highly required in biomedical robotics and wildlife-conservation devices. However, for the existing soft grippers realized by pneumatic[37,38,40], hydraulic[86], and magnetic actuation[87] and responsive materials[17] using pinching[37,38,87], enclosing[86], and suction[44], it is challenging to balance the response time, manufacturing cost, simplicity of designs, and robustness in noninvasive grasping missions. Here, utilizing the programmable shape morphing, we present a noninvasive kirigami hand, which can encapsulate gelatinous and delicate organisms nondestructively in unstructured environments.

Subject to simply uniaxial stretch, the 2D kirigami precursor composed of two circular units bridged with a biconcave unit (Fig. 4.1) transforms into an encapsulated Venus-flytrap-like shape composed of two hemispheres bridged with a saddle shape (Fig. 4.1**)**. To demonstrate its delicacy in noninvasively grasping gelatinous organisms, we use the example of grasping a raw egg yolk from a petri dish with the grasping process and mechanism from open to closed states shown in Fig. 4.1 in both side view and front view (insets). First, the biconcave unit starts bending and forms a V shape with the increasing uniaxial stretch. Next, as shown in Fig. 4.1, the two circular units transform into two hemispheres with the variation of the boundary curvature and start grasping the egg yolk from the bottom. Last, the flattened boundary curve leads to the closure of the structure and encapsulating the egg yolk, where the super-slippery and soft yolk can be held for hours showing both the soft yet robust ability to encapsulate and preserve gelatinous organisms. Further, to demonstrate the advantage of the bio-interactive hand, we rapidly encapsulate a live fish from water before it could escape; we then release it unharmed. The noninvasive interaction shows the conformability and adaptivity of the gripper. Also, encapsulating super-soft objects (e.g., shampoo bubbles) and the collection of granular objects (e.g., pine nuts) from a super-soft substrate

(e.g., a raw egg yolk) are demonstrated, broadening its versatility and noninvasiveness. Moreover, the universal gripper can be applied to a wide range of targets, including small objects such as a human hair, a coin, a thin micro-SD card, and blueberries, etc., as well as a 400g deadweight that is 1,000 times the weight of the gripper (0.4g). We note that despite the simple design, the gripper kirigami is capable of repeatedly lifting the 400g deadweight for over 1,400 cycles without causing materials and structural failure and sacrificing its grasping performance, demonstrating the robustness of the gripper.

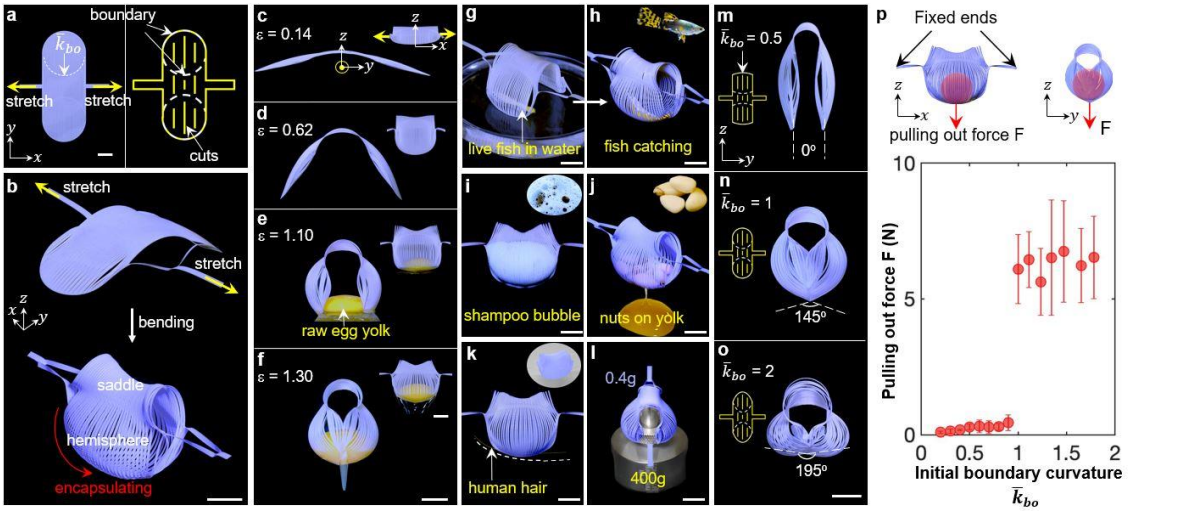

Fig. 4.1 Programmable delicate and noninvasive kirigami gripper. a 2D precursor composed of an array of two circular units bridged with a biconcave unit. $\bar{k}_{bo}$ defines the initial boundary curvature of the units. Yellow arrows are the direction of the uniaxial stretching. Yellow lines and white dashed lines represent the cuts and the boundaries, respectively. b Isometric view of the morphology from bending to encapsulating upon stretching. Red arrows represent the morphing direction of the hemisphere. c-f Side views of the grasping process of a raw quail egg yolk with the increasing applied strain from 0.14 to 1.3, respectively. The inset shows the corresponding front views. g-h Encapsulating a live fish from a petri dish filled with water. i Grasping the super-soft shampoo bubbles from the surface of the water. j Collecting the granular objects (pine nuts) from the super-soft surface of a raw egg yolk. k-l Grasping a human hair (k) and a deadweight (400 g, l). m-o Experimental illustration of shapes formed by 2D precursors with the different initial-boundary curvatures $\bar{k}_{bo}$ at the maximum applied strain. The insets show the schematic figure of the 2D precursors. The white dashed line represents the angle between the tips of the gripper. p Pulling-out force test via pulling out a red sphere from the grippers with various boundary curvatures $\bar{k}_{bo}$. The error bars represent the standard errors of the mean. Schematics and the experimental results. Red arrows are the direction of the pulling-out force. Scale bars = 10 mm.

The morphology programmed via tuning the boundary curvature can be further harnessed to tailor the holding force of the flexible gripper [86]. As shown in Fig. 4.1, when the normalized initial-boundary curvature $\bar{k}_{bo}$ of the 2D precursors increases from 0 to 2, after simple stretching, the angle formed by the two tips of the hemispheres increases from 0 to 195^{o}, correspondingly, their final deformed shapes transit from open ($\bar{k}_{bo} < 1$) to closed ($\bar{k}_{bo} \geq 1$). The precursor with $\bar{k}_{bo} = 1$ defines a critical state, where the two curved ends can become contacted to form a 3D encapsulated shape. Correspondingly, as shown in Fig. 4.1 on the pulling force of the kirigami grippers vs. $\bar{k}_{bo}$, it results in a sudden jump of the pulling-out force of the kirigami grippers at $\bar{k}_{bo} = 1$ from an average force of 0.4N ($\bar{k}_{bo} < 1$) to 6.1 N ($\bar{k}_{bo} \geq 1$), a 15 times grasping force enhancement. The pulling force is defined as the minimum force required to pull the red sphere out of the gripper, as schematically illustrated on the top of Fig. 4.1. The force jump is because the grasping mode transits from pinching by friction to distinct encapsulating due to the programmed shape of the grippers by the boundary curvature. Further increasing the normalized boundary curvature beyond 2 does not lead to a higher pulling force, since all the grippers share a similar closed shape under the same encapsulating grasping mode, where further deformation is constrained by the contacted hemisphere petals. Furthermore, for the kirigami grippers with the same size and geometry, when reducing the number of parallel cuts or equivalently increasing the ribbon width, we observe the similar sudden jumping of the dramatically reduced pulling force at a critical ribbon width 0.875 mm, arising from the same grasping transition mode from encapsulating to pinching.

It is noteworthy that using pinching or the friction force, existing kirigami grippers are not well suited for grasping gelatinous organisms[17,87]. These grippers need to compress or pinch the targets to lift the targets, making the noninvasive collection of the delicate organisms

challenging[17,87]. Distinct from that, we demonstrated a different grasping mode, encapsulating the targets ultra-gently without compressing the objects, via programmable morphology, which is especially suitable for grasping delicate organisms nondestructively. Also, the pulling-out force of our gripper could be an order of magnitude (about 10 times) larger than recently reported kirigami grippers[87] at the same scale by harnessing the dynamically programmed morphology.

4.3 Gripper evolution for extreme scenarios

Given the tradeoff between delicacy, strength, and precision, it remains a grand challenge to simultaneously achieve high delicacy (extremely small contact pressure for noninvasive grasping), high strength (high pull force for large payload-to-weight ratios), and high precision (handling both small-size objects and thin sheets on flat surfaces without additional attachments) in a single soft gripper[58,65]. One potential solution is the aforementioned adaptive shape-morphing kirigami approach[45,46]. Inspired by the kirigami approach[45], the previous section in boundary curvature-guided design of an encapsulating kirigami gripper takes a step toward a potential delicate, strong, and precision gripper[46]. We demonstrated its proof-of-concept applications in manually picking up gelatinous organisms nondestructively 100-μm-diameter without the need of additional attachments[46]. It underscores the significance of adaptive morphologies in potentially mitigating the tradeoff challenges. However, despite these advancements, its performance still falls short of achieving the ultimate goal of an extraordinary high-performance soft gripper that specializes across the diverse range of high-requirement tasks mentioned above. Several challenges persist in the field, necessitating further exploration. These include effectively handling objects that are even more delicate than the reported water-filled balloon[54] and raw egg yolk[46], such as water droplets. Additionally, addressing the manipulation of micro-size and thin objects

thinner than a human hair that requires ultraprecision, and accommodating ultra-heavy objects that may surpass the reported record-high payload-to-weight ratio of 6400[52], as well as the potential integration of the gripper with prosthetic hands for multifunction, pose significant hurdles.

Another potential solution is to mimic natural organisms, which balance this tradeoff by morphing with nastic trajectories to perform grasping and climbing, e.g., cucumber tendrils and cephalopod tentacles[66]. Soft grippers aim to imitate their shapes, but few explore the potential of the nastic trajectory for exceptional grasping capabilities[67]. Previous studies in soft grippers primarily emphasize the adaptive morphologies for specialized or universal grasping improved capabilities[58,65]. Their grasping trajectories receive less attention and remain largely unexplored[68]. However, the significance of the trajectory should not be overlooked, as it profoundly influences the gripper's performance of soft grippers, especially when dealing with noninvasive manipulation of fragile objects and precision grasping of small or thin objects[58]. The explicit modeling and programming of trajectories pose considerable challenges due to the inherent complexities arising from the nonlinear and large deformations observed in soft materials and compliant structures[69]. For example, the implicit relationship between the boundary curvature and trajectory of the curvature-based kirigami gripper in the section[46] makes it rather challenging to program and control the grasping trajectories.

In this section, we propose combining the two potential solutions of adaptive morphologies in kirigami and nastic curves in tendril plants to potentially address the challenges. Here, we report a new angle-based kirigami gripper by manipulating the intersecting angle γ in the X-shaped ribbon (Fig. 4.2) for specializing across versatile high-requirement tasks. It shows unprecedented capabilities compared to the current state-of-the-art kirigami grippers and other soft grippers based on different actuation mechanisms[58,65]. First, it enables programmable tendril-like trajectories and

adaptive morphologies by γ_0 in an explicit and controlled manner theoretically and experimentally. Second, it can simultaneously achieve ultragentle yet ultrastrong and ultra-precision manipulations, which facilitate its unprecedented universality. We show that it is capable of noninvasively grasping extremely soft objects, e.g., a water droplet with nearly zero stiffness (Fig. 4.2), precisely grasping an ultra-thin polymer sheet as thin as 4 μm and 2 μm-diameter microfiber that are 20 times and 40 times thinner than a typical human hair, respectively, and strongly grasping an ultra-heavy dead weight with 16,000 times the self-weight of the gripper (0.4 g) that is 16 times the load capacity in our curvature-based design[46] and 2.5 times the reported record-high payload-to-weight ratio[52]. Third, we demonstrate, for the first time, a proof-of-concept, environment-friendly gripper made of natural and biodegradable materials such as bare leaf (Fig. 4.2) in ultragentle grasping of a dandelion (Fig. 4.2) and other objects. This green design philosophy aims to minimize both the impact on targets, such as plants and animals, and the associated ecological footprint[88]. Fourth, the lightweight, deployable, and simple displacement-controlled gripper facilitates its easy integration with prosthetic hands without the need of additional tethered bulky power and actuation systems in fluidic driven grippers[37,39,41,42]. Utilizing the explicit displacement-trajectory relationship that facilitates the grasping control, we demonstrate its integration with robotic prosthetics and multifunctionality in handling various challenging delicate tasks, such as noninvasively picking a grape from the vine (Fig. 4.2), opening a zipper, turning a book page, and folding clothes etc. A feedback system required for delicate tasks in existing prostheses[89] is not necessary with the help of the tendril-like trajectory. These demonstrated unprecedented capabilities also highlight both the novelty and significance of this work.

4.4 Programmable trajectories through manipulating γ_0

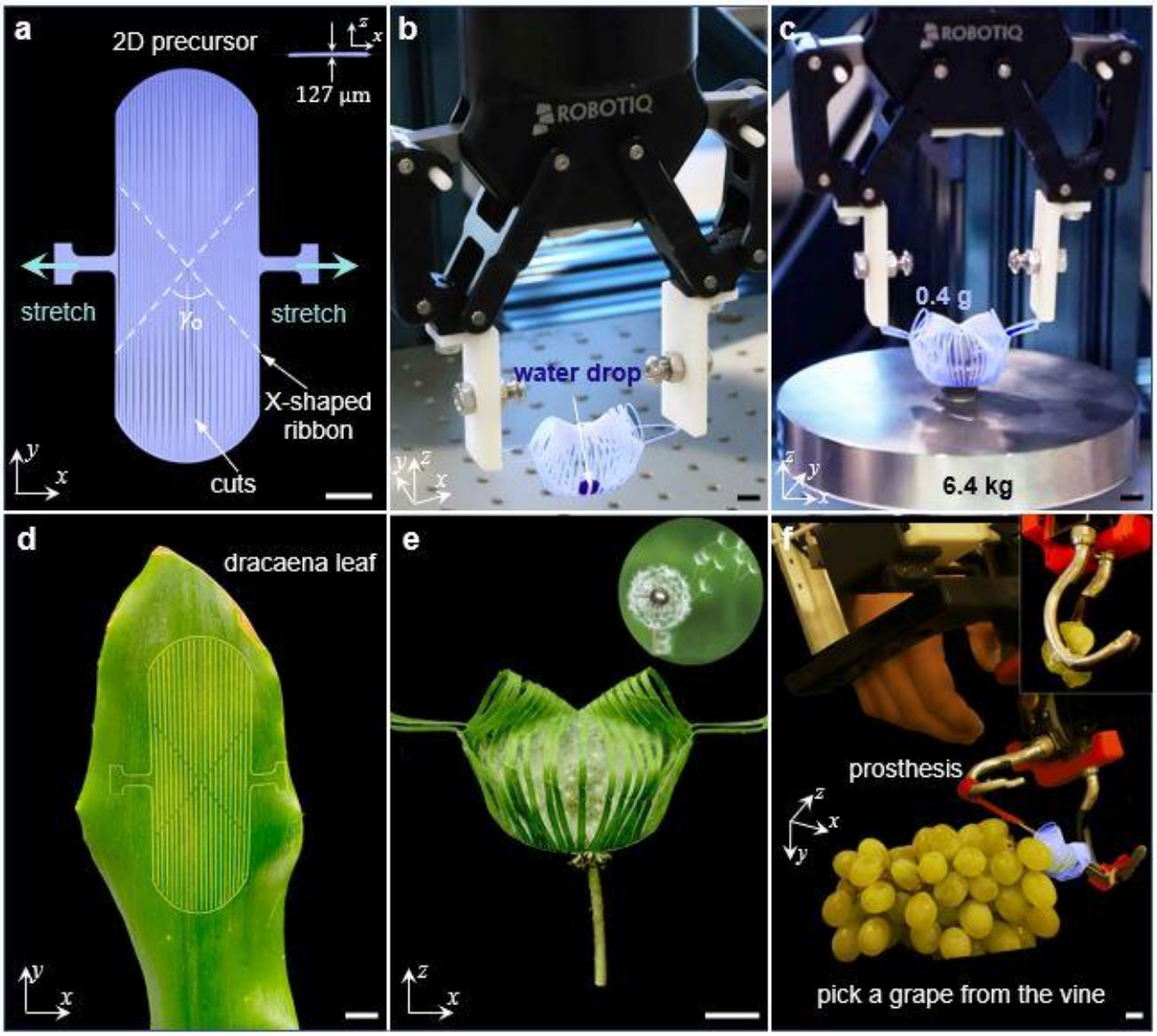

Fig. 4.2 Demonstration of a noninvasive and biodegradable kirigami gripper. a The 2D precursor of the kirigami gripper is divided by a central X-shape ribbon network into two fan shapes and two triangles patterned with parallel cuts. The angle $\gamma_0 = 80°$ is highlighted in dashed white lines, with the inset showing the side view with a 127-μm thickness. Green arrows are the direction of uniaxial stretching. b-c The kirigami gripper integrated with a robotic arm grasping a water droplet (b) and a 6.4kg heavy deadweight (c), 16,000 times the weight of the gripper. d-e 2D precursors of the gripper made of a bare leaf (d). The gripper made of a leaf grasps a dandelion (e). f The kirigami gripper integrated onto a prosthesis electrical terminal device (ETD) assists the prosthesis with picking a grape from the vine noninvasively. The inset shows the squeezed ruptured grape after picking without using the kirigami gripper. Scale bars = 10 mm.

Fig. 4.2 shows the 2D precursor design of the gripper. It comprises a thin flat sheet patterned with parallel cuts, where a central X-shaped ribbon forms an original intersecting angle, γ_0. It is fabricated through laser cutting of a thin polyethylene terephthalate (PET) sheet with a thickness of 127 μm (see "Methods" section). Uni-axial stretching changes the intersecting angle from γ_0 to γ(inset of Fig. 4.3). γ increases towards 180^o with the applied strain ε. Correspondingly, the gripper deploys in such a way that ribbons buckle into a pop-up shell-like caging shape composed of two shells as grasping petals bridged by two cones (Fig. 4.2). The buckling ribbons resemble the shape of Euler elastica[74,90,91]. We combine analytical analysis, experiments, and finite element method to elucidate how the trajectory programmed by γ_0 paves the way towards noninvasive and delicate grasping.

For the angle-based design, the original (γ_0) and deformed (γ) intersecting angle can be explicitly related to the applied strain ε (or the displacement). The relationship is expressed as

$$\varepsilon = c_{\mathrm{r}}\left(\frac{\sin\left(\frac{\gamma}{2}\right)}{\sin\left(\frac{\gamma_0}{2}\right)} - 1\right) \tag{4-1}$$

where c_{r} is a constant related to the normalized length of the stretching ribbon (Methods). The angle design yields the explicit relationship, where a small variation in the curved boundary with the continuity conserved barely affects the performance. Such relationship facilitates the displacement control of the trajectory as discussed later. In contrast, despite the generation of various 3D curved shapes in the boundary curvature-based design in our previous study[46], its inexplicit and nonlinear relationship between the displacement and the Gaussian curvature makes it not suitable for the explicit displacement control (Methods).

Tracing the movement of the end effectors of the gripper in the *yz*-plane defines the grasping trajectory during the stretching-induced deployment. This trajectory plays an important role in governing the grasping performances.

By approximating the shape of the discrete ribbons in the gripper as Euler elastica[74,90,91], we can obtain the Cartesian coordinates along the trajectory curve expressed as

$$\bar{y}_{\mathrm{t}} = \left(\frac{2}{\lambda}\mathrm{E}(\mathrm{AM}(\lambda\overline{s}_{\mathrm{h}}, m_{\mathrm{s}}), m_{\mathrm{s}}) - \overline{s}_{\mathrm{h}}\right)\cos(\beta) \tag{4-2}$$

$$\bar{z}_{\mathrm{t}} = \left(\frac{2}{\lambda}\mathrm{E}(\mathrm{AM}(\lambda\overline{s}_{\mathrm{h}}, m_{\mathrm{s}}), m_{\mathrm{s}}) - \overline{s}_{\mathrm{h}}\right)\sin(\beta) \tag{4-3}$$

where $\bar{y}_{\mathrm{t}}$ and $\bar{z}_{\mathrm{t}}$ are the coordinate functions (Methods). $\overline{s}_{\mathrm{h}}$ is half of the length of the longest discrete ribbon in the petal normalized by the half-width of the 2D precursor. $\lambda = 2\mathrm{F}(\frac{\pi}{2}, m_{\mathrm{s}})/\overline{s}_{\mathrm{h}}$. E, F, and AM denote the elliptic functions. $m_{\mathrm{s}}(\gamma_{\mathrm{o}}, \varepsilon)$ and $\beta(\gamma_{\mathrm{o}}, \varepsilon)$ denote the elliptic modulus and rotating angle of the discrete ribbons in the petals, respectively, which depend on γ_{o} and ε (Methods).

Fig. 4.3 shows the analytically predicted curved trajectories of various grippers with different γ_{o}. First, for grippers with a large γ_{o} (e.g., $\gamma_{\mathrm{o}} = 170^{\mathrm{o}}$), the limited variation in γ from 170^{o} to 180^{o} leads to a short trajectory similar to a circular arc. The arc's *z*-axis displacement decreases monotonically with ε. The deployed gripper exhibits a 3D shape with two petals far from each other at the maximum applied strain $\varepsilon_{\mathrm{max}}$. Second, a slight decrease in γ_{o} (e.g., $\gamma_{\mathrm{o}} = 150^{\mathrm{o}}$) extends the trajectory path to be longer (Fig. 4.3). Compared to $\gamma_{\mathrm{o}} = 170^{\mathrm{o}}$, the gap between the two petals at $\varepsilon_{\mathrm{max}}$ is smaller. Fig. 4.3 shows that the experimental side-view deploying process is consistent with the analytical prediction. At a relatively small applied strain (e.g., $\varepsilon \sim 0.11$), the grippers deform into a large-angled V-shape, when the two petals remain flat and the central parts pop up into cones. At an intermediate applied strain (e.g., $\varepsilon \sim 0.23$), the two petals gradually bend into a

shell-like shape and rotate to approach each other. Third, for grippers with a further decreased γ_0 (e.g., 130^o), the trajectory curls more and exhibits a critical ω-shape. The two petals initially bend and approach the lowest position (y = –1), and subsequently lift to meet in the middle to close the gap (Fig. 4.3). For grippers with a small $\gamma_0 < 90^o$ (e.g., $\gamma_0 = 10^o$ and 80^o), a larger variation in γ with ε causes ribbons to bend more. It makes the ω-shaped trajectory more prominent. Fig. 4.3 shows the experimental deploying process of the gripper with $\gamma_0 = 80^o$, which agrees well with the analytical model. It exhibits a similar deploying process to that of $\gamma_0 = 130^o$ but with a smooth spherical caging shape at ε_{max}.

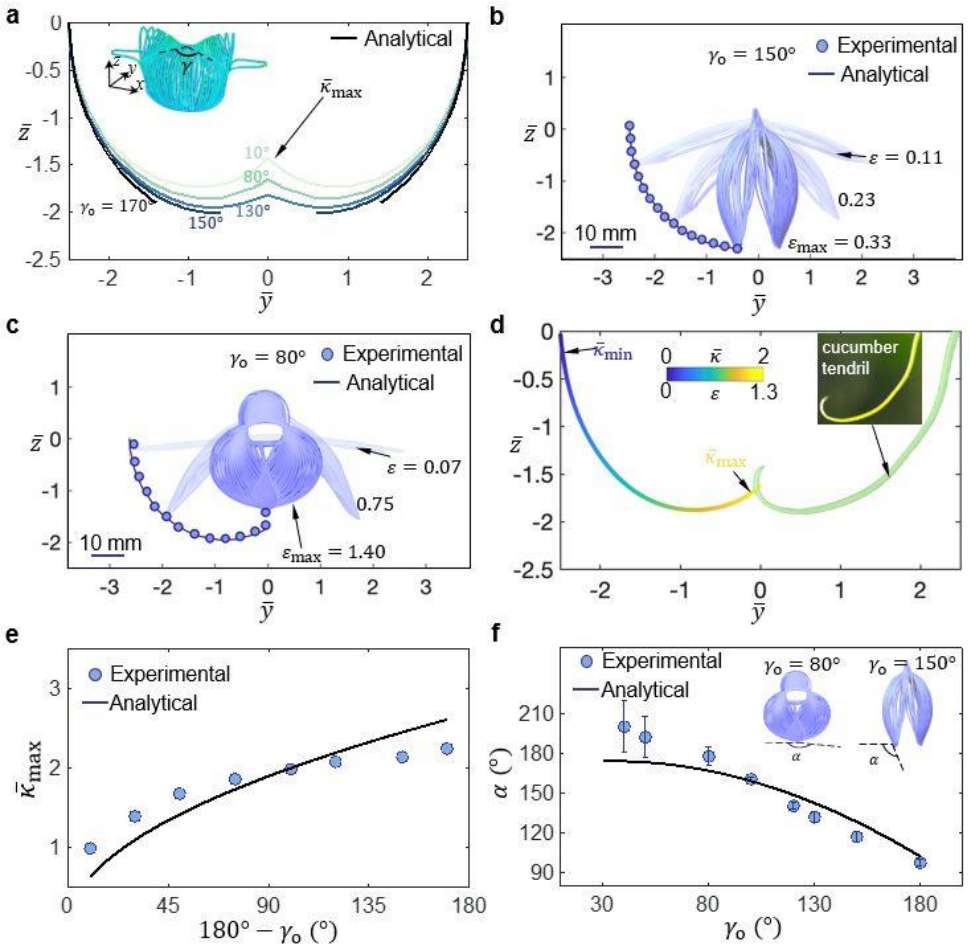

Fig. 4.3 Programmable and controllable grasping trajectories of the gripper. a The deploying trajectories at the end effector of petals in the grippers with different original intersecting angles γ_o. The color of the curves represents different γ_o. $\bar{\kappa}_{max}$ denotes the normalized curvature of the trajectory curve at the maximum applied strain ε_{max}. The inset shows the isometric view of the simulation results of the gripper with $\gamma_o = 80°$, with γ denoting the changing intersecting angle upon stretching. b-c Side-view (in the *yz*-plane) closure process of the grippers with $\gamma_0 = 150°$ and 80°. The deploying trajectories at the end effector of petals with an increasing applied strain ε. d The trajectory of the gripper with mimicking the cucumber tendril curve. The color bar represents the curvature $\bar{\kappa}$ along the trajectory proportional to the applied strain ε. $\bar{\kappa}_{max}$ and $\bar{\kappa}_{min}$ are the maximum and minimum curvature along the trajectory. The inset shows a cucumber tendril. e The normalized curvature $\bar{\kappa}_{max}$ of the trajectory curve at the maximum applied strain as a function of the variation (180°-γ_o) in the original intersecting angle. f The grasping/closing angle α as a function of the angle γ_o in different 2D precursors. The grasping angle α denotes the angle between the tangential direction at the end tip of the petal and the horizontal axis in the fully deployed state. Schematics show the side-view of different α demonstrated by grippers with $\gamma_0 = 80°$ and 150°. The error bars are the standard errors of the mean. Scale bars = 10 mm.

We utilize γ to bridge the gap between the curvature $\bar{\kappa}$ of the trajectory and the strain ε (or displacement). Fig. 4.3 shows that the variation in $\bar{\kappa}$ increases approximately linearly with ε,

$$\bar{\kappa} \propto \varepsilon \tag{4-4}$$

in the trajectory curve of the gripper with $\gamma_0 = 80^o$ (Supplementary Note 3). It facilitates the explicit control of the trajectory through ε. Interestingly, all the trajectories in Fig. 4.3 resemble the shape of the Euler spiral[92], consistent with the curve of a curling tendril (Fig. 4.3) in plants[93]. Mimicking the nastic morphology of plants, the gripper with a gradually curling trajectory enables an ultra-gentle touch, as discussed later. This biomimetic trajectory with gradually increasing curvature $\bar{\kappa}$ is first explored and utilized in soft grippers, to our knowledge.

To quantify how γ_0 programs the grasping trajectory, we derive the correlation between γ_0 and the normalized maximum curvature $\bar{\kappa}_{\max}$ of the trajectory curve (Fig. 4.3) at $\varepsilon = \varepsilon_{\max}$. The correlation is expressed as

$$\bar{\kappa}_{\max} \propto \sqrt{180° - \gamma_0} \tag{4-5}$$

Fig. 4.3 shows that $\bar{\kappa}_{\max}$ is proportional to the square root of the variation in angle 180^o-γ_0. The intersecting angle starts with γ_0 and ends at 180^o during the deployment (Methods). Overall, the smaller the angle γ_0 is, the curlier the trajectory (Fig. 4.3).

Overall, Equation (4-5) enables the simple program of the trajectories through manipulating γ_0. It leads to unprecedented grasping capabilities discussed later. Equation (4-4) allows for the explicit control of the trajectory curvature through the displacement or strain ε. Consequently, based on Equations (4-4) and (4-5), the trajectories become programmable and controllable. Noteworthily, both programming and controlling the trajectory are difficult for existing kirigami grippers based on a shell structure[45] and a curvature-based design[46]. It is mainly due to the nonlinear deformation of shells and the implicit relationship between the boundary

curvature and trajectory (Methods). These significantly impede the gripper's performance in delicate tasks, particularly when integrated with robotic arms and prostheses that rely on a cost-effective displacement/position control[55-57]. Additionally, this contrasts the prevalent soft grippers based on pneumatic/hydraulic-driven[37-42] and stimuli-responsive materials[17,47-52], where explicitly programming their grasping trajectories is very challenging due to the high material nonlinearity.

In addition to the trajectories, the grasping angle α between the two end effectors determined by the fully deployed petals, plays a key role in delicate grasping. α is defined as the angle between the tangential direction at the end tip of the petal and the horizontal axis (insets of Fig. 4.3). Theoretically, α can be predicted as

$$\alpha = -2\tan^{-1}\left(-\frac{2\sqrt{m_s^2-m_s^4}}{1-2m_s^2}\right) - \bar{l}_r\tan^{-1}\left(-\frac{2\sqrt{m_c^2-m_c^4}}{1-2m_c^2}\right) \tag{4-6}$$

$$\frac{2\mathrm{E}(\frac{\pi}{2},m_s)}{\mathrm{F}(\frac{\pi}{2},m_s)} - 1 = \frac{(1+c_b)\sin\left(\frac{\gamma_o}{2}\right)-c_b}{\sin\left(\frac{\gamma_o}{2}\right)+\cos\left(\frac{\gamma_o}{2}\right)} \tag{4-7}$$

where m_s and m_c denotes the elliptic modulus of the discrete ribbons in the spherical petals and central cones, respectively, which are correlated by γ_o in Equation (4-7). $\bar{l}_r$ is the ratio between the characteristic length of the ribbons of the spherical and conical regions (Methods). c_b is a constant related to the buckling of the boundary ribbon.

Fig. 4.3 shows that as γ_o decreases from 180° to 30°, α is predicted to monotonically increase from 97° to a plateau value of 180°, which is consistent with the experiment. However, due to the contact in the petals, experimentally, α can be even beyond 180° for a gripper with γ_o close to 30°. Especially, the gripper with γ_o = 80° show a grasping angle of close to 180° (i.e., $\alpha \sim$ 180°). It defines a critical state, where the two petals form a smooth sphere-like shape (Fig. 4.3).

This is distinct from the sharp-angle tips formed by the two shallow-shell ($\gamma_0 = 130°$, $\alpha = 131.9°$ and $\gamma_0 = 150°$, $\alpha = 117.1°$) petals (Fig. 4.3 and Methods). The deployment with ε in the three grippers can be well reproduced by the corresponding FEA simulations (Methods). It shows that despite the large applied strain, the maximum principal strain remains small (below ~ 1 %) in the gripper due to the significant strain release through buckling of ribbons.

With γ_0 programming the deploying trajectory and the grasping angle, the grasping capability evolves. For the grippers with a larger γ_0, their near circular-arc trajectories and non-smooth enclosing space formed by sharp-angle tips (i.e., a small α) make the invasion unavoidable when pinching the target objects. By contrast, for the grippers with $\gamma_0 = 80°$, the gradually curling trajectory and a near-180° grasping angle facilitate encapsulating a target object ultra-gently. Mimicking a cucumber tendril's nastic and gentle motion, the gradual curling trajectory minimizes the horizontal interaction between the petals and the object, as discussed next. This is especially suitable for noninvasively grasping extremely soft and fragile objects such as liquid droplets (Fig. 4.2) and gelatinous organisms, discussed later. Additionally, for the grippers with $\gamma_0 < 80°$, the curlier trajectory and the grasping angle larger than 180° disturb the smoothness of the spherical cage formed by petals (Methods). It undermines the grasping performance. Additionally, when the petals are compressed by the surface, α further increases to be closer to 180° before the closure of the petals. The deformation due to the compression makes the petals to approach the target in a more parallel way. Overall, considering the trajectory, the grasping angle, and the enclosing volume of petals (Methods), $\gamma_0 = 80°$ is the optimal angle for a gripper to specialize across different extreme scenarios.

4.5 Bending-to-stretching energy transition for Janus-faced feature: ultragentle and ultrastrong

To better understand the Janus-faced feature of being ultragentle to handle extremely soft objects (Fig. 4.2) and ultrastrong to handle ultraheavy objects (Fig. 4.2), we further explore the effects of γ_0 on the stretching force F_x in the x direction (Fig. 4.4) and the two reaction forces F_y and F_z acting on the petals in the y and z direction during grasping. As γ_0 decreases from 150° to 80°, they show similar J-shaped F_x-d_x curves but with a dramatically reducing initial stiffness (Fig. 4.4). We note that reducing γ_0 has the similar effect on the F_x-d_x curves as reducing the boundary curvature from positive to negative in our previous boundary curvature-based shape-morphing kirigami sheets[46]. For $\gamma_0 = 80^o$, a small stretching force F_x of 2N can result in a large displacement in the gripper. Such a small force facilitates its integration with robotic arms and prosthesis.

Before the closure of spherical petals, the inexpensive bending with the gradual curling trajectory leads to an ultragentle touch. Fig. 4.4 shows the touch force F_y (i.e., the quasi-static reaction force in the y direction between the petal and target objects shown in Fig. 4.4) increases with the x-axis displacement d_x regardless of γ_0 but remains small with a maximum value of 35.5 mN. Notably, the contact pressure exerted by the spherical petals is about 0.0468 kPa, which is comparable to the reported gentlest gripper (0.0455 kPa) in handling a jelly fish[39].

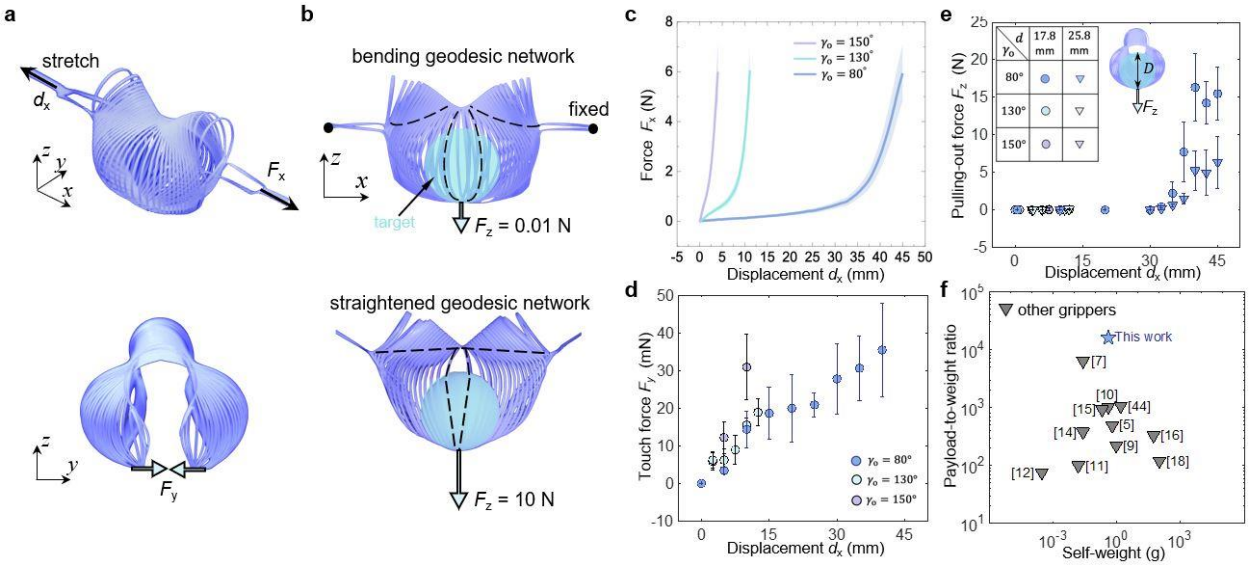

Fig. 4.4 Janus-faced grasping feature. a The isometric view and the side view of the deploying gripper with the increasing displacement along the *x*-axis. F_y denotes the applied stretching force along the *x*-axis. F_y denotes the *y*-direction reaction force between the petals and target object when the gripper is in contact with the target. b Schematics showing the transition of the geodesic ribbon network (highlighted in dashed black line) from bending to stretching with an increasing pulling-out force F_z. F_z denotes the force required in the *z* direction to pull out the green sphere from the gripper, with the green sphere being the target object. Green arrows are the direction of the pulling-out force F_z. Black dots are the fixed points. c Experimental force-displacement (F_x-d_x) curves for three grippers with $\gamma_o = 80°$, 130°, and 150°. The error bars represent the standard errors of the mean. d Experimental touch force F_y as a function of the displacement d_x of three grippers. e Experimental pulling-out force F_z as a function of the displacement d_x for the grippers. The inset shows the schematic illustration of measuring F_z via pulling green spheres with two different diameters *D* out of the grippers. The error bars represent the standard errors of the mean. f Comparison of the robustness (payload-to-weight ratio vs. self-weight) between our gripper and other works.

After the closure of the petals, we explore its adaptive capability for low-to-high payload by pulling out an encapsulated sphere from the fully deployed gripper (Fig. 4.4). The pulling-out force F_z is defined as the minimum force required to pull the sphere out of the gripper. The pulling-out test simulates the scenario when a grasped heavy object tries to slip out of the closed petals. When the pulling force or the grasped object is relatively small or lightweight, the bending geodesic[94,95] network remains curved (Fig. 4.4). However, when F_z is large (Fig. 4.4), the angle-based X shape coupled with the curled-up trajectory at ε_{max} makes the ribbon network become

straightened with dominated stretching energy to prohibit the target from escaping. This bending-to-stretching energy evolution enables the gripper to hold the target object firmly, leading to a large pulling-out force. Fig. 4.4 shows F_z *vs.* displacement d_x for pulling two different-sized spheres out of the grippers with different γ_0. For the gripper with $\gamma_0 = 80°$, as d_x increases from 32.5 mm to 40 mm, α approaches 180°, and the energy evolution in the spherical petals results in a jump of F_z from an average force of 0.41N to 16.3N, a 39 times force enhancement. Note that the sphere with a large diameter (D = 25.8 mm) leads to a smaller pulling-out force than that with a smaller diameter (D = 17.8 mm) because the large diameter prohibits the closure of the sphere formed by the petals. In contrast, the maximum F_z for the grippers with $\gamma_0 = 130°$ and $\gamma_0 = 150°$ is less than 0.3N (Fig. 4.4), over 50 times smaller than that of the gripper with $\gamma_0 = 80°$. This is because their uncurled trajectory ($\gamma_0 = 130°$ and 150°) makes it energetically easier for the target to bend the petals for escaping.

We note that our previous work on the curvature-based design[46] prohibits deployed grippers from forming straightened geodesic ribbons. In contrast, the angle-based design (X-shape) and the curled-up trajectory yield a straightened geodesic network. It results in a bending-to-stretching energy evolution for unprecedented payload capacity shown in Fig. 4.2. Thus, for the gripper with $\gamma_0 = 80°$, the bending-to-stretching energy evolution enables it to be ultragentle in the y direction and ultrastrong in the z-direction, where F_z is over 460 times larger than F_y in the fully deployed state.

Next, we further compare the payload-to-weight ratio[56] of our gripper ($\gamma_0 = 80°$) with that of a host of soft grippers[41,45-53,96] by categorizing them in a diagram of payload-to-weight ratio versus the mass of the gripper in Fig. 4.4. The payload-to-weight ratio (i.e., the ratio of the maximum weight the gripper can carry and the mass of the gripper) is of paramount importance,

especially when grippers are integrated with prostheses and autonomous vehicles[56]. Existing soft grippers harness fluid-driven rigidity percolation[37,59], variation in the stiffness of responsive materials[51,52], eletroadhesion[96], and suction[41] to overcome the intrinsic compliance in soft grippers[97,98]. We note that the payload-to-weight ratio of these reported grippers is entangled below 7,000. Our kirigami gripper can achieve a record-high payload-to-weight ratio of 16,000, which is 2.5 times higher than the reported highest ratio of 6,400[52] (yielded by a gold layer), and 16 times higher than that of our previous curvature-based work[46].

4.6 Universality of the gripper

Leveraging the nastic trajectory, we further demonstrate the universality of the kirigami gripper in grasping a variety of objects in different forms, shapes, sizes, stiffness, materials, and weight, as summarized in Fig. 4.5. First, different from pinching-based[45] grasping in most of the state-of-art grippers such as granular jamming[37], the unique curling-up trajectory similar to gentle tendrils of plants minimizes pinching and pressurizing the grasped objects. This is beneficial for noninvasively manipulating extremely soft and fragile objects, including liquids with close-to-zero stiffness, such as a water droplet, liquid bubbles, and non-Newtonian liquids with a hydrophobic coating, e.g., ketchup and raw egg yolk, soft gels such as pudding and caviar, live gelatinous organisms such as jellyfish (Fig. 4.5) and fish. Second, the net-like enclosed structure can also well handle granular objects in different shapes, such as pills, coins, and ice cubes, as well as medical waste, such as needles and sharps, where gaps between the flexible ribbons can accommodate the randomly oriented sharps without damaging the gripper (Fig. 4.5). This is challenging for pneumatic/hydraulic-based soft grippers with the potential of sharps-induced leaking damages.

Third, the gradually curling-up trajectory and close-to-180° closing angle of the two end effectors make it easy and beneficial to grasp thin disks (e.g., micro-SD card) and delicately handle ultra-thin fibers and sheets, as discussed later. This is extremely challenging for granular jamming-based grippers and pneumatic grippers. Fourth, the bending-to-stretching deformation transition in the ribbons of grasping petals can largely enhance the holding force to pick up heavy objects (e.g., 6.4 kg dead weight in Fig. 4.2). Besides mimicking the nastic curve of plants, the gripper could be made from plants or wood (e.g., the dracaena leaf in Fig. 4.2) and could grasp fragile organisms, including dandelion (Fig. 4.2), fragile fruits (e.g., strawberry in Fig. 4.5), and slippery meat (Fig. 4.5) for food processing to minimize the ecological footprint[88] of the soft robot during both manufacturing and grasping.

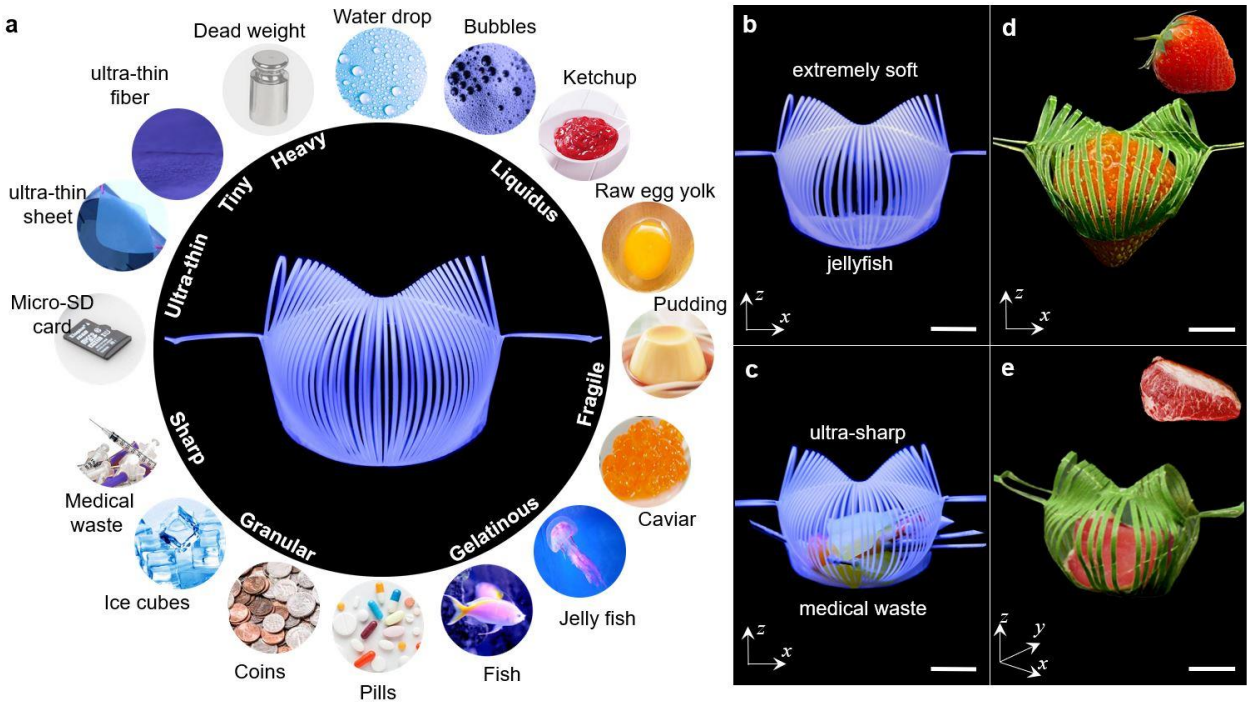

Fig. 4.5 Universality of the gripper. a A collection of various objects in different forms, shapes, stiffness, sizes, and weight that the gripper can handle shows its universality. b-c Demonstration of the gripper in grasping a jellyfish and sharp granular medical trash. d-e The gripper made of a leaf grasps a strawberry and a piece of meat. Scale bars = 10 mm.

4.7 Integration with robotic platforms and prosthetic hands

Leveraging the programmable and controllable trajectories, lastly, we demonstrate the gripper's unaltered capability when it is integrated with both a commercial robotic arm (Fig. 4.6) and an electromyographic (EMG)-controlled upper limb prosthesis (see "Methods" section) for complementing their functions in accomplishing challenging manipulation tasks (Fig. 4.6).

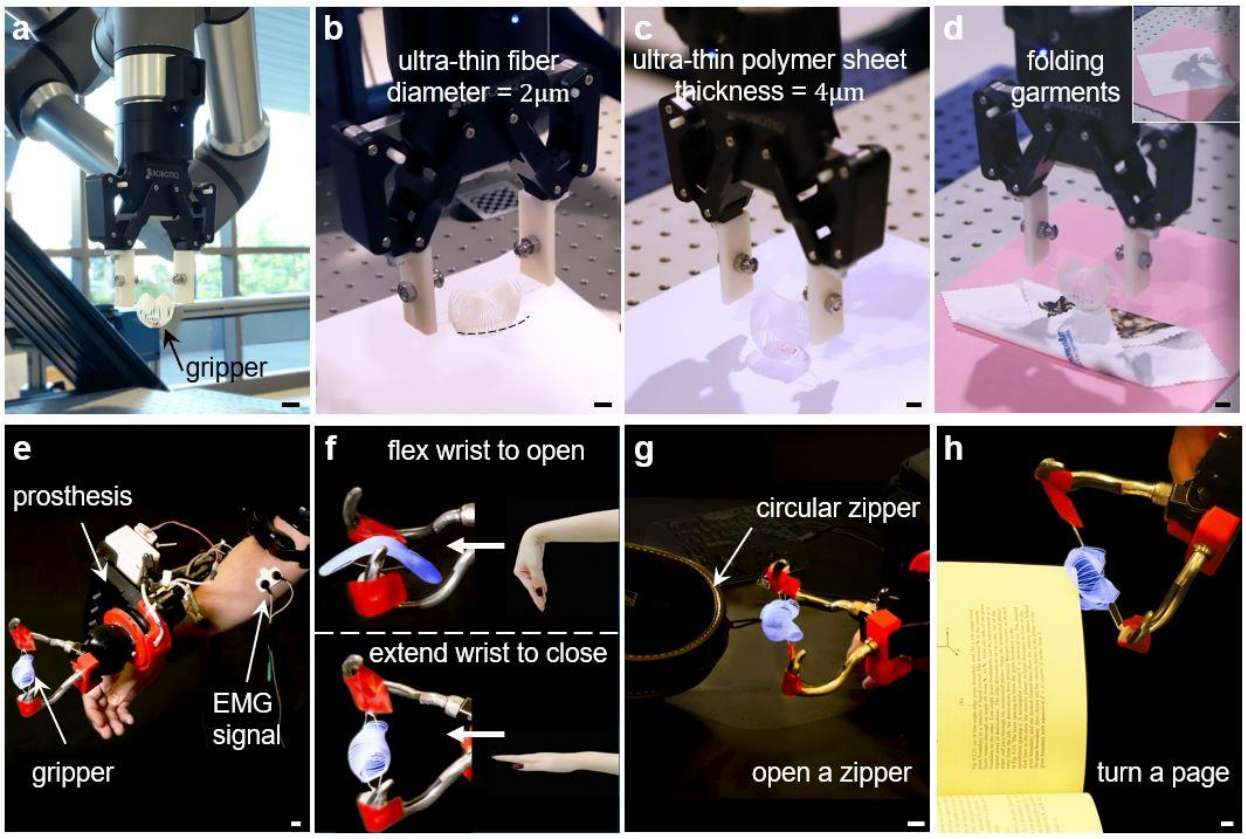

Fig. 4.6 Kirigami gripper integrated with a robotic arm and an electromyographic prosthesis. a-d The kirigami gripper integrated onto a commercially available robotic arm grasps an ultra-thin fiber (b), an ultra-thin polymer sheet (c). The gripper folds garments with the inset showing the unfolded garments (d). e-h The kirigami gripper integrated onto a prosthesis electrical terminal device (ETD) with closed and open states (f) controlled by EMG signals of the wrist flexor and extensor, respectively. The kirigami gripper assists the prosthesis with opening a zipper (g) and turning a book page (h). Scale bars = 10 mm.

Distinct from the reported soft grippers integrated onto a robotic platform[37,39,45], the tendril-like trajectory enables the gripper to perform universal feats that no current rigid or soft machine can accomplish. It can handle the uncertainty in the nondestructive and delicate grasping profoundly. For example, the same robotic kirigami gripper can successfully pick up a water droplet from a hydrophobic surface and place it on either hydrophobic or hydrophilic surfaces (Fig. 4.2), an ultra-thin fiber, e.g., a fiber thread with a diameter of 2 μm in Fig. 4.6, which is 40 times thinner than a human hair (a diameter of around 80 μm), an ultra-thin sheet, e.g., a 4-μm thick polymer sheet in Fig. 4.6, as well as heavyweight in Fig. 4.2. The nastic trajectory enables the spherical petals to scoop the sheet from the target surface ultra-gently (see Methods for detailed discussions). The curling-up grasping, similar to the gentle tendrils, is demonstrated. It minimizes the horizontal interaction between the petals and the thin sheet. Its nastic trajectory and the spherical petals equip the gripper with the capability of handling multidimensional uncertainty in a passive and adaptive way. Thus, it makes the need of highly accurate control of the robotic arm unnecessary, which is especially beneficial when visual perception is hard to be achieved during manipulation[56,99]. Moreover, Fig. 4.6 shows that it can also manipulate thin and flexible objects, such as folding a soft square-shaped garment into a smaller folded square sheet, which are challenging tasks for most existing robotic manipulators[56,99]. The ultra-soft touch prevents damage to the target object without sacrificing the success rate of grasping, 95.2%.

The state-of-art prosthetic devices rely on the user's integration of sensory systems and motor control to achieve nondestructive functions, especially in dexterous tasks[89,100]. We first integrate a soft gripper onto prostheses, which provides an alternative solution to ensure noninvasive interaction in universal tasks. Though existing soft grippers gain non-destructivity but forfeit the universality[39,43,52], here, the programmable and controllable trajectory enables our

kirigami gripper to assist the prosthesis users in universal and nondestructive tasks. Crucially, the simple and explicit relationship, Equations (4-4) and (4-5), stemming from the X-shape design, eases the trajectory control when it is integrated with displacement-controlled prostheses. The easily-deployed feature facilitates the integration with any prosthetic hands (including our demonstrated electrical terminal device (ETD)). When integrated with an EMG-controlled prosthesis ETD (Fig. 4.6), the kirigami gripper switches between the open and close states with the ETD's movements operated by the EMG signals[101-103] recorded from the wrist extensor and flexor, respectively. Flexing and extending the wrist (Fig. 4.6) correspond to the open and closed state of the kirigami gripper, respectively (see "Methods" section).

Further, we evaluate the significantly improved performance of the prosthesis with a kirigami gripper in several representative delicate tasks in daily life, such as picking fruits, opening a zipper, and turning a book page. Fig. 4.2 shows that the kirigami gripper can successfully pick a grape from the vine easily and nondestructively, where prostheses without a high-quality sensory system may squeeze and rupture the grape (inset of Fig. 4.2). The spherical petals of the kirigami gripper help it encapsulate the grape with a high success rate of 78.6%. Fig. 4.6 shows that the kirigami gripper can also successfully open a circular zipper. For existing prostheses without feedback control, slipping out is unavoidable due to the changeable reaction force when manipulating a straight zipper, let alone a circular zipper. Here, the curled-up trajectory coupled with the spherical petals enables the gripper to fit the uncertain reaction passively. Furthermore, Fig. 4.6 shows that the prosthesis with a kirigami gripper can easily turn a book page smoothly. Similar to grasping a super-thin sheet, the gradually curling trajectory enables the gripper to pick and turn a page, which is challenging for the existing robotic prosthesis hands and other soft grippers with unprogrammed trajectories using pinching[45] or enveloping[43]. Moreover, the bulky

support systems of pneumatically or hydraulically driven[37,39,41,42] grippers make it challenging to be integrated onto a wearable prosthesis.

4.8 Methods

4.8.1 Integration with EMG controlled prosthesis device

When integrated with the prosthesis device, the kirigami gripper is controlled by EMG signals. Surface EMG signals were collected from gelled, bipolar electrodes placed over the extensor carpi radialis longus (ECRL) and flexor carpi radialis (FCR) muscles, identified via palpation. The electrodes were connected to an EMG system (MA400, Motion Lab Systems, Inc., USA), and the EMG signals were recorded at a 1000Hz sampling frequency. The magnitude of each EMG signal proportionally drove the speed of the prosthesis ETD motor in one direction.

4.8.2 Grasping mechanism

Regarding precision tasks, the unique features in the gripper with $\gamma_0 = 80°$, such as close-to-180° grasping angle and curling-up trajectory, account for its precision grasping of ultrathin sheet objects in Fig. 4.6. First, when the end effectors touch the substrate surface, the gradual curling in the trajectory facilitates the tip entering the gap between the target and the substrate to perform encapsulating. Second, $\alpha \sim 180°$ enables the spherical petals to approach the sheet in parallel and insert the end tip in parallel to the sheet into the gap between the sheet and the lying surface. This parallel approaching and encapsulating mode minimizes the horizontal interaction between the petals and the target thin sheet. Note that when the petals are in contact with the surface (Fig. 4.7), α further increases to be closer to 180° before the closure of the petals. Then, the curled-up trajectory (Fig. 4.3) ensures the petals lift the target. It is noteworthy that by virtue

of the ω-shaped trajectory, accurate vision control of the traveling routine or distance is not necessary, where the only requirement is to ensure that the end tip of the petal touches the substrate surface. Thus, the parallel encapsulating mode avoids pinching or compressing the target, which facilitates noninvasively grasping a super-thin sheet. Compared to the grippers with larger γ_0, e.g., $\gamma_0 = 130°$ and 150°, their U-shaped trajectories and smaller angle α can hardly grasp the target sheet without compressing the target horizontally. The pinching mode results in the buckling of the thin sheet or a failure of grasping.

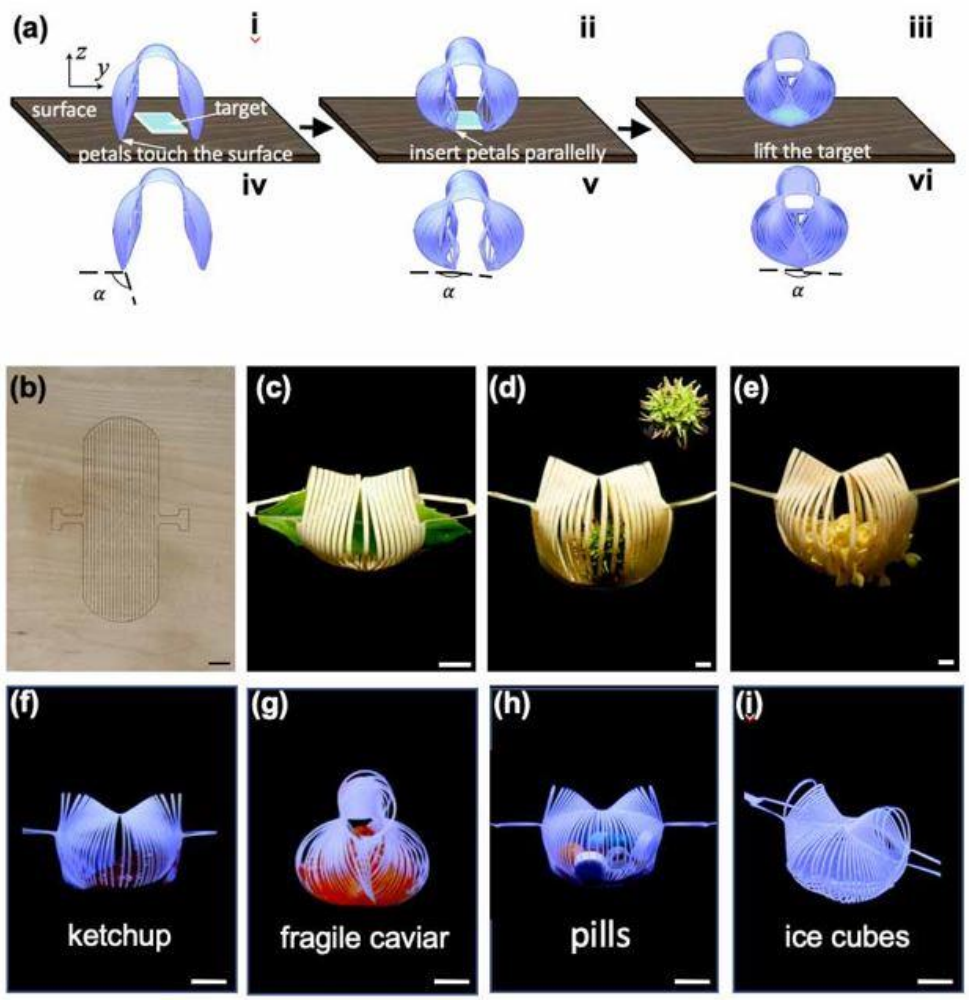

Fig. 4.7 a Schematics of the gripper with γ_0 = 80° grasping an ultra-thin sheet. (a, i) Petals touch the lying surface. (a, ii) Petals affected by the compression from the surface. Petals approach the target parallelly and insert the end tip into the gap between the target and the surface. (a, iii) Petals lift the target. (a, iv-vi) Schematics show the variation in the grasping angle α in a, i-iii. The angle α is defined as the angle between the tangential direction at the end tip of the petal and the horizontal axis. b-e 2D precursor of the gripper made of a wood plate grasping a leaf (c), a thorny plant (d), and rotini (e). f-i Kirigami gripper grasping ketchup (f), caviar (g), granular pills (h), and ice cubes (i). Scale bars = 10 mm.

Regarding delicate tasks, the demonstrations (e.g., waterdrop and jellyfish) serve as compelling showcases of the extraordinary delicacy exhibited by our gripper. Furthermore, it highlights the immense potential of our gripper in tackling challenging scenarios encountered in the fields of minimally invasive biology conservation and biomedicine. We acknowledge that achieving ultra-delicate grasping poses a significant challenge due to the uncertainties arising from

the dynamic task environment (e.g., wetting conditions, viscosity, and rate of operation) and how the living objects will react to touch (e.g., when grasping gelatinous organisms such as a jellyfish). However, by programming the trajectory of our gripper to emulate the nastic curve found in nature, we have significantly enhanced its capability to handle the uncertainties of unknown and unstructured environments, all without the need for feedback control. Regarding wetting conditions, we pick the waterdrop from a flat surface with commercially available hydrophobic coating (Rust-oleum multi-purpose spray kit). This limitation arises due to the inherent challenges associated with picking up a spreading water droplet from a hydrophilic surface without causing damage or compromising the integrity of the droplet. Regarding viscosity, our gripper can be applied to fluids and gelatinous organisms with different viscosity, including Newtonian fluids (e.g., a waterdrop in Fig. 4.2), non-Newtonian fluids (e.g., ketchup in Fig. 4.7), a living jellyfish (Fig. 4.5). Regarding rate operation, the petals, actuated by the Robotiq 2F-85 gripper, approach the waterdrop at velocities of 65mm/s and 35mm/s. Remarkably, we have found that the success rate remains consistently high (76%), even when the velocity is varied within this range. This indicates the robustness and reliability of our gripper's performance across different operating speeds.

The gripper is designed to be larger than the object. It enables the gripper to encapsulate the target to minimize the compression exerted on the target. This encapsulating grasping mode is different from various prevalent soft grippers using pinching mode. The pinching mode requires the gripper to compress the target and then use the friction to lift it. The compression makes noninvasively grasping a water drop or gelatinous organisms impossible.

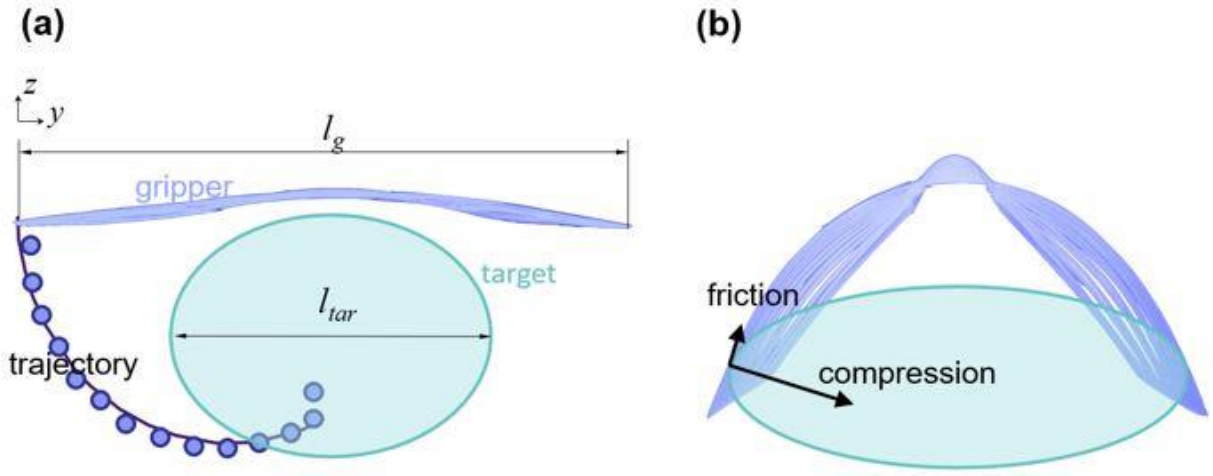

Fig. 4.8 a Schematic showing the side view of the gripper encapsulating the target. l_{tar} and l_g denote the length of target and length of the undeployed gripper, respectively. The black curve and blue dots are the analytical and experimental results of the deploying trajectory, respectively. b Schematic showing the side view of the gripper pinching a large target. The black arrows are the compression and the friction exerted on the target by the gripper.

For the tasks without a high requirement on non-invasion (Fig. 4.8), we use a dimensionless parameter l_{tar}/l_g to analyze the variation in performance of the gripper. As shown in Supplementary Fig. 4.8, l_{tar} and l_g denote the length of target and length of the undeployed gripper, respectively. With l_{tar}/l_g <0.45, the gripper performance barely changes with the curling trajectory scooping up the target. It enables the formation of a straightened geodesic network. As a result, the stretching energy is utilized to hold the target. With l_{tar}/l_g >0.45, the failure in forming a straightened geodesic network leads to a sharp drop in the pulling-out force. Additionally, the gripper has to compress the target and use the friction force to lift the target (Fig. 4.8). The energy increase in the gripper is predominant bending.

4.8.3 Control of the deploying gripper

The curvature-based design is capable of generating various 3D shapes. However, the inexplicit and nonlinear relationship between the displacement and the Gaussian curvature makes it not suitable for the explicit displacement control. For the morphology induced by the boundary curvature, we arrive at a scaling of the curvature as a function of the in-plane tension: $k_b \sim \sqrt{\tau}$, where k_b and τ denote the curvature of the central point in the boundary ribbon and the corresponding in-plane tension, respectively. For the curvature-dominated boundary, the differential equation for the shear tension is given by

$$\frac{d}{ds}\left(\frac{1}{k_b}\left(p_n + \frac{dq}{ds}\right)\right) + k_b q = 0 \tag{4-8}$$

where s denotes the arclength. p and q are the load due and the transverse shear tension, respectively. Substituting q using the linear constitutive equation of the bending moment, we find

$$\frac{d}{ds}\left(\frac{1}{k_b}\left(\frac{1}{2}k_b^3 + \frac{d^2(k_b - k_{bo})}{ds^2} + \frac{p_n}{B}\right)\right) - k_b\frac{dk_{bo}}{ds} = 0 \tag{4-9}$$

The in-plane tension is expressed as

$$\tau = C_1 B(k_b^2 + C_2 + f(k_b, k_{bo})) \tag{4-10}$$

where τ and k_b denote the in-plane tension and the boundary curvature, respectively. B is the bending rigidity. C_1 and C_2 are constants. $f(k_b, k_{bo})$ is a function related to the boundary curvature k_{bo} in the reference configuration and is zero when the boundary of the precursor is circular.

To better understand the angle-based design of the kirigami gripper in Fig. 4.2, we first explore how the prescribed intersecting angle γ_0 guides the displacement-controlled morphology of shell-like grasping petals. We start with the kirigami design of a fan-shaped 2D petal patterned with parallel cuts enclosed by a V-shaped straight ribbon and a circular boundary ribbon with γ_0 = 120°. Upon uni-axial stretching of the 2D petal, the discrete ribbons pop up to form a shallow shell-

like shape with a positive Gaussian curvature K, arising from the increase in the deformed intersecting angle γ. As γ further increases with the applied strain ε, the shell grows with increasing K. When $\gamma = \gamma_{max} = 180^o$, it arrives at a maximally stretched state, corresponding to a fully deployed shape. The morphology and curvature of the fully deployed shells can be programmed by γ_0, where a relatively smaller γ_0 generates a larger K due to its larger angle variation $\Delta\gamma = \gamma - \gamma_0$ ($\gamma_0 \leq \gamma \leq 180^o$). Especially, when $\gamma_0 = 180^o$, K remains zero due to $\Delta\gamma = 0$ and the sheet remains flat.

For different γ_0, the angle-based design presents a simple and explicit relationship between the applied strain ε and γ, i.e.,

$$\varepsilon = \frac{\sin\left(\frac{\gamma}{2}\right)}{\sin\left(\frac{\gamma_0}{2}\right)} - 1 \tag{4-11}$$

This largely simplifies the complex and implicit control equation in the boundary curvature-based design. Note that when the fan-like precursor is combined with the X-shaped ribbons, this relationship need to be modified using the constant c_r related to the length of the stretching ribbon. γ first increases linearly with ε, followed by a steep rise near the fully deployed state for all the prescribed angles γ_0.

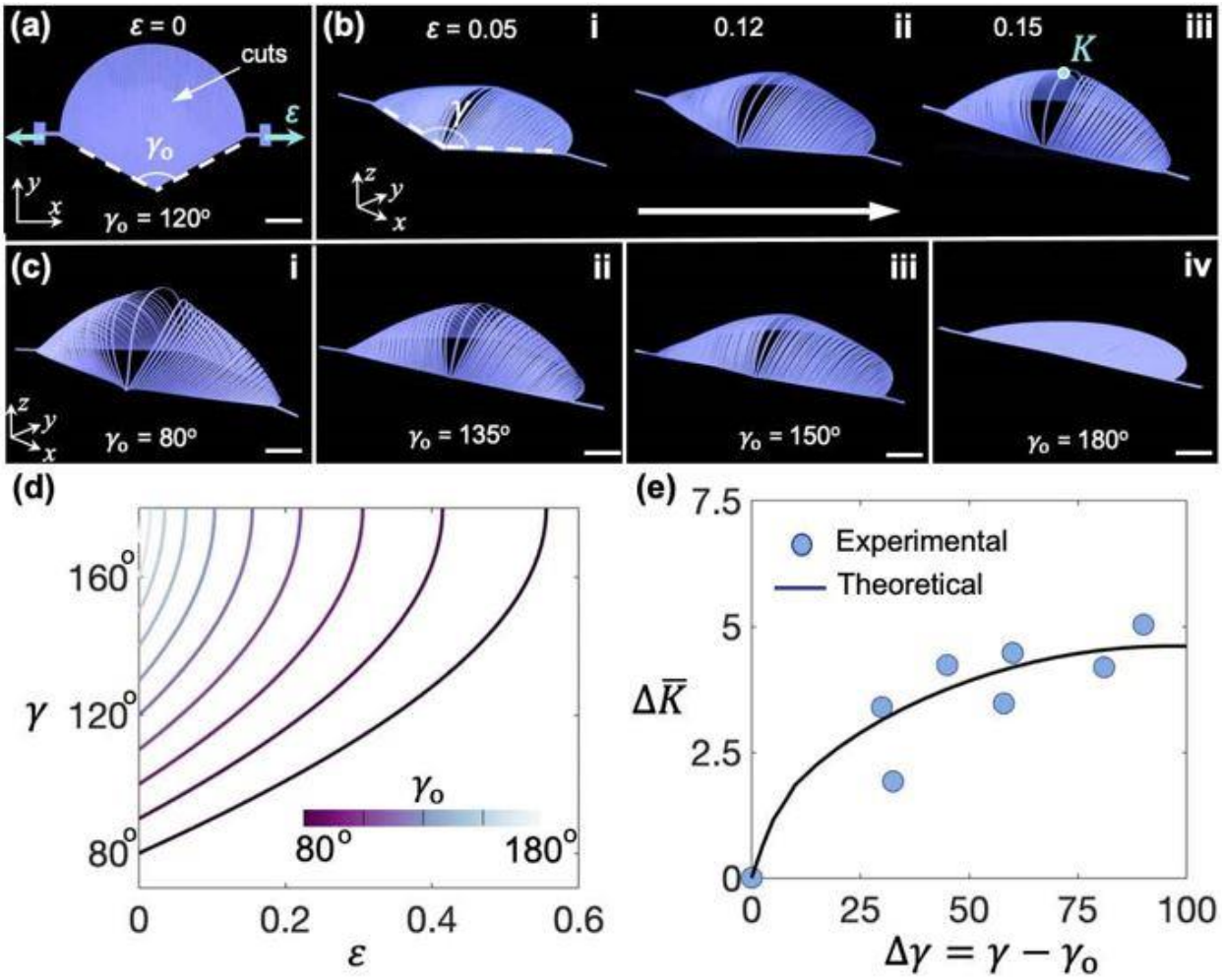

Fig. 4.9 Displacement control of deployment based on an angle-γ_0 design. a Fan-shaped 2D precursor pattern with parallel cuts with the angle $\gamma_0 = 120°$ highlighted in dashed white lines. Green arrows are the direction of applied uniaxial strain ε. b A shell-like 3D shape formed by stretching the fan-shape 2D precursor at an applied strain ε of 0.05 (b, i), 0.12 (b, ii), and 0.15 (b, iii), respectively. γdenotes the varying angle in deformed states, with K being the Gaussian curvature at the top point of the shell-like shape. c 3D shapes formed by ultimately stretched 2D fan-shape precursors with $\gamma_0 = 80°$ (c, i), 135° (c, ii), 150° (c, iii), and 180° (c, iv), respectively. d Theoretical results of the varying angle g as a function of the applied strain ε in 2D precursors with different γ_0. The color bars represent 2D precursors with different γ_0. e Experimental and theoretical results of the variation $\Delta\bar{K}$ in the normalized Gaussian curvature of the shell-like shape as a function of the variation $\Delta\gamma = \gamma - \gamma_0$ in the angle during deformation. Scale bars = 10 mm.

As shown in Fig. 4.9, the correlation between ΔK and $\Delta\gamma$ can be analytically obtained by modeling each discrete ribbon as Euler elastica, which gives

$$\Delta\overline{K} \sim \frac{m_s F(\frac{\pi}{2}, m_s)}{\cos(\frac{\Delta\gamma}{2})} \tag{4-12}$$

where $\Delta\overline{K} = \Delta K/K_{max}$ with K_{max} being the Gaussian curvature of the fully deployed state, m_s is the elliptic modulus characterizing the buckling shape of discrete ribbons, and F denotes the incomplete elliptic integral of the first kind. $\Delta\overline{K}$ first increases monotonically with $\Delta\gamma$ and then approaches a plateau when $\Delta\gamma$ approaches its maximum, which is consistent with the experiments. Thus, with Equations. (4-11) and (4-12), γ bridges the gap between K and ε (or displacement) in the fan shape via an explicit relationship. This simplifies the displacement control of the shape-shifting in the gripper and eases the deploying control when it is integrated with prostheses and robotic arms relying on a cost-effective displacement control.

4.8.4 Program of the grasping trajectory

We note that all the deploying trajectories of the end effectors are consistent with the Euler spiral. The trajectory curvature linear increases along the arclength coordinate s_t of the trajectory curve. We also note that the arclength s_t increases linearly with the applied strain. Thus, s_t bridges the gap between the applied strain and the trajectory and makes the trajectory controllable. Further, with γ_0 increasing, the curvature at the maximum applied strain decreases. Based on the Gauss-Bonnet theorem, the variation in the summation of exterior angles is proportional to the integral of the Gaussian curvature. The two principal curvatures are assumed to be equal, i.e., the square root of the Gaussian curvature. Then the varying principal curvature yields the variation in the trajectory curvature. Thus, we arrive at a scaling of the maximum curvature as a function of the

variation in the original intersecting angle. The simulation results of grippers with γ_0 =80°, 130°, and 180° are consistent with the experiments, where the maximum tensile strain is small. Moreover, the gripper with γ_0 =180° exhibits a U-shape trajectory similar to that of grippers with γ_0 =130° and 150°, which may cause wrinkling or failure in grasping ultra-thin objects.

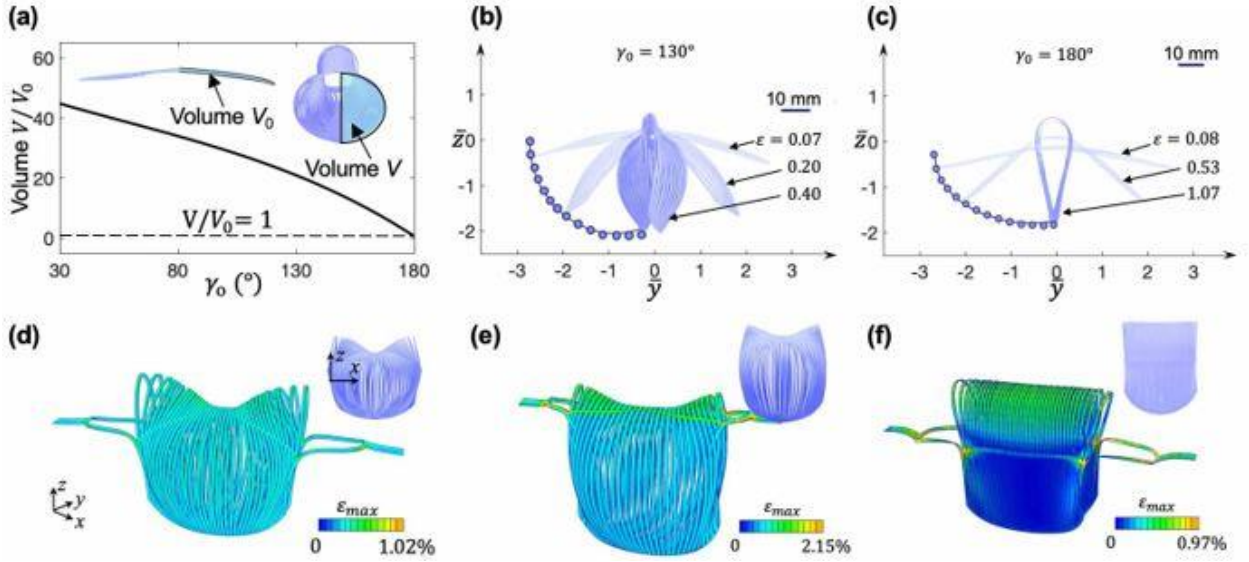

Fig. 4.10 a Normalized volume V/V_0 of deployed grippers as a function of the angle γ_0 in different 2D precursors. The insets show schematics of the volume in the undeployed (V_0) and deployed (V) states. Dashed black lines represent the normalized volume V/V_0 =1 in the undeformed state. b-c The trajectory of the gripper with γ_0 = 130° and 180° with an increasing applied strain ε. d-f Front-view simulation results of grippers (γ_0 = 80°, 130°, and 180°) with insets showing the experimental results. The color bar shows the maximum tensile strain in the ribbons. Scale bars = 10 mm.

Regarding the enclosing volume of petals (Fig. 4.10), for the gripper with γ_0 = 80°, the deploying hemispherical petals with an over 2.4 times larger enclosing volume V than that of the shallow-shell petals of the gripper with γ_0 = 150°. We note that for the gripper with γ_0 = 80°, V is over 35 times the volume V_0 of its undeployed flat state. Meanwhile, it creates a large accommodation room over 40 times its undeployed volume. The elastic and reversible deployment in the kirigami gripper with minimal occupying volume is in sharp contrast to most undeployable

soft grippers, which will facilitate its easy integration with other robotic and prosthesis robotic systems. Consequently, considering the trajectory, the shape of petals, and the volume, $\gamma_0 = 80°$ is optimal for designing the gripper.

4.8.5 Comparison with existing grippers

Table 4.1 A comparison between other soft grippers and our gripper.

	[1]	[3]	[7]	[14]	[15]	[16]	[17]	[9]	[10]	[5]	[44]	[46]	This work
Grasping mechanism	Jamming	Fluid-driven actuator	Fluid-driven actuator	responsive material	responsive material	responsive material	responsive material	Stretching-induced deformation	Stretching-induced deformation	Suction	Electro-adhesion	Adhesive material	Stretching-induced deformation
Programmable deformation	×	×	✓	×	✓	×	×	×	✓	×	×	×	✓
Programmable and controllable trajectory	×	×	×	×	×	×	×	×	×	×	×	×	✓
Noninvasively manipulate gelatinous organisms	×	✓	✓	×	×	×	×	×	✓	×	×	×	✓
Noninvasively manipulate liquid objects	×	×	×	×	×	×	×	×	×	×	×	×	✓
Gentleness (contact pressure)	Unexplored	0.0455 kPa	Unexplored	Unexplored	Unexplored	Unexplored	Unexplored	Unexplored	Unexplored	-15.7 kPa	Unexplored	2.5 kPa	0.0468 kPa
Strength (maximum payload-to-weight ratio)	Unexplored	Unexplored	<100	380	925	330	6,400	222	1,000	490	1,067	Unexplored	16,000
Delicacy (minimum resolution for ultra-thin objects)	Unexplored	Unexplored	Unexplored	Unexplored	Unexplored	10 μm	3.2 mm	1.5 mm	80 μm	2.5 mm	Unexplored	Unexplored	2 μm
Manipulate gelatinous organisms when integrated onto robotic arms and prostheses	×	✓	✓	×	×	×	×	×	✓	×	×	×	✓
Manipulate liquid objects when integrated onto robotic arms and prostheses	×	×	×	×	×	×	×	×	×	×	×	×	✓

We start by comparing our gripper with several representative soft and noninvasive grippers. For example, the kirigami gripper based on a rhombic shell (Yang et al., Science Robotics

2021) can pick a raspberry using pinching mode. The nondestructive gripper based on an origami polyhedron (Teoh et al., Science Robotics 2018) and hydraulic ribbons (Sinatra et al., Science Robotics 2019) can grasp a jellyfish using enclosing mode. Existing noninvasive grippers can be applied to fragile objects and gelatinous organisms. First, from the perspective of noninvasive feature, none of existing grippers can be applied to any of the high-requirement scenarios in biology (i.e., nondestructively grasping marine life softer than jellyfish) and biomedicine (i.e., noninvasively manipulating a liquid drop), as shown in Table 4.1. Distinctly, our gripper surpasses them in the noninvasive feature. It can nondestructively manipulate a liquid drop with near-zero stiffness, as shown in Fig. 4.2. This feature arises from programming the grasping trajectory toward the nastic curve in plants. The gradually curling-up trajectory enables an ultra-gentle touch. From the perspective of the strong feature, the payload-to-weight ratio in our work is 16000, two orders magnitude larger than that of other works shown by Table 4.1. This payload-to-weight ratio is of great importance for noninvasive tasks in unstructured environments (Robert J. Wood et al., Science Robotics 2022). The payload-to-weight ratio in Yang et al.'s work is about 222 due to the pinching grasping mode. The ratio in Teoh et al.'s work is less than 100 due to the rotating polyhedron made of rigid thermoplastic. Third, from the perspective of the design simplicity, in Teoh et al.'s work, the supporting stents are necessary to rotate the origami polyhedron. Both Teoh et al.'s and Sinatra et al.'s work require the support of bulky external hydraulic systems. In Yang et al.'s work, extra design modifications (e.g., extended appendages) are required for grasping a grain of sand or medical pills. In our work, one design can specialize across different tasks. This feature facilitates assisting prostheses in delicate tasks shown in Fig. 4.2 and Fig. 4.6, where frequently changing the end effector for different tasks is necessary in existing prostheses.

Compared with the reported strongest gripper using a gold layer coupled with shape memory polymers (Roh et al., Science Robotics, 2021) with a payload-to-weight ratio of 6,400, our gripper has a ratio 2.5 times higher (16,000). Compared to all existing strong grippers based on stimuli-responsive materials, suction, fluid-driven rigidity percolation, jamming, adhesive materials and electro-adhesion shown by Fig. 4.4 and Table 4.1, our gripper has the largest payload-to-weight ratio.

Existing universal grippers rely on the suction (Song et al., Advanced Materials 2021), responsive shape memory polymers (Linghu et al., Science Advances 2020), and jamming (Brown et al., PNAS 2010). However, none of them can achieve universal grasping while retaining the noninvasive feature. Specifically, suction cannot preserve the gelatinous organisms during grasping. Shape memory polymers require a high temperature (e.g., 80°C in Linghu et al.'s work) that could harm living organisms, let alone the sacrificed response time. The jamming structure cannot grasp gelatinous organisms, let alone liquid objects.

Overall, our new design surpasses the previous one in specializing across different extreme scenarios, including handling extremely soft, ultra-heavy, and ultra-thin/tiny objects. A systematic comparison is provided in Table 4.1.

4.9 Conclusion and discussion

Predominant soft grippers neglect the function of trajectories, due to the complexity of explicitly driving artificial trajectories towards nastic morphologies in nature. It results in systems incapable of specializing across high-requirement tasks. In this article, we proposed a simple angle-based design strategy for a noninvasive, ultrastrong, and universal gripper with high precision. We showed that the shapes of tendril-like trajectories can be explicitly programmed by

the angle γ_0 and simply controlled by the applied strain ε or displacements, which, to the best of our knowledge, has not been achieved previously. Emulating the natural curve enables the gripper to achieve preternatural grasping performances, i.e., extremely soft and ultrathin\tiny targets. The programmable and controllable tendril-like trajectories can be well predicted by the developed analytical modeling, which is validated by related experiments. Further, the programmed trajectory yields a bending-to-stretching energy evolution during heavy-target grasping, thereby radically augmenting its grasping capability. The powerful gripper is capable of grasping various extreme objects in terms of stiffness, size, geometry, form, and weight, including an ultrafragile water drop and gelatinous jellyfish, an ultrathin 4μm-thick polymer sheet and 2μm-diameter fiber, an ultraheavy dead weight that is over ten thousand times its self-weight, and sharp granular medical trash, etc.

We anticipate that the gripper could have broad applications in robotics, marine organism protections, agriculture, food processing, prosthesis, and medical devices. The design philosophy that treats trajectories as mutable leads to functional (i.e., grasping) and energetic evolution. It will catalyze the next-generation soft machine systems. Further, the proof-of-concept demonstration as a biodegradable gripper using bare leaf represents an opportunity for rethinking the engineering design of soft machines that can better integrate with our ecosystem.

In comparison to state-of-the-art specialized and universal soft robotic grippers[58], this work fills the important knowledge gaps both fundamentally and practically. Fundamentally, this work overcomes the challenges in theoretically predicting the grasping trajectories of the reported kirigami grippers[45,46], as well as other soft grippers made of fluidic elastomers[37-42] or stimuli-responsive materials[17,47-52] due to their high materials nonlinearity and large deformation. The intricate nature of trajectories in existing soft grippers stems from the nonlinear and large

deformations inherent in compliant structures and soft materials. Practically, for the first time, it unifies ultradelicacy, ultrastrengh, ultraprecision, universality, and multifunctionality in one single gripper, which is not achieved in all the reported soft robotic grippers (Methods). When it comes to delicate tasks such as manipulating water droplets and jellyfish, achieving noninvasive grasping presents a significant challenge due to the uncertainties inherent in dynamic task environments and the unpredictable reactions of living organisms. However, by programming the trajectory, we enhance our gripper's ability to handle the uncertainties associated with uncertain environments.

This gripper is scale- and material-independent. A question remains regarding what material could optimize durability and strength. Materials with larger Young's modulus and fracture toughness would improve the performance but requires a higher energy input during stretching. Moreover, to minimize the disturbance of the smoothness in the curved surface, the upper and lower boundary requires a C^2 continuity (Methods). For a boundary with a C^1or C^0 continuity, varying the geometry of localized ribbons at the discontinuous point in the boundary could improve performance for extremely soft objects. The aspect ratio and the width of the cut in the 2D precursor are optimized to improve the grasping capability. The grasping performance is affected by the size of the target, a large size could make the gripper unable to encapsulate the target. It could cause the petals to pinch the target, accompanied by a sharp drop in the pulling-out force (Methods). Additionally, the maximum principal strain ε_{max} in the popping-up ribbons is small, resulting in over 1,000 repeated cycles of 1 kg deadweight lifting with the gripper without failure. Round tips at the cut tips can be applied to relieve the stress concentration for improving durability.

CHAPTER 5

Conclusions and future works

In this thesis, I present a novel design strategy for achieving various morphologies in kirigami structures, as well as its applications in wearable devices and soft robotics. Manipulating the boundary curvatures of the cuts can program intricate and dynamic 3D shapes. This approach simplifies the inverse design process considerably, thanks to the geodesic ribbons employed. Furthermore, I demonstrate the practical application of this strategy by creating dynamically conformable heaters for human joints. I envision that this design approach can be extended to a wide range of wearable devices, thereby expanding its potential applications. Additionally, programmably adjusting the geometric parameters can generate nastic wavy shapes that closely resemble natural morphologies. This capability holds promise for applications in wave propagation within mechanical metamaterials and for mimicking the intricate shapes found in plant- and animal-inspired soft robots.

Moreover, programming the grasping trajectory of kirigami grippers can induce a transformative evolution from a noninvasive gripper to a universal gripper that possesses ultradelicacy, ultrastrength, and ultraprecision, capable of excelling in various extreme scenarios. Furthermore, I envision that integrating sensors into this gripper enables in situ characterization of physiological and genomic properties of animals. Additionally, the proof-of-concept demonstration of a biodegradable gripper using a bare leaf opens up possibilities not only for advancements in gripper materials, but also for reevaluating the engineering design of soft machines to foster better integration with our ecosystem.

This thesis focuses on a mechanics- and mathematics-guided system that encompasses the programming of morphologies in mechanical metamaterials, as well as the resultant functional

evolutions facilitated by these morphologies and trajectories. The concept of functional evolution driven by morphological intelligence showcased in this thesis has the potential to propel the development of next-generation soft machine systems.

REFERENCES

1. Liu Y, Genzer J, Dickey MD. “2D or not 2D”: Shape-programming polymer sheets. Progress in Polymer Science 52, 79-106 (2016).
2. van Manen T, Janbaz S, Zadpoor AA. Programming the shape-shifting of flat soft matter. Materials Today 21, 144-163 (2018).
3. Hawkes E, et al. Programmable matter by folding. Proceedings of the National Academy of Sciences 107, 12441-12445 (2010).
4. Felton S, Tolley M, Demaine E, Rus D, Wood R. A method for building self-folding machines. Science 345, 644-646 (2014).
5. Randall CL, Gultepe E, Gracias DH. Self-folding devices and materials for biomedical applications. Trends in Biotechnology 30, 138-146 (2012).
6. Momeni F, M.Mehdi Hassani.N S, Liu X, Ni J. A review of 4D printing. Materials & Design 122, 42-79 (2017).
7. Kuang X, et al. Advances in 4D Printing: Materials and Applications. Advanced Functional Materials 29, 1805290 (2019).
8. Cho Y, et al. Engineering the shape and structure of materials by fractal cut. Proceedings of the National Academy of Sciences 111, 17390-17395 (2014).
9. Shan S, Kang SH, Zhao Z, Fang L, Bertoldi K. Design of planar isotropic negative Poisson’s ratio structures. Extreme Mechanics Letters 4, 96-102 (2015).
10. Blees MK, et al. Graphene kirigami. Nature 524, 204-207 (2015).
11. Tang Y, Yin J. Design of cut unit geometry in hierarchical kirigami-based auxetic metamaterials for high stretchability and compressibility. Extreme Mechanics Letters 12, 77-85 (2017).

12. Tang Y, Lin G, Yang S, Yi YK, Kamien RD, Yin J. Programmable Kiri-Kirigami Metamaterials. Advanced Materials 29, 1604262 (2017).
13. Cui J, Poblete FR, Zhu Y. Origami/Kirigami-Guided Morphing of Composite Sheets. Advanced Functional Materials 28, 1802768 (2018).
14. Callens SJP, Zadpoor AA. From flat sheets to curved geometries: Origami and kirigami approaches. Materials Today 21, 241-264 (2018).
15. Hwang D-G, Bartlett MD. Tunable Mechanical Metamaterials through Hybrid Kirigami Structures. Scientific Reports 8, 3378 (2018).
16. Ning X, et al. Assembly of Advanced Materials into 3D Functional Structures by Methods Inspired by Origami and Kirigami: A Review. Advanced Materials Interfaces 5, 1800284 (2018).
17. Tang Y, Li Y, Hong Y, Yang S, Yin J. Programmable active kirigami metasheets with more freedom of actuation. Proceedings of the National Academy of Sciences 116, 26407-26413 (2019).
18. Cheng Y-C, Lu H-C, Lee X, Zeng H, Priimagi A. Kirigami-Based Light-Induced Shape-Morphing and Locomotion. Advanced Materials 32, 1906233 (2020).
19. Li Y, Yin J. Metamorphosis of three-dimensional kirigami-inspired reconfigurable and reprogrammable architected matter. Materials Today Physics 21, 100511 (2021).
20. Grima JN, Alderson A, Evans KE. Auxetic behaviour from rotating rigid units. physica status solidi (b) 242, 561-575 (2005).
21. Rafsanjani A, Bertoldi K. Buckling-Induced Kirigami. Physical Review Letters 118, 084301 (2017).

22. Qi Z, Campbell DK, Park HS. Atomistic simulations of tension-induced large deformation and stretchability in graphene kirigami. Physical Review B 90, 245437 (2014).
23. Shyu TC, et al. A kirigami approach to engineering elasticity in nanocomposites through patterned defects. Nature Materials 14, 785-789 (2015).
24. Tang Y, Lin G, Han L, Qiu S, Yang S, Yin J. Design of Hierarchically Cut Hinges for Highly Stretchable and Reconfigurable Metamaterials with Enhanced Strength. Advanced Materials 27, 7181-7190 (2015).
25. Yang Y, Dias MA, Holmes DP. Multistable kirigami for tunable architected materials. Physical Review Materials 2, 110601 (2018).
26. Liu Z, Du H, Li J, Lu L, Li Z-Y, Fang NX. Nano-kirigami with giant optical chirality. Science Advances 4, eaat4436 (2018).
27. Neville RM, Scarpa F, Pirrera A. Shape morphing Kirigami mechanical metamaterials. Scientific Reports 6, 31067 (2016).
28. Li Y, Zhang Q, Hong Y, Yin J. 3D Transformable Modular Kirigami Based Programmable Metamaterials. Advanced Functional Materials 31, 2105641 (2021).
29. Song Z, et al. Kirigami-based stretchable lithium-ion batteries. Scientific Reports 5, 10988 (2015).
30. Guan Y-S, Zhang Z, Tang Y, Yin J, Ren S. Kirigami-Inspired Nanoconfined Polymer Conducting Nanosheets with 2000% Stretchability. Advanced Materials 30, 1706390 (2018).
31. Zhang Y, et al. A mechanically driven form of Kirigami as a route to 3D mesostructures in micro/nanomembranes. Proceedings of the National Academy of Sciences 112, 11757-11764 (2015).

32. Zhao R, Lin S, Yuk H, Zhao X. Kirigami enhances film adhesion. Soft Matter 14, 2515-2525 (2018).
33. Rafsanjani A, Zhang Y, Liu B, Rubinstein SM, Bertoldi K. Kirigami skins make a simple soft actuator crawl. Science Robotics 3, eaar7555 (2018).
34. Celli P, et al. Shape-morphing architected sheets with non-periodic cut patterns. Soft Matter 14, 9744-9749 (2018).
35. Choi GPT, Dudte LH, Mahadevan L. Programming shape using kirigami tessellations. Nature Materials 18, 999-1004 (2019).
36. Jin L, Forte AE, Deng B, Rafsanjani A, Bertoldi K. Kirigami-Inspired Inflatables with Programmable Shapes. Advanced Materials 32, 2001863 (2020).
37. Spivak M. A Comprehensive Introduction to Differential Geometry. Publish or Perish (1970).
38. Fan Z, et al. Inverse Design Strategies for 3D Surfaces Formed by Mechanically Guided Assembly. Advanced Materials 32, 1908424 (2020).
39. Levien R. The elastica: a mathematical history.). EECS Department, University of California, Berkeley (2008).
40. Djondjorov P, Hadzhilazova M, Mladenov I, Vassilev V. Explicit Parameterization of Euler's Elastica. Geom Integrability & Quantization 9, 175-186 (2008).
41. Sadik S, Dias MA. On local kirigami mechanics I: Isometric conical solutions. Journal of the Mechanics and Physics of Solids 151, 104370 (2021).
42. Efrati E, Pocivavsek L, Meza R, Lee KYC, Witten TA. Confined disclinations: Exterior versus material constraints in developable thin elastic sheets. Physical Review E 91, 022404 (2015).
43. Timoshenko S, Gere J. Theory of Elastic Stability. McGraw-Hill (1961).

44. Brown E, et al. Universal robotic gripper based on the jamming of granular material. Proceedings of the National Academy of Sciences 107, 18809-18814 (2010).
45. Ilievski F, Mazzeo AD, Shepherd RF, Chen X, Whitesides GM. Soft Robotics for Chemists. Angewandte Chemie International Edition 50, 1890-1895 (2011).
46. Chi Y, Tang Y, Liu H, Yin J. Leveraging Monostable and Bistable Pre-Curved Bilayer Actuators for High-Performance Multitask Soft Robots. Advanced Materials Technologies 5, 2000370 (2020).
47. Sinatra NR, Teeple CB, Vogt DM, Parker KK, Gruber DF, Wood RJ. Ultragentle manipulation of delicate structures using a soft robotic gripper. Science Robotics 4, eaax5425 (2019).
48. Yang Y, Vella K, Holmes DP. Grasping with kirigami shells. Science Robotics 6, eabd6426 (2021).
49. Li S, et al. A Vacuum-driven Origami "Magic-ball" Soft Gripper. In: 2019 International Conference on Robotics and Automation (ICRA)) (2019).
50. Mazzuca SA, Page MC, Meldrum RD, Brandt KD, Petty-Saphon S. Pilot study of the effects of a heat-retaining knee sleeve on joint pain, stiffness, and function in patients with knee osteoarthritis. Arthritis Care & Research 51, 716-721 (2004).
51. Wessendorf AM, Newman DJ. Dynamic Understanding of Human-Skin Movement and Strain-Field Analysis. IEEE Transactions on Biomedical Engineering 59, 3432-3438 (2012).
52. Yao S, Cui J, Cui Z, Zhu Y. Soft electrothermal actuators using silver nanowire heaters. Nanoscale 9, 3797-3805 (2017).
53. Hong S, et al. Highly Stretchable and Transparent Metal Nanowire Heater for Wearable Electronics Applications. Advanced Materials 27, 4744-4751 (2015).

54. Wu S, Yao S, Liu Y, Hu X, Huang HH, Zhu Y. Buckle-Delamination-Enabled Stretchable Silver Nanowire Conductors. ACS Applied Materials & Interfaces 12, 41696-41703 (2020).
55. Xu F, Zhu Y. Highly Conductive and Stretchable Silver Nanowire Conductors. Advanced Materials 24, 5117-5122 (2012).
56. Chen T, Panetta J, Schnaubelt M, Pauly M. Bistable auxetic surface structures. ACM Trans Graph 40, Article 39 (2021).
57. Wu Xue L, Yang Chuan P, Guo Yu Q, Wang Hong Y. Triple-shape memory effect in poly (ethylene terephthalate) (PET) film. Pigment & Resin Technology 47, 55-62 (2018).
58. Yin, J., Cao, Z., Li, C., Sheinman, I. & Chen, X. Stress-driven buckling patterns in spheroidal core/shell structures. 105, 19132-19135, doi:doi:10.1073/pnas.0810443105 (2008).
59. Holmes, D. P. & Crosby, A. J. Snapping Surfaces. 19, 3589-3593, doi:https://doi.org/10.1002/adma.200700584 (2007).
60. Zhao, Y. et al. Somatosensory actuator based on stretchable conductive photothermally responsive hydrogel. 6, eabd5483, doi:doi:10.1126/scirobotics.abd5483 (2021).
61. Kim, Y., Parada, G. A., Liu, S. & Zhao, X. Ferromagnetic soft continuum robots. 4, eaax7329, doi:doi:10.1126/scirobotics.aax7329 (2019).
62. Melancon, D., Gorissen, B., García-Mora, C.J. et al. Multistable inflatable origami structures at the metre scale. Nature 592, 545–550 (2021).
63. Zhao, Y. et al. Twisting for soft intelligent autonomous robot in unstructured environments. 119, e2200265119, doi:doi:10.1073/pnas.2200265119 (2022).
64. Liu, Y., Genzer, J. & Dickey, M. D. “2D or not 2D”: Shape-programming polymer sheets. Progress in Polymer Science 52, 79-106, doi:https://doi.org/10.1016/j.progpolymsci.2015.09.001 (2016).

65. van Manen, T., Janbaz, S. & Zadpoor, A. A. Programming the shape-shifting of flat soft matter. Materials Today 21, 144-163, doi:https://doi.org/10.1016/j.mattod.2017.08.026 (2018).
66. Hawkes, E. et al. Programmable matter by folding. Proceedings of the National Academy of Sciences 107, 12441-12445, doi:10.1073/pnas.0914069107 (2010).
67. Felton, S., Tolley, M., Demaine, E., Rus, D. & Wood, R. A method for building self-folding machines. Science 345, 644-646, doi:10.1126/science.1252610 (2014).
68. Randall, C. L., Gultepe, E. & Gracias, D. H. Self-folding devices and materials for biomedical applications. Trends in Biotechnology 30, 138-146, doi:https://doi.org/10.1016/j.tibtech.2011.06.013 (2012).
69. Momeni, F., M.Mehdi Hassani.N, S., Liu, X. & Ni, J. A review of 4D printing. Materials & Design 122, 42-79, doi:https://doi.org/10.1016/j.matdes.2017.02.068 (2017).
70. Kuang, X. et al. Advances in 4D Printing: Materials and Applications. Advanced Functional Materials 29, 1805290, doi:https://doi.org/10.1002/adfm.201805290 (2019).
71. Cho, Y. et al. Engineering the shape and structure of materials by fractal cut. Proceedings of the National Academy of Sciences 111, 17390-17395, doi:10.1073/pnas.1417276111 (2014).
72. Shan, S., Kang, S. H., Zhao, Z., Fang, L. & Bertoldi, K. Design of planar isotropic negative Poisson's ratio structures. Extreme Mechanics Letters 4, 96-102, doi:https://doi.org/10.1016/j.eml.2015.05.002 (2015).
73. Blees, M. K. et al. Graphene kirigami. Nature 524, 204-207, doi:10.1038/nature14588 (2015).
74. Tang, Y. & Yin, J. Design of cut unit geometry in hierarchical kirigami-based auxetic metamaterials for high stretchability and compressibility. Extreme Mechanics Letters 12, 77-85, doi:https://doi.org/10.1016/j.eml.2016.07.005 (2017).

75. Cui, J., Poblete, F. R. & Zhu, Y. Origami/Kirigami-Guided Morphing of Composite Sheets. Advanced Functional Materials 28, 1802768, doi:10.1002/adfm.201802768 (2018).

76. Callens, S. J. P. & Zadpoor, A. A. From flat sheets to curved geometries: Origami and kirigami approaches. Materials Today 21, 241-264, doi:https://doi.org/10.1016/j.mattod.2017.10.004 (2018).

77. Hwang, D.-G. & Bartlett, M. D. Tunable Mechanical Metamaterials through Hybrid Kirigami Structures. Scientific Reports 8, 3378, doi:10.1038/s41598-018-21479-7 (2018).

78. Ning, X. et al. Assembly of Advanced Materials into 3D Functional Structures by Methods Inspired by Origami and Kirigami: A Review. Advanced Materials Interfaces 5, 1800284, doi:https://doi.org/10.1002/admi.201800284 (2018).

79. Cheng, Y.-C., Lu, H.-C., Lee, X., Zeng, H. & Priimagi, A. Kirigami-Based Light-Induced Shape-Morphing and Locomotion. Advanced Materials 32, 1906233, doi:https://doi.org/10.1002/adma.201906233 (2020).

80. Grima, J. N., Alderson, A. & Evans, K. E. Auxetic behaviour from rotating rigid units. physica status solidi (b) 242, 561-575, doi:https://doi.org/10.1002/pssb.200460376 (2005).

81. Qi, Z., Campbell, D. K. & Park, H. S. Atomistic simulations of tension-induced large deformation and stretchability in graphene kirigami. Physical Review B 90, 245437, doi:10.1103/PhysRevB.90.245437 (2014).

82. Shyu, T. C. et al. A kirigami approach to engineering elasticity in nanocomposites through patterned defects. Nature Materials 14, 785-789, doi:10.1038/nmat4327 (2015).

83. Liu, Z. et al. Nano-kirigami with giant optical chirality. Science Advances 4, eaat4436, doi:10.1126/sciadv.aat4436 (2018).

84. Neville, R. M., Scarpa, F. & Pirrera, A. Shape morphing Kirigami mechanical metamaterials. Scientific Reports 6, 31067, doi:10.1038/srep31067 (2016).

85. Song, Z. et al. Kirigami-based stretchable lithium-ion batteries. Scientific Reports 5, 10988, doi:10.1038/srep10988 (2015).

86. Guan, Y.-S., Zhang, Z., Tang, Y., Yin, J. & Ren, S. Kirigami-Inspired Nanoconfined Polymer Conducting Nanosheets with 2000% Stretchability. Advanced Materials 30, 1706390, doi:https://doi.org/10.1002/adma.201706390 (2018).

87. Zhang, Y. et al. A mechanically driven form of Kirigami as a route to 3D mesostructures in micro/nanomembranes. Proceedings of the National Academy of Sciences 112, 11757-11764, doi:10.1073/pnas.1515602112 (2015).

88. Rafsanjani, A., Zhang, Y., Liu, B., Rubinstein, S. M. & Bertoldi, K. Kirigami skins make a simple soft actuator crawl. Science Robotics 3, eaar7555, doi:10.1126/scirobotics.aar7555 (2018).

89. Celli, P. et al. Shape-morphing architected sheets with non-periodic cut patterns. Soft Matter 14, 9744-9749, doi:10.1039/C8SM02082E (2018).

90. Brown, E. et al. Universal robotic gripper based on the jamming of granular material. Proceedings of the National Academy of Sciences 107, 18809-18814, doi:10.1073/pnas.1003250107 (2010).

91. Ilievski, F., Mazzeo, A. D., Shepherd, R. F., Chen, X. & Whitesides, G. M. Soft Robotics for Chemists. Angewandte Chemie International Edition 50, 1890-1895, doi:https://doi.org/10.1002/anie.201006464 (2011).

92. Song, S., Drotlef, D.-M., Son, D., Koivikko, A. & Sitti, M. Adaptive Self-Sealing Suction-Based Soft Robotic Gripper. Advanced Science 8, 2100641, doi:https://doi.org/10.1002/advs.202100641 (2021).
93. Becker, K. et al. Active entanglement enables stochastic, topological grasping. Proceedings of the National Academy of Sciences 119, e2209819119, doi:10.1073/pnas.2209819119 (2022).
94. Hong, Y. et al. Boundary curvature guided programmable shape-morphing kirigami sheets. Nature Communications 13, 530, doi:10.1038/s41467-022-28187-x (2022).
95. Wani, O. M., Zeng, H. & Priimagi, A. A light-driven artificial flytrap. Nature Communications 8, 15546, doi:10.1038/ncomms15546 (2017).
96. Dong, Y. et al. Multi-stimuli-responsive programmable biomimetic actuator. Nature Communications 10, 4087, doi:10.1038/s41467-019-12044-5 (2019).
97. Ma, M., Guo, L., Anderson, D. G. & Langer, R. Bio-inspired polymer composite actuator and generator driven by water gradients. Science 339, 186-189, doi:10.1126/science.1230262 (2013).
98. Hubbard, A. M., Mailen, R. W., Zikry, M. A., Dickey, M. D. & Genzer, J. Controllable curvature from planar polymer sheets in response to light. Soft Matter 13, 2299-2308, doi:10.1039/C7SM00088J (2017).
99. Linghu, C. et al. Universal SMP gripper with massive and selective capabilities for multiscaled, arbitrarily shaped objects. Sci Adv 6, eaay5120, doi:10.1126/sciadv.aay5120 (2020).
101. Hawkes, E. W., Majidi, C. & Tolley, M. T. Hard questions for soft robotics. Sci Robot 6, doi:10.1126/scirobotics.abg6049 (2021).
102. Gruber, D. F. & Wood, R. J. Advances and future outlooks in soft robotics for minimally invasive marine biology. Sci Robot 7, eabm6807, doi:10.1126/scirobotics.abm6807 (2022).

103. Laschi, C., Mazzolai, B. & Cianchetti, M. Soft robotics: Technologies and systems pushing the boundaries of robot abilities. Sci Robot 1, doi:10.1126/scirobotics.aah3690 (2016).

104. Shintake, J., Cacucciolo, V., Floreano, D. & Shea, H. Soft robotic grippers. Advanced materials 30, 1707035 (2018).

105. Li, S., Vogt, D. M., Rus, D. & Wood, R. J. Fluid-driven origami-inspired artificial muscles. Proceedings of the National Academy of Sciences 114, 13132-13137, doi:10.1073/pnas.1713450114 (2017).

106. Odhner, L. U., Ma, R. R. & Dollar, A. M. in 2012 IEEE International Conference on Robotics and Automation. 2830-2835 (IEEE).

107. Whitesides, G. M. Soft Robotics. Angewandte Chemie International Edition 57, 4258-4273, doi:https://doi.org/10.1002/anie.201800907 (2018).

108. Li, A. et al. Programmable droplet manipulation by a magnetic-actuated robot. Science advances 6, eaay5808 (2020).

109. Runciman, M., Darzi, A. & Mylonas, G. P. Soft robotics in minimally invasive surgery. Soft robotics 6, 423-443 (2019).

110. Devi, M. A., Udupa, G. & Sreedharan, P. A novel underactuated multi-fingered soft robotic hand for prosthetic application. Robotics and Autonomous Systems 100, 267-277 (2018).

111. Zaidi, S., Maselli, M., Laschi, C. & Cianchetti, M. Actuation technologies for soft robot grippers and manipulators: A review. Current Robotics Reports 2, 355-369 (2021).

112. Must, I., Sinibaldi, E. & Mazzolai, B. A variable-stiffness tendril-like soft robot based on reversible osmotic actuation. Nature Communications 10, 344, doi:10.1038/s41467-018-08173-y (2019).

113. Kim, S. Y. et al. Reconfigurable soft body trajectories using unidirectionally stretchable composite laminae. Nature Communications 10, 3464, doi:10.1038/s41467-019-11294-7 (2019).

114. Giannaccini, M. E. et al. A variable compliance, soft gripper. Autonomous Robots 36, 93-107 (2014).

115. Graule, M. A., Teeple, C. B. & Wood, R. J. in 2022 IEEE/RSJ International Conference on Intelligent Robots and Systems (IROS). 9401-9408.

116. Spivak M. A Comprehensive Introduction to Differential Geometry. Vol. 1 (Publish or Perish, 1970).

117. Fan, Z. et al. Inverse Design Strategies for 3D Surfaces Formed by Mechanically Guided Assembly. Advanced Materials 32, 1908424, doi:https://doi.org/10.1002/adma.201908424 (2020).

118. Mazzuca, S. A., Page, M. C., Meldrum, R. D., Brandt, K. D. & Petty-Saphon, S. Pilot study of the effects of a heat-retaining knee sleeve on joint pain, stiffness, and function in patients with knee osteoarthritis. Arthritis Care & Research 51, 716-721, doi:https://doi.org/10.1002/art.20683 (2004).

119. Wessendorf, A. M. & Newman, D. J. Dynamic Understanding of Human-Skin Movement and Strain-Field Analysis. IEEE Transactions on Biomedical Engineering 59, 3432-3438, doi:10.1109/TBME.2012.2215859 (2012).

120. F, L. N. G. A Treatise on the Mathematical Theory of Elasticity. Nature 105, 511-512, doi:10.1038/105511a0 (1920).

121. Rafsanjani, A., Brulé, V., Western, T. L. & Pasini, D. Hydro-Responsive Curling of the Resurrection Plant Selaginella lepidophylla. Scientific Reports 5, 8064, doi:10.1038/srep08064 (2015).

122. Feng, S., Krim, H. & Kogan, I. 3D Face Recognition using Euclidean Integral Invariants Signature. (2007).

123. Cacucciolo, V., Shintake, J. & Shea, H. Delicate yet strong: Characterizing the electro-adhesion lifting force with a soft gripper. (2019).

124. Zhou, X., Majidi, C. & O'Reilly, O. Soft Hands: An Analysis of Some Gripping Mechanisms in Soft Robot Design. International Journal of Solids and Structures 64-65, doi:10.1016/j.ijsolstr.2015.03.021 (2015).

125. Ruotolo, W., Brouwer, D. & Cutkosky, M. R. From grasping to manipulation with gecko-inspired adhesives on a multifinger gripper. Science Robotics 6, eabi9773, doi:10.1126/scirobotics.abi9773.

126. Teeple, C., Werfel, J. & Wood, R. Multi-Dimensional Compliance of Soft Grippers Enables Gentle Interaction with Thin, Flexible Objects. (2022).

127. George, J. et al. Biomimetic sensory feedback through peripheral nerve stimulation improves dexterous use of a bionic hand. Science Robotics 4, eaax2352 (2019).

128. Farina, D. et al. Toward higher-performance bionic limbs for wider clinical use. Nature Biomedical Engineering, 1-13, doi:10.1038/s41551-021-00732-x (2021).

129. Fleming, A. et al. Myoelectric control of robotic lower limb prostheses: A review of electromyography interfaces, control paradigms, challenges and future directions. Journal of neural engineering 18, doi:10.1088/1741-2552/ac1176 (2021).

130. Li, M., Wen, Y., Gao, X., Si, J. & Huang, H. Toward Expedited Impedance Tuning of a Robotic Prosthesis for Personalized Gait Assistance by Reinforcement Learning Control. IEEE Transactions on Robotics PP, 1-10, doi:10.1109/TRO.2021.3078317 (2021).